CHARACTERIZATION AND MODELING OF SMALL AREA $Hg_{1-x}Cd_xTe$ PHOTODIODE SPATIAL RESPONSE

by

Gary James Tarnowski

Submitted to the Department of Electrical Engineering and Computer Science
in partial fulfillment of the requirements for the degrees of

Master of Science in Electrical Engineering

and

Bachelor of Science in Electrical Engineering

at the

MASSACHUSETTS INSTITUTE OF TECHNOLOGY

May 1993

Author _____
Department of Electrical Engineering and Computer Science
May 18, 1993

Certified by _____
Clifton G. Fonstad
Professor of Electrical Engineering
Thesis Supervisor

Certified by _____
Margaret H. Weiler
Staff Engineer, Loral Infrared and Imaging Systems
Thesis Supervisor

Accepted by _____
Campbell L. Searle
Chairman, Departmental Committee on Graduate Students

CHARACTERIZATION AND MODELING OF SMALL AREA $Hg_{1-x}Cd_xTe$ PHOTODIODE SPATIAL RESPONSE

by

Gary James Tarnowski

Submitted to the Department of Electrical Engineering and Computer Science
on May 18, 1993, in partial fulfillment of the
requirements for the degrees of
Master of Science in Electrical Engineering
and
Bachelor of Science in Electrical Engineering

Abstract

This thesis is concerned with three–dimensional numerical modeling and blackbody slit scanner testing of the direct space and frequency domain spatial responses of small area, backside illuminated, long wavelength infrared, heterojunction $Hg_{1-x}Cd_xTe$ photodiodes. The simulation helped to identify factors by which single–pixel modulation transfer function (MTF) might be improved, and an example of that improvement is included. Single pixel MTF was also shown to be dominated by the detector pixel pitch and relatively independent of pitch/mesa ratio. The numerical model was compared to an analytical model, with the results in good qualitative agreement. A blackbody slit scan test and analysis methodology was developed. Slit scans were taken and analyzed on representative small area photodiodes, and the results compared to the numerical model. When the optical input was deconvolved from the raw data, the apparent spatial definition was improved, but the deconvolution method introduced unphysical ripples into the deconvolved data.

Thesis Supervisor: Clifton G. Fonstad
Title: Professor of Electrical Engineering

Thesis Supervisor: Margaret H. Weiler
Title: Staff Engineer, Loral Infrared and Imaging Systems

Acknowledgements

I wish to thank Professor Clifton Fonstad for his role as my on campus advisor for this thesis. In particular, I thank him for his criticism despite the short time frame and for a useful discussion regarding the simulation symmetry and boundary conditions.

Many people were helpful at Loral Infrared and Imaging Systems, the supporters of this research. First and foremost, I express my gratitude to Dr. Margaret Weiler, my company advisor. No matter the adversity, she could conjure a solution. Her supervision of this project, critical readings of this thesis, and generous donation of her time are greatly appreciated.

I thank Nancy Hartle, supervisor of Device Design and Test, for running hurdles which I have not encountered thanks to her. Her more global viewpoint of this project and its motivation was valuable. Dr. Ronald Briggs is thanked for our discussions, as well as for his original creation of the cylindrical coordinates code. I am also grateful for his procurement of hardware for this project, as well as for his thoughtful original design of the spot scan station. I thank Dr. Kevin Maschhoff for our discussions on the MTF of most everything and for his clarification of points. Lynne Terzis is noted for concurrent work on deconvolving the spot and for originally exploring some of the test analysis issues. Richard Hassler, of Optical Engineering, is thanked for the generation of polychromatic objective MTFs. I am grateful to Robert Minich, head technician, for putting up with a host of questions and for scheduling the testing in. I also thank Karl Gustavsen for his showing me the ropes on the spot scan station. Finally, I'd like to thank Steve Krusemark for putting up with integrals and worse, and for knowing so much about bicycling.

More generally, this document represents the culmination of much of my MIT experience. I sincerely thank my parents for their love and support during these five years, and particularly during the adversities of this term. Now that I am a smidgen older, I realize what exceptional people they are.

I also wish to thank my friends here, whom I always wish good luck. I thank my present roommate Matt Bloom for his good humor as we sailed our similar boats this year. I'm grateful to that influential group who've been through a great deal: Cam Daly, Steve Janselewitz, Brian Elder and Ed Walters. I certainly thank Antoinette Baker for her uncomplaining receipt of many tidings, and for her taste in geometric forms. Finally, I thank Banu Ramachandran for her patience, grace, and extraordinary kindness during much of my time here. Thank you, everyone, and best wishes.

Contents

List of Figures

List of Tables

Chapter 1

Introduction

1.1 Background

High performance infrared imaging systems (IIS), as pictured in Figure 1-1, find applications in thermography, night vision, search and rescue operations, atmospheric spectroscopy, military reconnaissance, surveillance, target acquisition and tracking. Increasing system performance demands better individual system components. In particular, requirements which focus on the relation between the contrast in some radiant object and the contrast in its corresponding image are of interest. This relation can be formalized by the modulation transfer function (MTF) of the system. Assuming some imaging system is linear and spatially shift invariant (LSI), the usual Fourier transform techniques are applicable and the transfer function indicates how well the IIS preserves contrast in the image as detail increases in the input illumination scene. The focal plane array (FPA), shown schematically in Figure 1-2, is the transducer from photons to electrons, and allows the optical system to interface with the electronic systems which follow it. The drive to make systems not only better at imaging, but lower in total size, weight, thermal load, and power dissipation concentrates attention on improving the MTF performance of these arrays.

Linear or square FPAs are made of single photodiodes, also shown in Figure 1-2. Linear scanning arrays may have 4×480 elements and square staring arrays may have 256×256 elements. Staring arrays are of particular concern since their use can eliminate mechanical moving parts like scanning mirrors, thereby reducing system size, weight, and complexity. This thesis focuses on long wavelength infrared (LWIR) liquid–phase epitaxially grown (LPE) P–on–N $Hg_{1-x}Cd_xTe$ heterojunction photodiodes, such as are fabricated at Loral Infrared and Imaging Systems (LIRIS), where this research was performed. Their spatial response may be characterized by the diode impulse response function, $\mathrm{dir}(x, y)$, or equivalently in the spatial frequency domain by its Fourier trans-

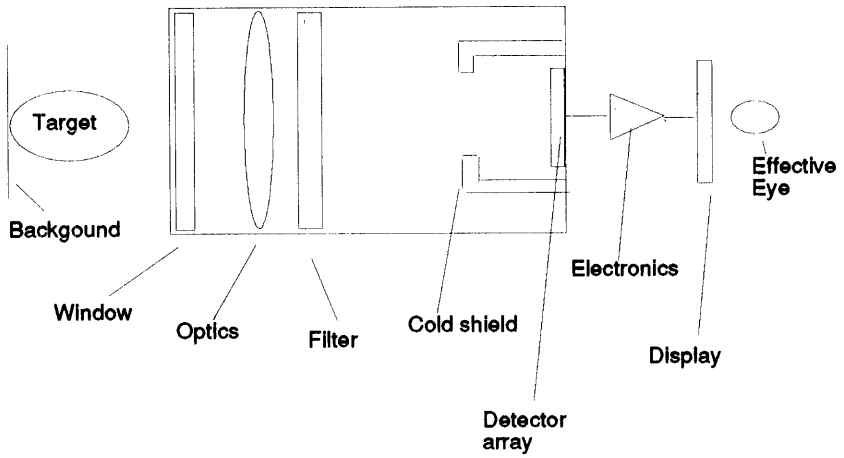

Figure 1-1: Schematic of a typical infrared imaging system. After reference [4].

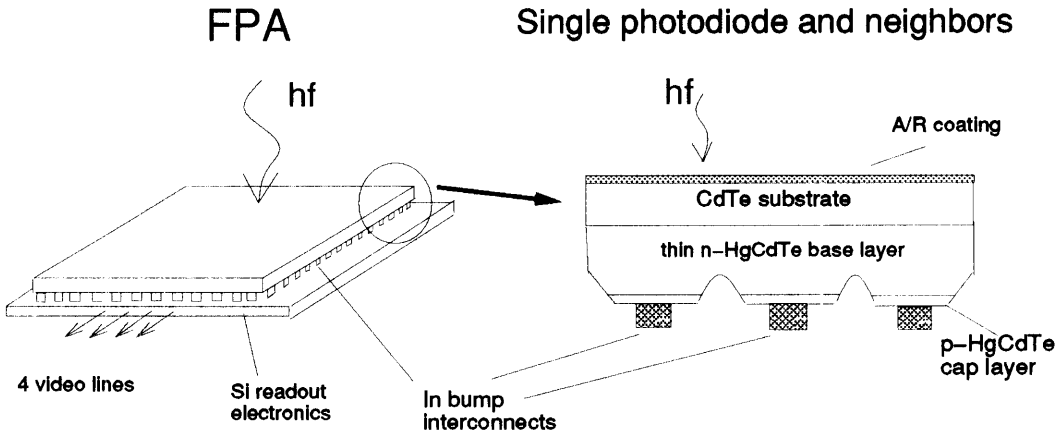

Figure 1-2: Schematic of a focal plane array, the element of the IIS examined in this research. Such arrays are constructed by replicating individual photodiodes, also shown in schematic.

form, DIR(f_x, f_y)[1], where the spatial impulse is an infinitesimally thin bandlimited "ray" from a blackbody source whose photon flux density is such that low level injection conditions prevail in the diode. It is this DIR(f_x, f_y) which is the single pixel MTF.

The MTF is of concern in both thermal imaging system design, since one wants to predict system performance, and in IIS evaluation in order to prove that the system performs as expected. The designer needs to be aware of the trade–offs between increasing MTF at the expense of other measures of IIS performance. In direct–space, the principal trade–off is between the flood illumination response of a photodiode and the response as a function of illumination impulse distance from the diode. The mesa and junction areas of such photodiodes are generally made smaller than the "cell" size of the diode in order to reduce space charge region generation–recombination currents and junction perimeter leakage currents [8], as well as the gamma–ray sensitive area [9]. Thus the diode photocurrent strongly depends on lateral optical collection in order to enhance the effective quantum efficiency. However, as device dimensions approach that of a diffusion length, carriers photogenerated in one cell may be collected by the junction of some neighboring cell, compromising the spatial definition of the array's pixels. Similarly, trade-offs between MTF and noise levels may be found.

1.2 Imaging System MTF

Any intensity pattern may be constructed by the appropriate sum of sinusoidal waveforms. Thus any object intensity may be Fourier transformed. First, a simple sinusoidal incident illumination intensity is considered:

$$i(x) = A_{dc} + A_{ac} \cos 2\pi f x \tag{1.1}$$

The modulation in such a waveform is given by

$$\mathrm{M} = \frac{A_{ac}}{A_{dc}} \tag{1.2}$$

The modulation transfer function is then just

$$\mathrm{MTF} = \frac{\mathrm{M_{image}}}{\mathrm{M_{object}}} \tag{1.3}$$

Since the system output, or image, is likewise transformable, there exists a system function

$$\mathrm{MTF}(f) = \frac{\mathrm{M_{image}}(f)}{\mathrm{M_{object}}(f)} = \frac{A_{\mathrm{image},ac}(f)}{A_{\mathrm{object},ac}(f)} \tag{1.4}$$

[1] Direct space responses are denoted by lowercase letters, frequency space functions by uppercase letters.

and it may be seen that the MTF($f = 0$) is always equal to unity; that is, the dc input suffers no modulation, although it is generally scaled from subsystem to subsystem. The transfer function of an entire imaging system might be modeled [6] as

$$\mathrm{MTF}(f) = \mathrm{MTF_{LOS}MTF_{OPT}MTF_{ARR}MTF_{ELC}MTF_{DSP}MTF_{EYE}} \tag{1.5}$$

with the subscripts indicating the MTF associated with

LOS Line of sight jitter (mechanical instability)

OPT Optics

ARR Focal plane array and readout electronics

ELC Electronics, including A/D converters, filters, and amplifiers

DSP Display (like a CRT)

EYE Effective eye, or just the eye for a human observer

The MTF of the detector array alone, as given in [6] is the product of the detector size and detector spacing MTFs, both of which are given as sinc functions of the appropriate widths. If array MTF is improved, either the whole system MTF may be improved or the requirements on some other portion of the system may be made less stringent, potentially reducing costs. The MTF model described above, while convenient, does not deal with detector MTF in detail. More detailed models of diode MTF, including carrier diffusion, follow.

1.3 Outline

This thesis begins with the theory of photodiode and FPA spatial response, examining the effects of carrier diffusion, photodiode geometry, sampled–scene phase, sampling and aliasing in Chapter 2. Chapter 3 describes the implementation and results of a three–dimensional numerical model whose outputs are the direct and frequency space responses of simulated photodiodes. The results are used to show how an FPA may be designed to optimize its single pixel MTF performance. Chapter 4 describes blackbody slit scanner testing of photodiodes, again from a transfer function point of view. This allows the removal of the effects of a finitely–small input illumination form. Chapter 5 discusses the real–world application of this test model, given signal–to–noise and other uncertainty issues. Chapter 6 presents results of the slit scans in both the direct and frequency space domains, before and after deconvolution of the slit and optical diffraction patterns. Finally, results are summarized and assessed in Chapter 7, and suggestions for future efforts are made.

Chapter 2

Photodiode spatial response theory

The spatial response problem can be examined in terms of the whole array or in terms of just a single diode. This chapter first discusses attempts to specify the MTF of the shift variant FPA, and then examines modeling the spatial response of just a single detector.

2.1 MTF models of the sampled imaging system

The imaging system cascade models presume both linearity and shift–invariance. Although linearity shall be assumed hereafter, nonlinear responses and nonuniform responses of any part of these systems makes their description difficult and degrades their performance. Several issues must be dealt with in modeling the FPA. Incident illumination is converted from some analog waveform into a spatially discrete representation. The response of any photodiode to illumination depends on the the phase of the illumination with respect to the sampling grid, and is therefore shift–variant. This grid is given by the center–to–center spacing between the detectors. The center–to–center spacing is called the pitch and can in general be different for both x and y. This is illustrated in Figure 2-1. Since a sampling process is involved, the spectrum of the output is aliased about the sampling frequency. While the problem of aliasing can be avoided by low–pass filtering the input waveform using the optical system, the sampling phase dependence cannot. Additionally, diffusion in the substrate needs to be addressed, no matter what geometry is proposed. While all these issues have not been dealt with by a single author, a review follows in order to show how each piece may be addressed.

The model of Wittenstein, *et al.* [11] neglects carrier diffusion, but is an excellent introduction to the issue, although its conclusion is not very useful. An analogy is drawn between isoplanatism

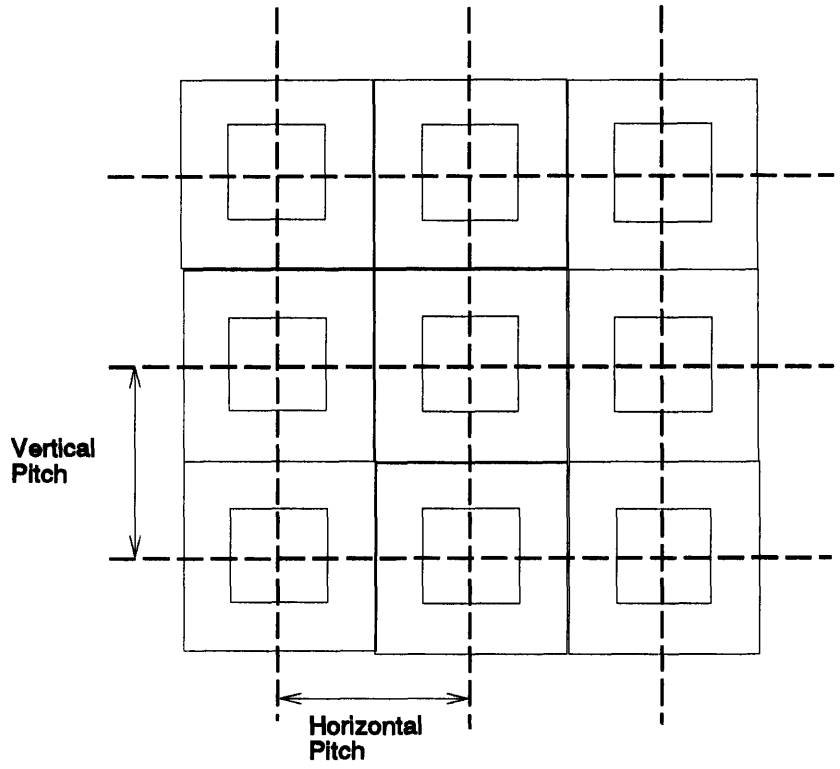

Figure 2-1: The diode geometry, sampling grid, and pitch. Solid lines indicate the array of photodiodes. The interior squares are the physical junctions, and the larger outer squares define the cell size. The sampling grid referred to in the text is given by the intersection of the dotted lines. The respective pitches are also shown.

in direct space and isoplanatism in Fourier space. For optical systems, the direct space region where the system is shift invariant is the isoplanatic region, or corrected field. In the region where the MTF of the *reconstructed* and continuous function is not compromised due to phase, the region is deemed isoplanatic. The paper essentially extends the Nyquist criterion to optical systems and examines when it is adequate.

Park, *et al.* [7] take a somewhat more useful approach in that they determine a limiting case model which is the basis (or could be the basis) for the pitch MTF used in typical array MTF models. The approach is to assume the input functional phase is unknown, and to average the MTF over all possible locations relative to the sampling grid. This stochastic approach is equivalent to convolving the input function with the two-dimensional rectangle function associated with the pitch of the pixels. This approach provides a useful limiting case for design decisions, although taken alone it would indicate that maximizing the pixel density is all that is required.

de Luca, *et al.* [4] approaches the problem uniquely by not using Fourier techniques, but by finding the results in direct space. While representing pixels as uniform response apertures located on a certain pitch, and again neglecting diffusion, the MTF can be written down by integrating the incident sinusoid over the detector aperture while keeping track of its phase, and then finding those discrete pixel responses which are highest and lowest on the entire focal plane. Thus the MTF is found as a function of phase; furthermore the high point and low point are picked out for any frequency. Hence the issues of discrete outputs, sampling, aliasing, and phase are incorporated into the model. Only the single pixel response is simplified.

2.2 Analytical models of single pixels

2.2.1 Convenient models

The spatial response of single pixels is often grossly simplified for convenience. Gaussians may be used, based on fitting spot scan or slit scan data. Models may not include carrier diffusion at all, and assume a uniform response across the pixel aperture. Some models may acknowledge crosstalk, and use measured data to weight and then linearly superpose two aperture functions in direct space and thus two sinc functions in frequency space, as shown in Figure 2-2. Let the function $\mathrm{rect}(x/X)$ indicate a rectangle of unit height centered on the origin whose width is given by X. Its Fourier transform is denoted by the sinc function, or $\sin(\pi X f_x)/(\pi X f_x)$. A real diode response, however, does not have step discontinuities like the rect function does.

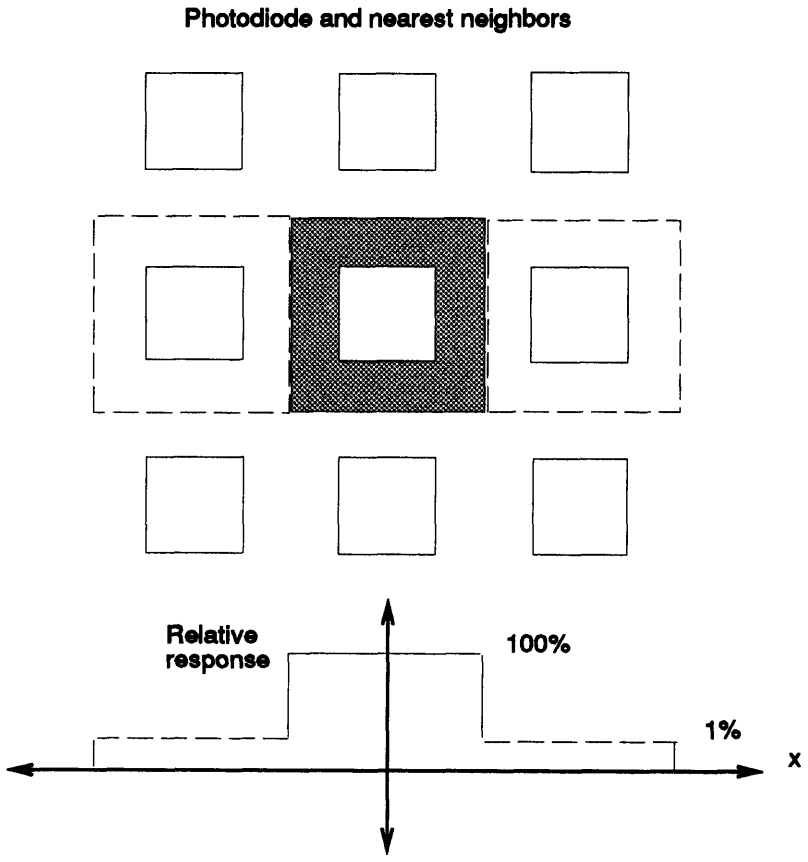

Figure 2-2: Modeling crosstalk between nearest neighbor diodes. Uniform collection of radiation in central shaded cell is assumed.

2.2.2 Cheung's model

Cheung's model [3] bears the closest resemblance to a real diode response except for the numerical modeling in this thesis. The model assumes an array of junctions with no separation between junctions. Incident from the backside is a monochromatic sinusoidal input. The assumptions made and solution are very similar to the approach taken in Chapter 3. The drift/diffusion equation is solved for the charge concentration. The current density into the junctions is found as a function of x and f_x. The quantum efficiency is then found as a function of sinusoidal illumination spatial frequency. Upon normalization to the dc quantum efficiency, the model yields the MTF due to carrier diffusion alone, or $\mathrm{MTF}_{\mathrm{CD}}(f)$. The integration over the depletion region is recognized to be a convolution of the current density with a rect function. Hence the complete MTF for this case may be written as

$$\mathrm{MTF}(f) = \mathrm{MTF}_{\mathrm{CD}}(f)\mathrm{sinc}(\pi w f) \tag{2.1}$$

where w is both the width and the pitch. The result of this model is illustrated in Figure 2-3.

This model solves for a one-dimensional MTF. In the case of LIRIS photodiodes, the mesa area is often less than the pitch area, as schematically shown in Figure 2-2. The diffusion point spread function is different for this geometry which includes spatially distinct junctions, mesa delineation cuts and frontside surface recombination. Since the point spread function is different, shift–variant, and not analytically tractable, the numerical model of Chapter 3 was implemented to correctly calculate the single pixel photoresponse, whose Fourier transform is the single pixel MTF, without resorting to undue simplification. Chapter 3 discusses how this single pixel MTF might be combined with the model given in [4] to yield a complete FPA MTF.

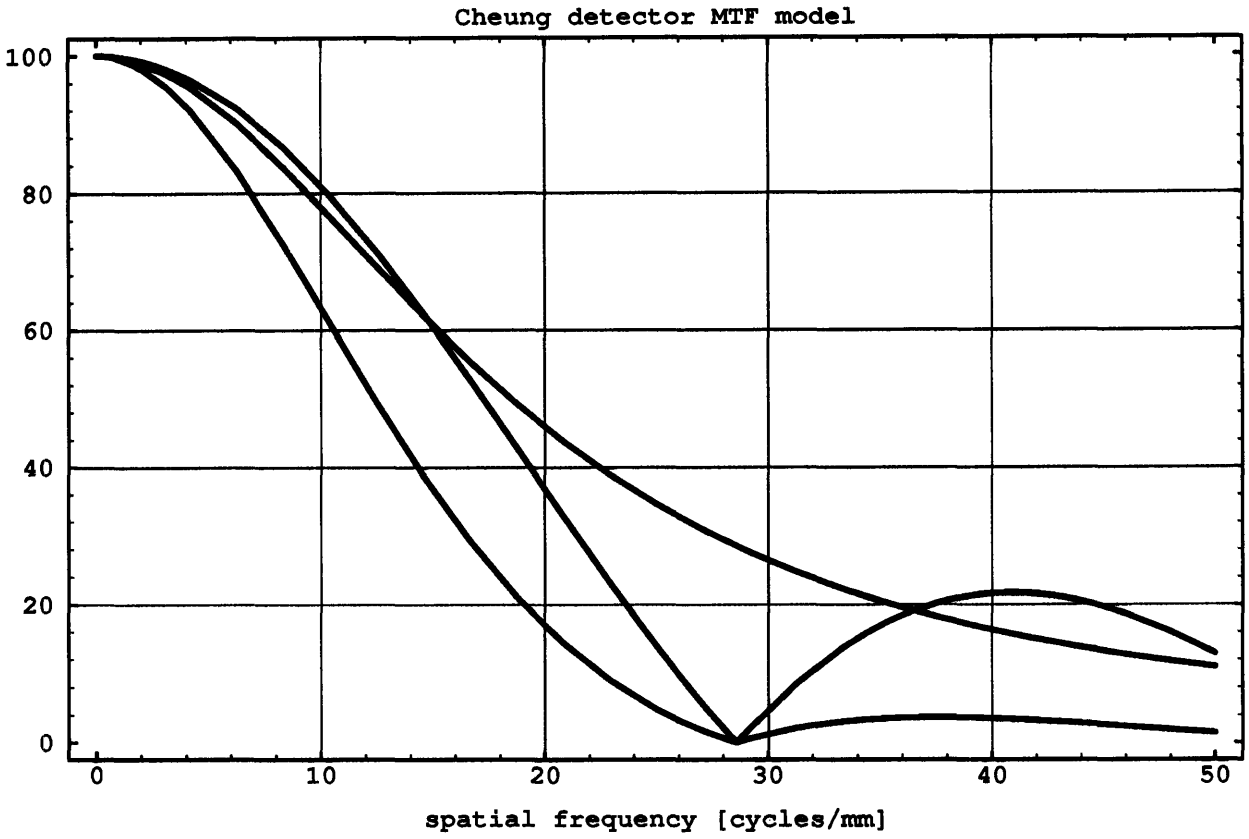

Figure 2-3: Cheung PV detector array MTF model. The carrier diffusion MTF(f) is the curve which is everywhere non–zero. The pitch sinc($\pi w f$) is the middle curve at $f = 20$ cycles/mm, going to zero at (1000 / 35) cycles/mm. Their product, the detector MTF, is the lowest curve. These curves are shown for an absorption coefficient of 2000/cm, a base thickness of 15 μm, a diffusion length of 15 μm, no collection enhancing field, and a detector pitch of 35 μm.

Chapter 3

Numerical modeling

A desirable MTF model would incorporate the following effects: diffusion, array geometry, spatial phase, sampling, discretization and aliasing. Both Cheung's and de Luca's models use direct sinusoidal input to find an MTF. Instead of a simple uniform aperture, the integral in de Luca's expression for sampled modulation response (SMR) could be performed over the "real" spatial profile of the diode, the diode impulse response function. In particular, the product of an incident sinusoid and a numerically found diode impulse response could be integrated for several different phases and frequencies. The high and low valued pixels on the FPA could be found, generating a phase–dependent MTF. This MTF would characterize the shift–variant FPA. This chapter describes how the spatial profiles of single detectors may be found by a numerical model. The approach is that of [1, 2], where the calculation is here extended from cylindrical to rectangular coordinates.

3.1 Derivation of the numerical model

3.1.1 Physical assumptions

The complex physics of the p–n heterojunction requires simplification so that a tractable problem is posed and solved. The simulation domain is considered entirely within the n–type base of the detectors and concerns itself with excess minority carriers only. The assumptions include

- Negligible thermal gradients; thermal equilibrium between electrons and the lattice.
- Scalar dielectric constant ϵ, and scalar hole mobility μ_p and diffusion coefficient D_p obeying the Einstein relation

$$\frac{D_p}{\mu_p} = \frac{kT}{q} \tag{3.1}$$

where k is Boltzmann's constant and q is the elementary charge quantum.

- The material is quasineutral so that

$$\nabla \cdot \epsilon \mathbf{E} = \rho \simeq 0 \tag{3.2}$$

- The electric field is curl–free, and there are no externally imposed magnetic fields

$$\nabla \times \mathbf{E} = 0 \tag{3.3}$$

- Thus the electric field in the material is a constant, E_z, arising from the alloy composition gradient. It is assumed to be z–directed and collection enhancing.

- Boltzmann transport, so that the current density equation for holes may be written as

$$\mathbf{J}_p = q\mu_p p\mathbf{E} - qD_p \nabla p \tag{3.4}$$

and the continuity equation may be written as

$$\frac{\partial p}{\partial t} = G_p - R_p - \frac{1}{q}\nabla \cdot \mathbf{J}_p \tag{3.5}$$

where G_p is the generation rate for holes and R_p is the recombination rate.

- Excitations and responses are static and fully time–independent.

- All radiation is monochromatic and normal to the substrate such that secondary reflections (optical crosstalk) are negligible. Further, the radiation is absorbed in the base layer and generates carriers at a rate of

$$G_p(x, y, z) = \Phi(x, y)\alpha e^{-\alpha z} \tag{3.6}$$

where $\Phi(x, y)$ is the incident monochromatic photon flux per unit time per unit area, and α is a function of wavelength.

- The depletion approximation is employed.

- Defining the excess minority carrier concentration as

$$p' = p_n - p_{n0} \tag{3.7}$$

where p_{n0} is the thermal equilibrium concentration, low level injection (LLI) is assumed and the recombination is modeled as

$$R_p = \frac{p'}{\tau_p} \tag{3.8}$$

where τ_p is the hole lifetime. The hole diffusion length is defined by the usual expression

$$l_p^2 = D_p \tau_p \tag{3.9}$$

Analytic equations

Given the above assumptions, a single drift–diffusion equation may be derived for the excess minority carrier concentration

$$G_p(x, y, z) = \frac{p'}{\tau_p} + \mu_p E_z \frac{\partial p'}{\partial z} - D_p \nabla^2 p' \tag{3.10}$$

which is valid in the bulk of the material.

Along the boundaries of the domain, the concentration and/or the derivative of the concentration must be specified. At any junction, under zero bias, in the depletion approximation,

$$p' = 0 \tag{3.11}$$

Along passivation surfaces, the surface recombination velocity s is introduced so that

$$\mathbf{J}_h = qsp' \tag{3.12}$$

where s is normal to the surface. The current elsewhere is given by Equation 3.4. In particular, the current into the center diode is of interest. Introducing z_j to indicate points in z along the junction,

$$J_z|_{z=z_j} = q\mu_p p'(z_j) E_z - qD_p \frac{\partial p'}{\partial z}|_{z=z_j} \tag{3.13}$$

The photocurrent is then found by integrating $J_z(x, y, z_j)$ over the central diode depletion region surface

$$I = \int_{\text{junction}} J_z(x, y, z_j) dx dy \tag{3.14}$$

and the quantum efficiency is found by normalizing this current to the incident flux Φ.

3.1.2 Mathematical assumptions

The simulation is necessarily over a finite point set, preferably as small as possible so that computation times are short. Hence a symmetry argument is used to quarter the simulation domain, and artificial boundary conditions are used to bound the domain in x and y. Finally, the continuous solution, with these boundary conditions, is shown to exist and be unique.

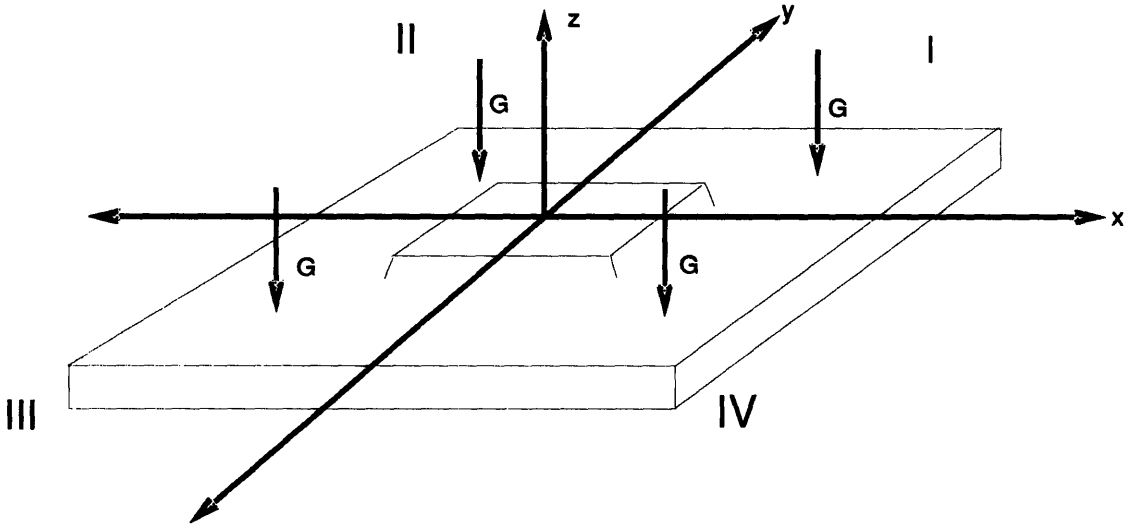

Figure 3-1: Symmetrically placed impulses force symmetric carrier and current density distributions. The xy origin is at the center of the junction.

Symmetry and linear superposition

Consider four spatial impulses of monochromatic radiation each of intensity G placed symmetrically about the origin as shown in Figure 3-1. The impulses are shown on the frontside for visual clarity, but the following argument holds for backside illumination. No current due to just impulses I and II will flow across origin plane YZ; similarly for impulses III and IV. This is then true for the pairs of impulses (I, IV) and (II, III): the normal current flow through origin plane YZ is zero;

$$\mathbf{J}(x = 0, y, z) \cdot \hat{i}_x = 0 \tag{3.15}$$

similarly for origin plane XZ.

There exists a certain minority carrier distribution throughout the material due to impulse I. The particular distribution is determined by the input, here $G\delta(x - x_0, y - y_0)$, the equations of the medium and the boundary conditions. If the charge distribution with only impulses I and II present is found, the current into the junction may be calculated. This current has a part due to impulse I and a part due to impulse II, and these parts are equal in magnitude. Similarly, when all four impulses are on, the current is just the sum of the four equal contributions. The solution to the medium's equation can also be determined by the boundary conditions. The carrier distribution in the presence of a reflecting boundary YZ is mathematically and physically indistinguishable from the distribution given the presence of a symmetrically located and symmetrically weighted impulse, as in the method of images often employed for electrostatic problems. Thus the response (the current)

due to the sum of the impulses is the same as the response due to one impulse with the symmetric boundary conditions at the XZ and YZ origin planes.

This introduces a new way to calculate the response to just one impulse. Employing the mirror boundaries, one may solve for the excess minority carrier concentration in just one quadrant. The distribution underneath the junction must be symmetric due to the symmetry of the excitation. Thus the distribution is known in all four quadrants. One then integrates J_z over the entire junction area, and then recognizes that this solution is the same as that arising from four symmetrically placed inputs. By dividing the current by four, the response to a single impulse is found. Then, if the response of the system to all possible spatial impulses is calculated, linear superposition gives the response to any input form which is symmetric about both the XZ and YZ origin planes.

Artificial boundary conditions

Figure 3-2 schematically illustrates the simulation domain. Real boundaries, like the substrate and passivation are treated by use of a surface recombination velocity, where the mesa cuts are approximated by perpendicular indentations. The mirror boundaries are one of the artificial boundaries, and are equivalent to surfaces with a recombination velocity of zero. The desired boundary conditions on the far edges would make the material seem forever continuous. Setting the carrier concentration to zero is not appropriate, since these walls are neither junctions nor Ohmic contacts. On the other extreme, reflecting boundaries would cause an abnormally high response (up to four times too large) due to impulsive illumination arriving near the edge, by the same arguments that drove the introduction of mirror boundary conditions. A so–called neutral boundary condition was chosen, where the boundaries are modeled as surfaces with $s = D_p/l_p$ to make them appear to be just more bulk material. In practice, an accurate response was desired for illumination distances under the nearest and next–nearest neighbor; more pixels would have been added to the simulation domain in order to make the response insensitive to the recombination velocity chosen on this far boundary.

Existence and uniqueness of the solution

Equation 3.10 is a second–order partial differential equation. As such, it could be expressed as a Sturm–Liouville problem, whose solution is an infinite series of eigenfunctions. For a given set of boundary conditions involving a linear combination of p' and its first derivative, this series converges to a solution which both exists and is unique [5].

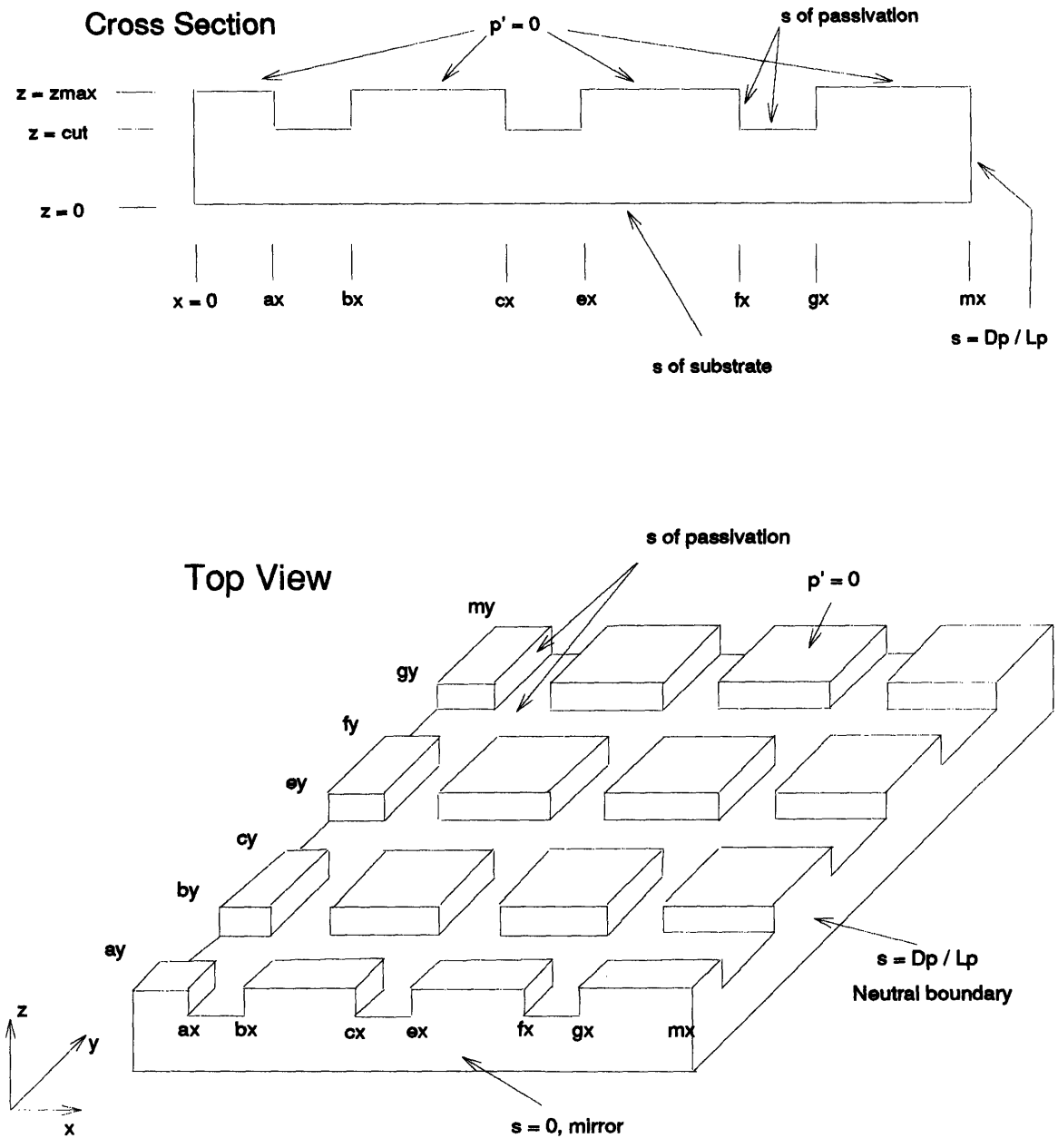

Figure 3-2: The simulation domain in cross section and top view. The top view shows the quarter of the full 7 by 7 pixel region over which the calculation takes place. Reflecting boundaries (mirrors) occur on the XZ and YZ origin planes. On the fourth pixel, in either x or y, the domain is terminated by a neutral boundary condition surface. The passivation and substrate recombination velocities may be independently allocated. All junctions are grounded so that the excess carrier concentration is zero.

3.1.3 Discretization

Bulk equation

The equations are normalized for convenience. First, a normalized carrier concentration u is introduced

$$u = \frac{D_p p'}{\Phi l_p} \tag{3.16}$$

All lengths are also normalized to the diffusion length l_p. Defining a parameter $\beta = \alpha l_p$, a fully normalized main equation may be written:

$$u = \beta e^{-\beta z} - \gamma_{dr} \frac{\partial u}{\partial z} + \nabla^2 u \tag{3.17}$$

where

$$\gamma_{dr} = \frac{q l_p E_z}{kT} \tag{3.18}$$

Standard finite difference techniques are used to discretize the equations on a uniform grid so that $\Delta x = \Delta y = \Delta z = \Delta$. For internal points, these approximations are used:

$$\frac{\partial u}{\partial z} = \frac{u_{k+1} - u_{k-1}}{2\Delta} + \mathcal{O}(\Delta^2) \tag{3.19}$$

$$\frac{\partial^2 u}{\partial z^2} = \frac{u_{k+1} - 2u + u_{k-1}}{\Delta^2} + \mathcal{O}(\Delta^2) \tag{3.20}$$

where subscripts are indicated only for those points where an index is changed from its default. Using i as the x index, j as the y index and k as the z index, this means that $u_{i,j-1,k}$ is written as just u_{j-1}. The main equation may then be written in discretized terms.

$$u = \frac{\Delta^2 \beta e^{-\beta z} - \frac{1}{2}\Delta\gamma_{dr}(u_{k+1} - u_{k-1}) + u_{i+1} + u_{i-1} + u_{j+1} + u_{j-1} + u_{k+1} + u_{k-1}}{(6 + \Delta^2)} + \mathcal{O}(\Delta^4) \tag{3.21}$$

Boundary conditions

In general, the surface recombination velocity boundary conditions can be rewritten as

$$\frac{\partial u}{\partial \chi}|_{\text{boundary}} = (\pm\gamma_s \pm \gamma_{dr})u \tag{3.22}$$

where χ indicates one of the three spatial dimensions, and the γ_{dr} is included if the boundary occurs in z and the signs are chosen based on the direction of s. The normalized surface recombination parameter is given by

$$\gamma_s = \frac{s\tau_p}{l_p} \tag{3.23}$$

The boundary condition in the case of mirrors is slightly simplified since, on the YZ mirror, for example, one may note directly that

$$\frac{\partial u}{\partial x} = 0 \tag{3.24}$$

$$\frac{\partial^2 u}{\partial x^2} = \frac{2u_{i+1} - 2u}{\Delta^2} + \mathcal{O}(\Delta^2) \tag{3.25}$$

where in this instance $i = 0$.

These boundary conditions are typically introduced via the second derivative in this way

$$\frac{\partial^2 u}{\partial x^2} = \frac{1}{2\Delta^2}(-7u + 8u_{i+1} - u_{i+2} - 6\frac{\partial u}{\partial x}\Delta) + \mathcal{O}(\Delta^2) \tag{3.26}$$

or via the first derivative if appropriate

$$\frac{\partial u}{\partial x} = \frac{1}{2\Delta}(-3u_i + 4u_{i+1} - u_{i+2}) + \mathcal{O}(\Delta^2) \tag{3.27}$$

where these equations would treat derivatives at $x = 0$.

The boundaries can occur in either one, two, or three dimensions, so equations are combined where appropriate. A large fraction of the dif3d.c source code which implements the simulation is devoted to allocating the 192 special cases which result from the boundaries and the chosen geometry.

Error terms in the expansions

It may be shown that the main expression for u, Equation 3.21, and all other expressions on boundaries are accurate to $\mathcal{O}(\Delta^4)$ in the Taylor series expansion. From the carrier concentration u, the current density is calculated via $\partial u/\partial z$, which is only accurate to $\mathcal{O}(\Delta^2)$. However, when the current density is integrated over the junction area, a factor of Δ^2 enters and the collected current has the form

$$I = I_0 + \mathcal{O}(\Delta^4) \tag{3.28}$$

where the subscript indicates the correct value. While this current has already been normalized to the flux, it remains to be normalized either to the diode area or the illuminated area. The area can only be specified to a precision of an integer multiple of Δ^2. In the case of the diode impulse response, or dir(x), the normalized illuminated area is just Δ^2. Hence the final product, the quantum efficiency, is only valid to

$$\eta = \eta_0 + \mathcal{O}(\Delta^2) \tag{3.29}$$

Typically the points are chosen to have a density of one point per micron in each dimension, so geometries can be laid out without ambiguity. The variation of efficiency with grid size is reported in Subsection 3.2.2.

Convergence and overrelaxation

Once the equations have been allocated to the grid points, the program simply steps through each point, doing the arithmetic. The new solution is emphasized over the old solution, however, as follows

$$u_{\text{new}} = 1.93 u_{\text{just calculated}} - u_{\text{previous}} \tag{3.30}$$

for each point. This is done to increase the rate of convergence of the u matrix with each iteration. The factor of 1.93 was empirically found to provide fastest convergence. When the sum of the absolute values of the difference between u_{new} and u_{previous} is less than a small number ϵ,

$$\sum_{\text{whole grid}} |(u_{\text{new}} - u_{\text{previous}})| \leq \epsilon \tag{3.31}$$

the solution is said to converge. The simulation has always converged in practice, except in an attempt to leave the "far" boundary conditions unspecified. The analogous continuous problem for that case is not guaranteed to have a solution.

3.2 Use of the numerical model

3.2.1 Provisions

The dif3d.c code provides for modeling rectangularly symmetric geometries and excitations. The user can simulate monochromatic flood, point, or slit illumination responses. The following parameters are alterable:

- Temperature
- Hole lifetime
- Diffusion length
- Absorption coefficient
- Field
- Substrate and passivation surface recombination velocity
- Number of diodes, from a 1×1 to a 7×7 total array of rectangular pixels, as long as the geometry is symmetric about the mirrors.
- Mesa delineation depth
- Base layer thickness

3.2.2 Verification

A theoretical proof of the discrete solution's convergence is not given here, but some evidence about the convergence is presented. By "independent of" or "matches" less than a 1% variation shall be meant. It is found that:

For either the case of very large area diodes, or close packed diodes without trench separation, the quantum efficiency converges to the usual one–dimensional analytical case.

The integrals of either the slit or the impulse responses over the whole domain consistently match the flood illumination response.

The responses are linear (when ϵ is also scaled), independent of overrelaxation factor, order of point evaluation, far edge surface recombination velocity and impulse response illumination area.

The response to a point on axis need only be divided by two instead of four, and the flood illumination and origin point responses require no such division.

Geometries symmetric about the diagonal have a similarly symmetric response function.

The responses are dependent on the the combination of ϵ and Δ. The results of varying Δ are shown in Figures 3-3 and 3-4. No formal effort was made to extrapolate the infinite point solution. Typically, grid sizes are about 200,000 points, $\Delta = 1$ μm and $\epsilon = 1$ for flood illumination. Slit illuminations are weighted by a factor of 100, and point illuminations by 10^4, since a grid plane usually contains about 10^4 points, and the desire is for roughly the same number of iterations to be used on either the flood, slit, or point response.

3.2.3 Operational constraints

Hardware and Software requirements

The code is a straightforward implementation in ANSI C, making it reasonably machine portable. Sun C++ 2.1 was used on a Sun SPARCstation2 with 32 MB of RAM for both the compilation (optimized by C++) and running of the code. Memory rapidly becomes an issue since each point in the grid uses 20 bytes. Hence point densities like 5 points per μm are unachievable. The code output files were set up to be easily read by the software *Mathematica*, where transforms, plotting, and other manipulations were performed.

Time requirements

Since a non-adaptive mesh is used, the grid is large, as previously noted. Calculation of a single point in a response function takes 5–11 minutes depending on the specific problem. Hence a typical flood response may take five minutes, a typical slit response, four hours, and a full diode impulse response, four days. Compilation to generate optimized machine code takes about three or four minutes. Most of the MTF information desired can be obtained from running just slit scan simulations.

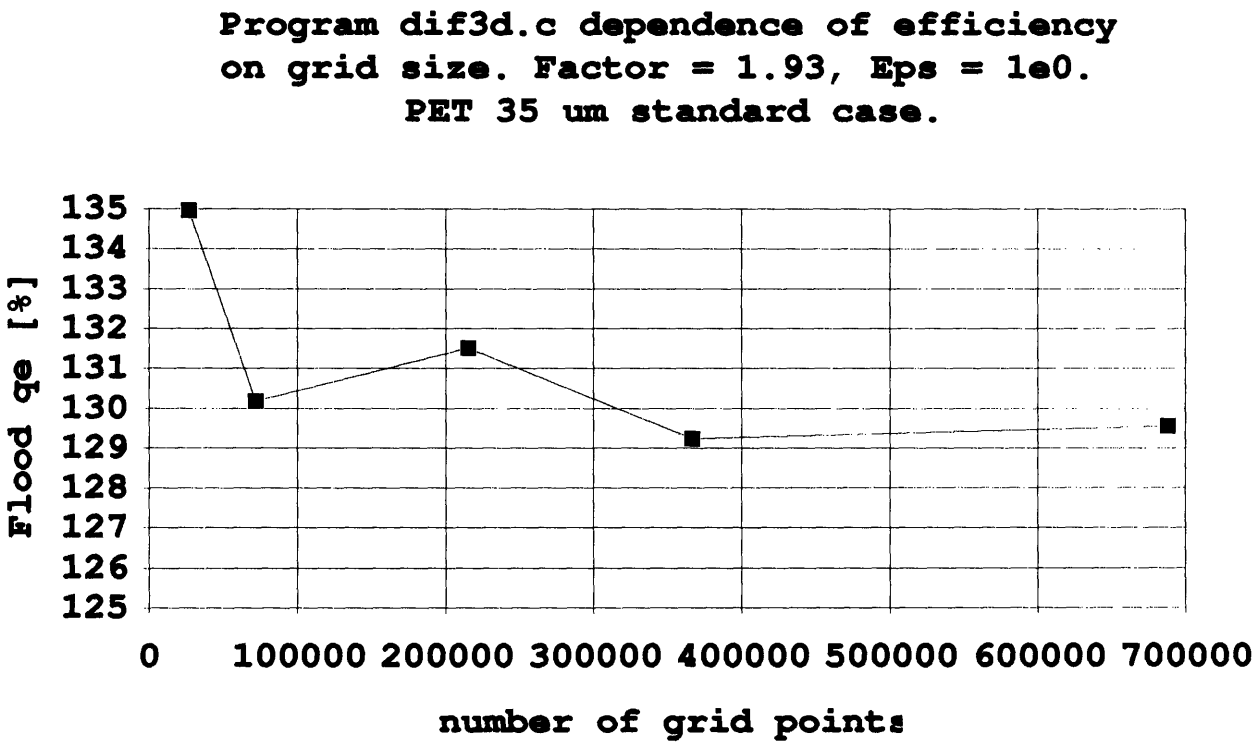

Figure 3-3: Flood illumination quantum efficiency variation with u grid size. The quantum efficiency is expected to converge to a single value as the grid size tends to infinity. All error terms in the Taylor series expansions vanish in that limit.

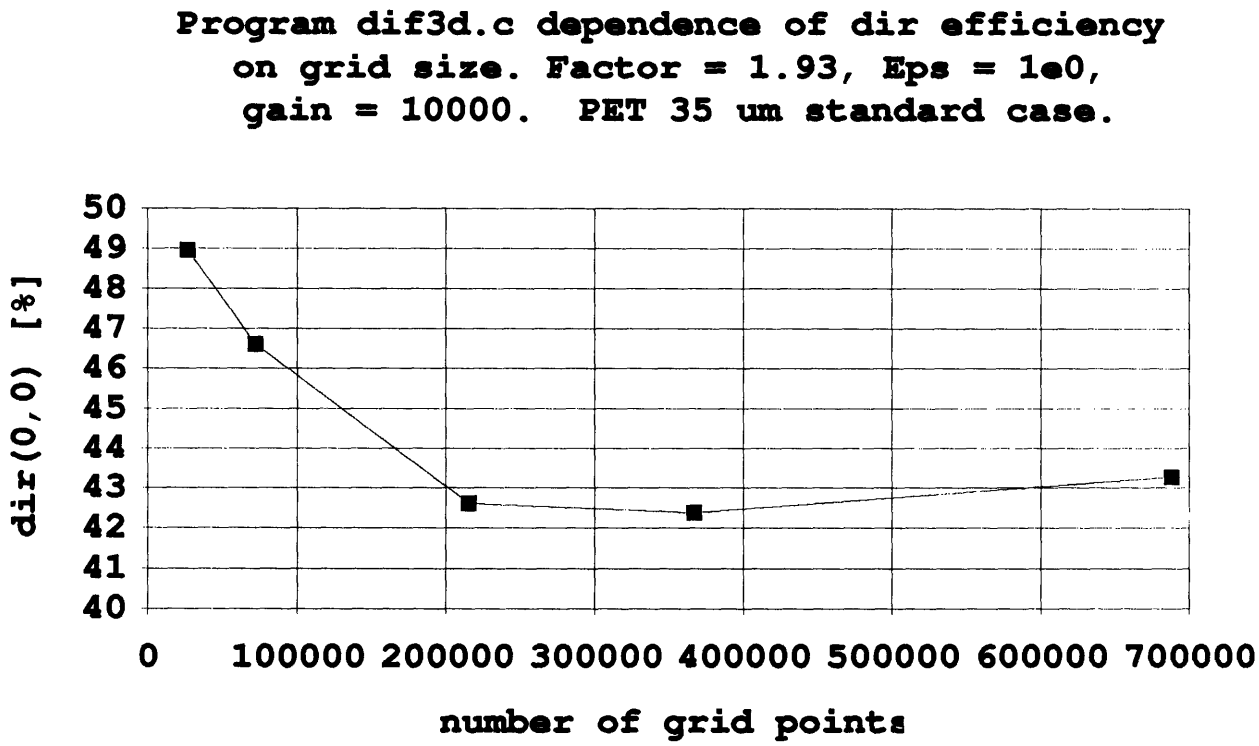

Figure 3-4: Diode impulse response, dir(0, 0), quantum efficiency variation with u grid size. The quantum efficiency is expected to converge to a single value as the grid size tends to infinity. All error terms in the Taylor series expansions vanish in that limit.

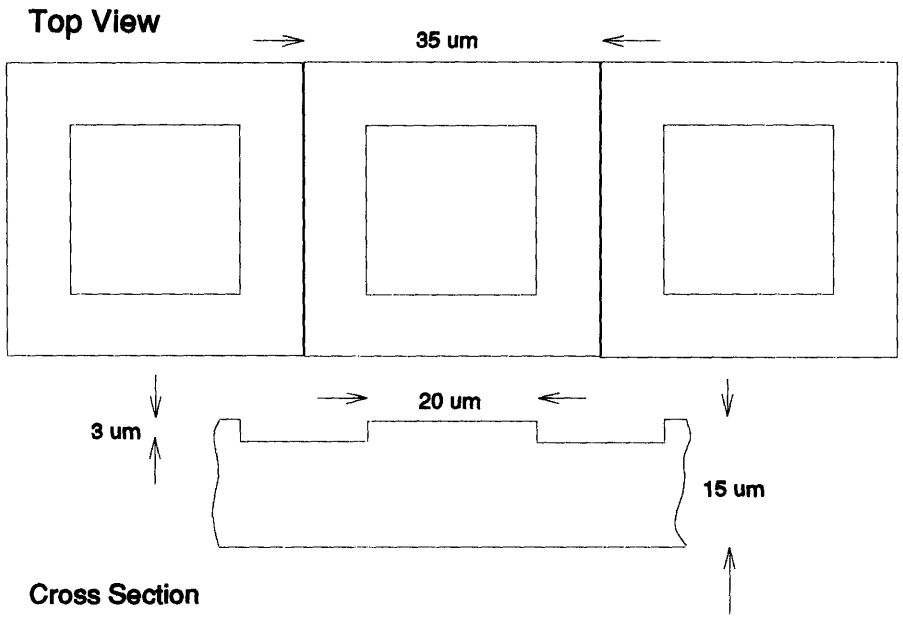

Figure 3-5: Schematic of the Small Staring Array 35 μm sparse geometry.

3.3 Results for a symmetric staring array

As symmetric staring arrays are likely to be the core of many "second-generation" (photovoltaic) IISs, a typical small area photodiode array was chosen for simulation. The geometry is shown in Figure 3-5.

3.3.1 Standard case MTF(f_x, f_y)

As an example of results, a standard case was defined with the geometry of Figure 3-5 and the following parameters: kT/q = 6 mV, α = 2000/cm, l_p = 15 μm, τ_p = 1 μs, E_z = 8 V/cm, $s_{\text{substrate}}$ = 0 and $s_{\text{passivation}}$ = 100 cm/s. This square staring array is symmetric in x and y. The flood illumination response was calculated as 53.7% with respect to the 35 μm × 35 μm cell area and 164% with respect to the 20 μm × 20 μm mesa area.

The direct and frequency space responses of this pixel are presented. It should be noted that the Fourier transform of the slit response function yields a profile MTF, that is

$$\mathcal{F}\{\int_{y=-\infty}^{y=+\infty} h(x,y)dy\} = H(f_x, 0) \tag{3.32}$$

The results presented here are found to agree with this theorem. The direct space data were discrete Fourier transformed in *Mathematica* on the SPARCstation2. Aliasing is assumed to be negligible for these data taken on 4 μm steps. Figure 3-6 shows a theoretical diode response to LWIR illumination

by an infinitesimally thin slit, traversing the diode in the x direction. Figure 3-7 is its transform, the diode profile MTF in the x direction. Figures 3-8 and 3-9 are the analogous data for y. Since the x and y directions are symmetric, these curves match the curves for x exactly. Figures 3-10 and 3-11 show the response due to an infinitesimally small LWIR spot in the just the x and the y directions. Figure 3-12 shows the entire response for all x and y. Figure 3-13 shows a profile slice of the full two–dimensional MTF. This matches 3-7, the transform of the slit response, exactly. Figure 3-14 indicates the profile slice for the y direction, matching with Figure 3-9. Finally, Figure 3-15 shows the full Small Staring pixel MTF, the transform of the response given in Figure 3-12.

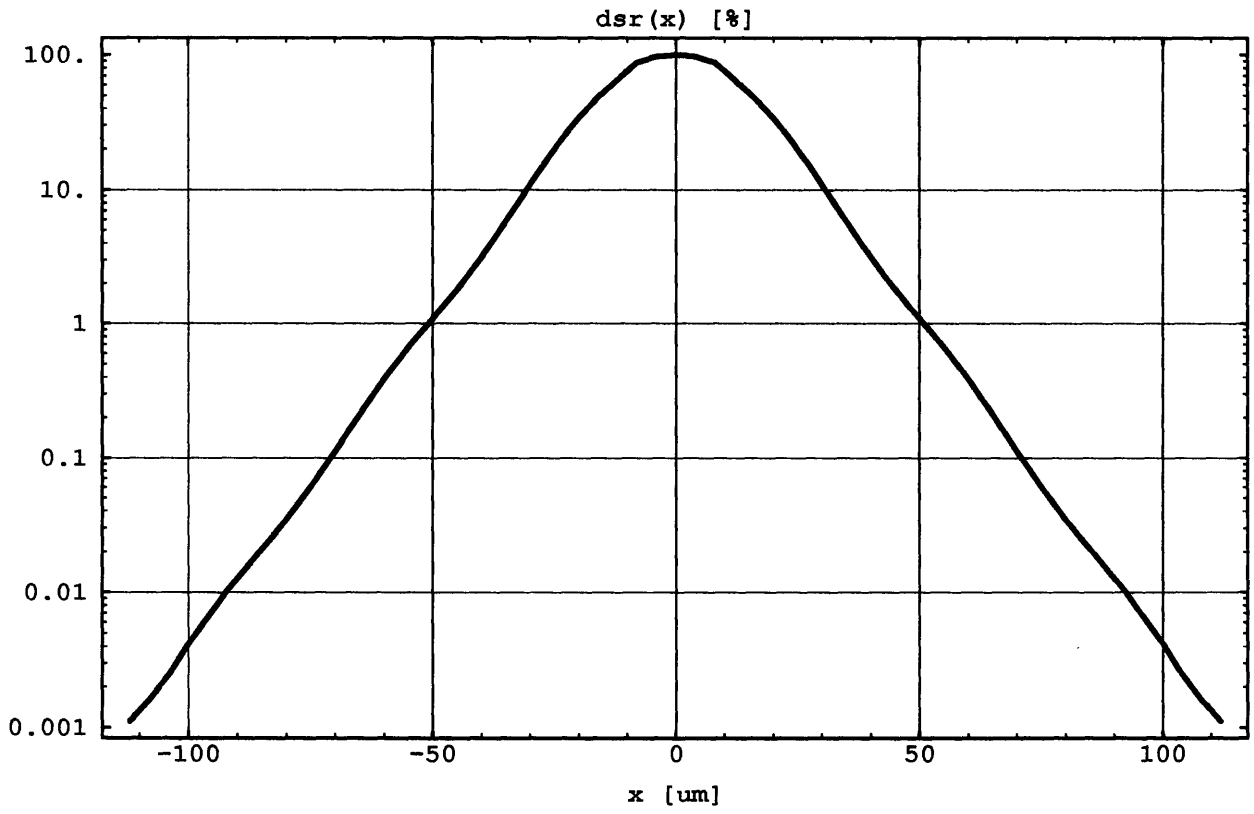

Figure 3-6: Small Staring Array simulation. The diode slit response(x) is the normalized collected photocurrent versus location of an infinitesimally thin slit of LWIR illumination. Its transform is the x direction profile MTF of the diode.

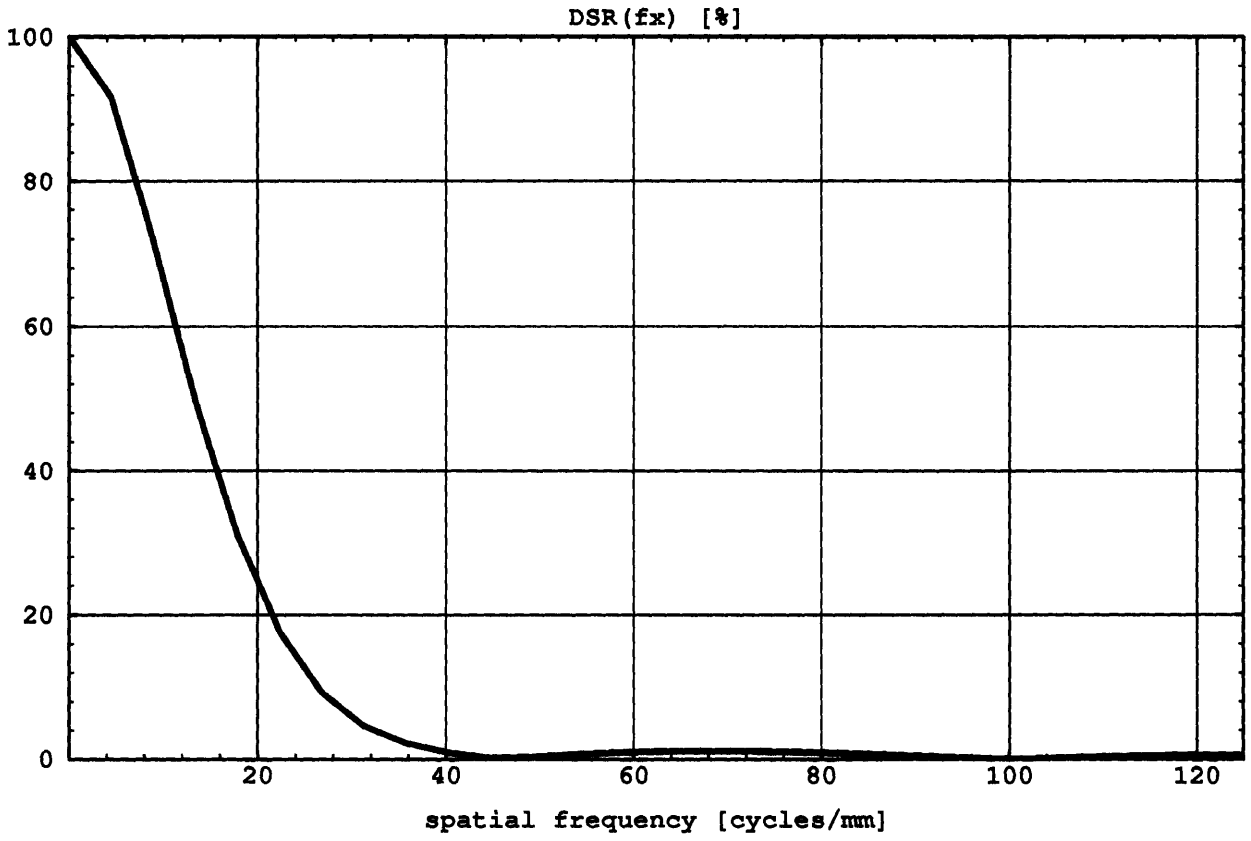

Figure 3-7: Small Staring Array simulation. The Diode Slit Response(f_x) is the profile MTF of the diode in the x direction.

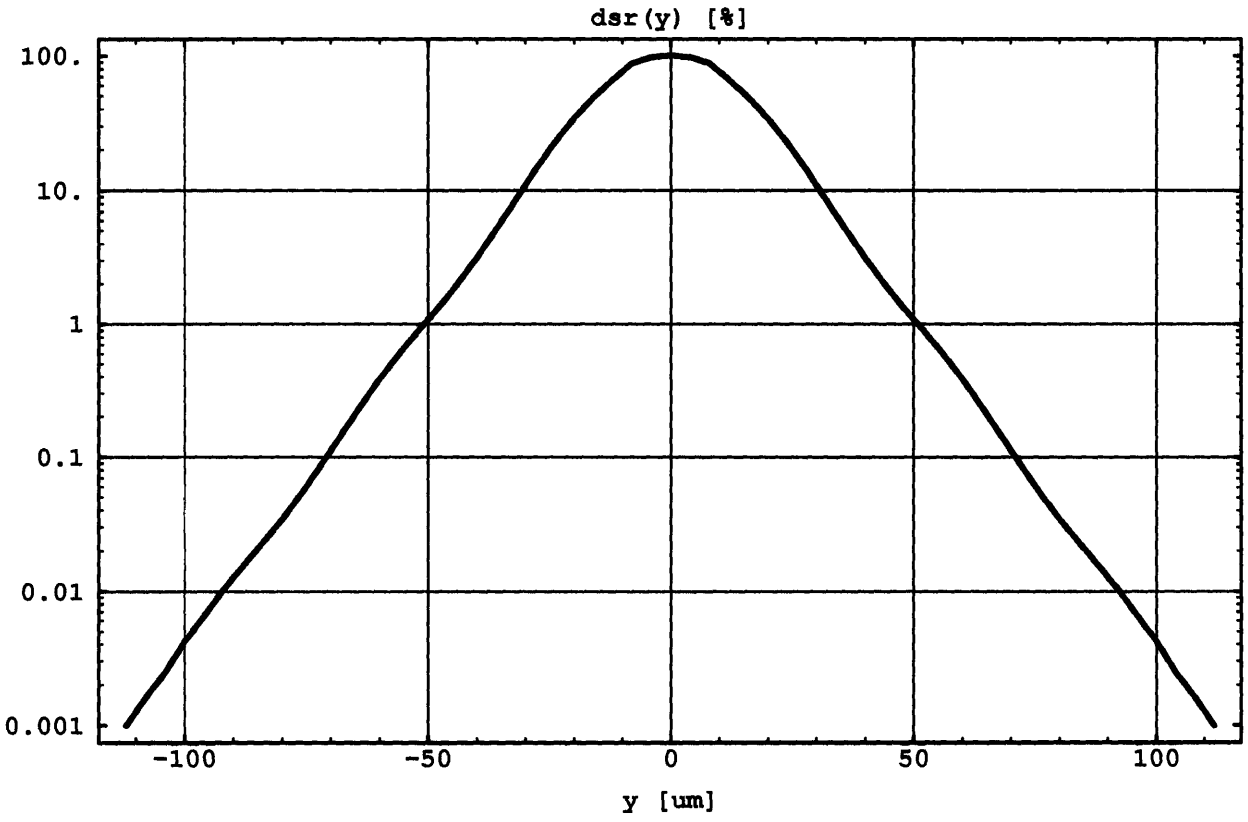

Figure 3-8: Small Staring Array simulation. Diode slit response(y). Here the slit is scanned across the y direction. Since this array is symmetric in x and y, the responses for both directions are the same.

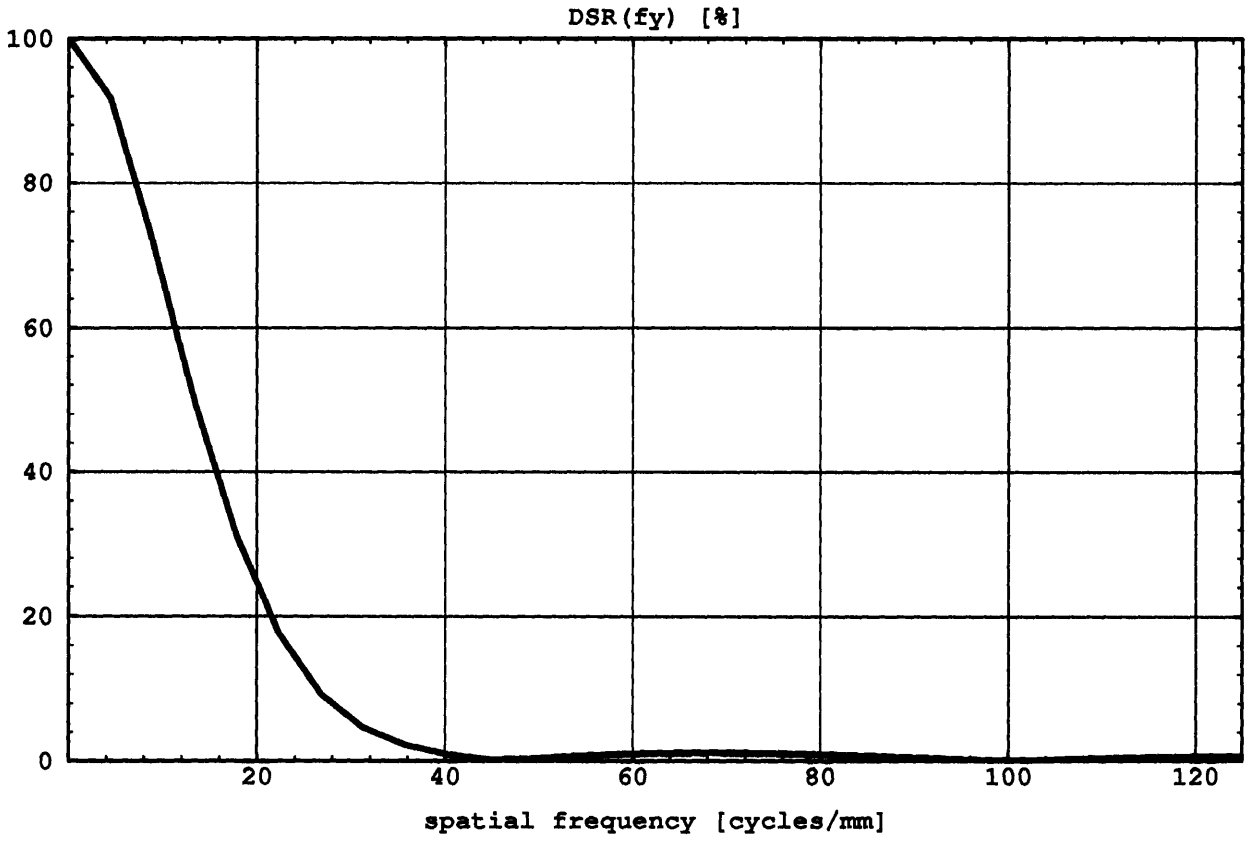

Figure 3-9: Small Staring Array simulation. Diode Slit Response(f_y), the profile MTF in the y direction, which is by symmetry the same as that in the x direction.

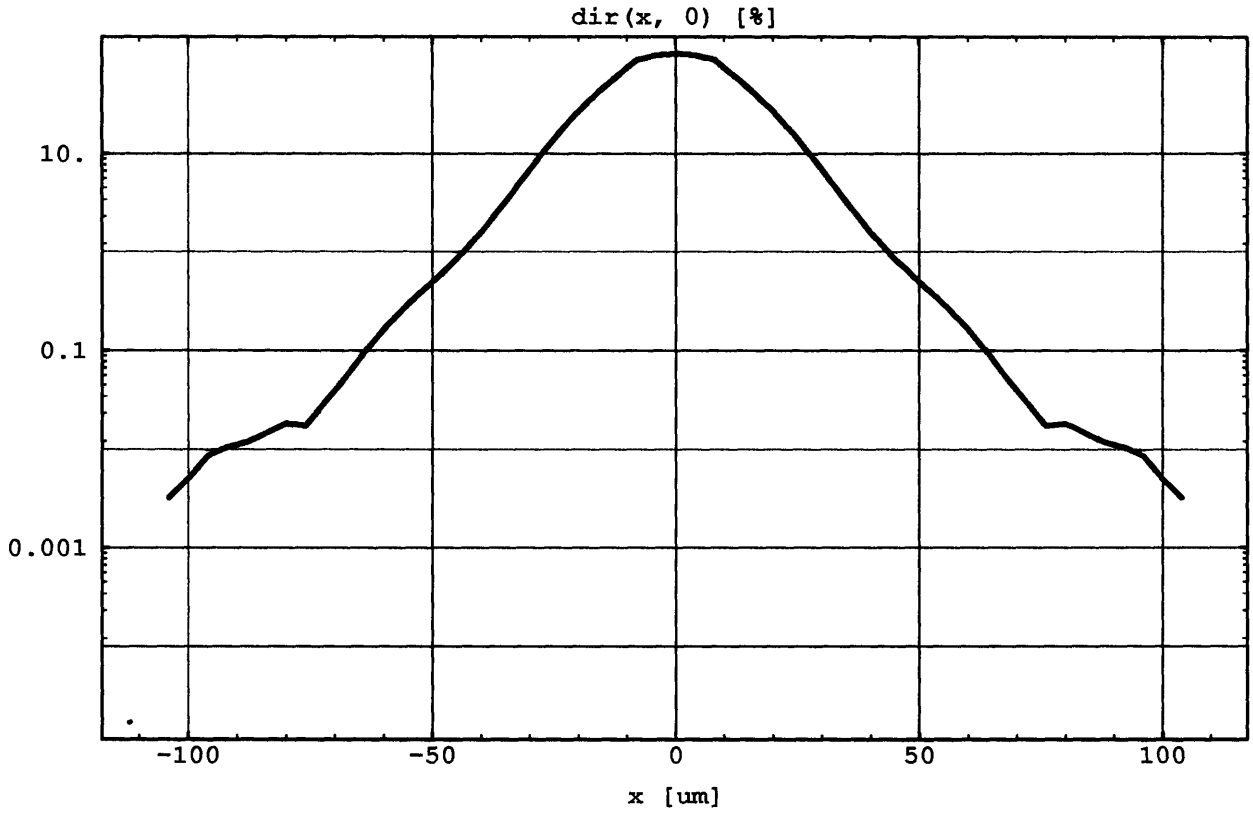

Figure 3-10: Small Staring Array simulation. The diode impulse response$(x, 0)$ is the normalized collected photocurrent versus location of an infinitesimally small spot of LWIR illumination. Here the response is shown versus the location of this spot along the x axis. This corresponds to a "perfect" spot scan in x.

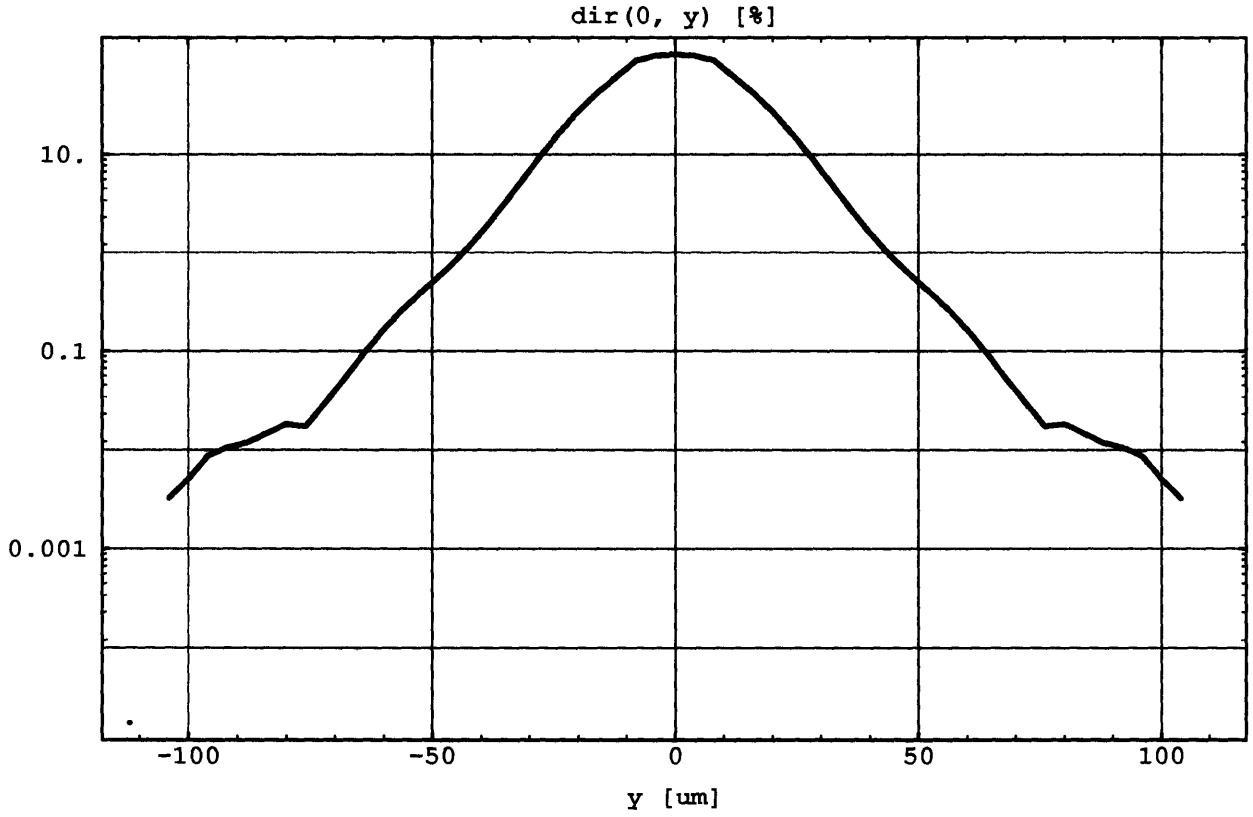

Figure 3-11: Small Staring Array simulation. Diode impulse response$(0, y)$. Here the response to a infinitesimal spot is shown versus spot location along the y axis. This corresponds to a "perfect" spot scan in y.

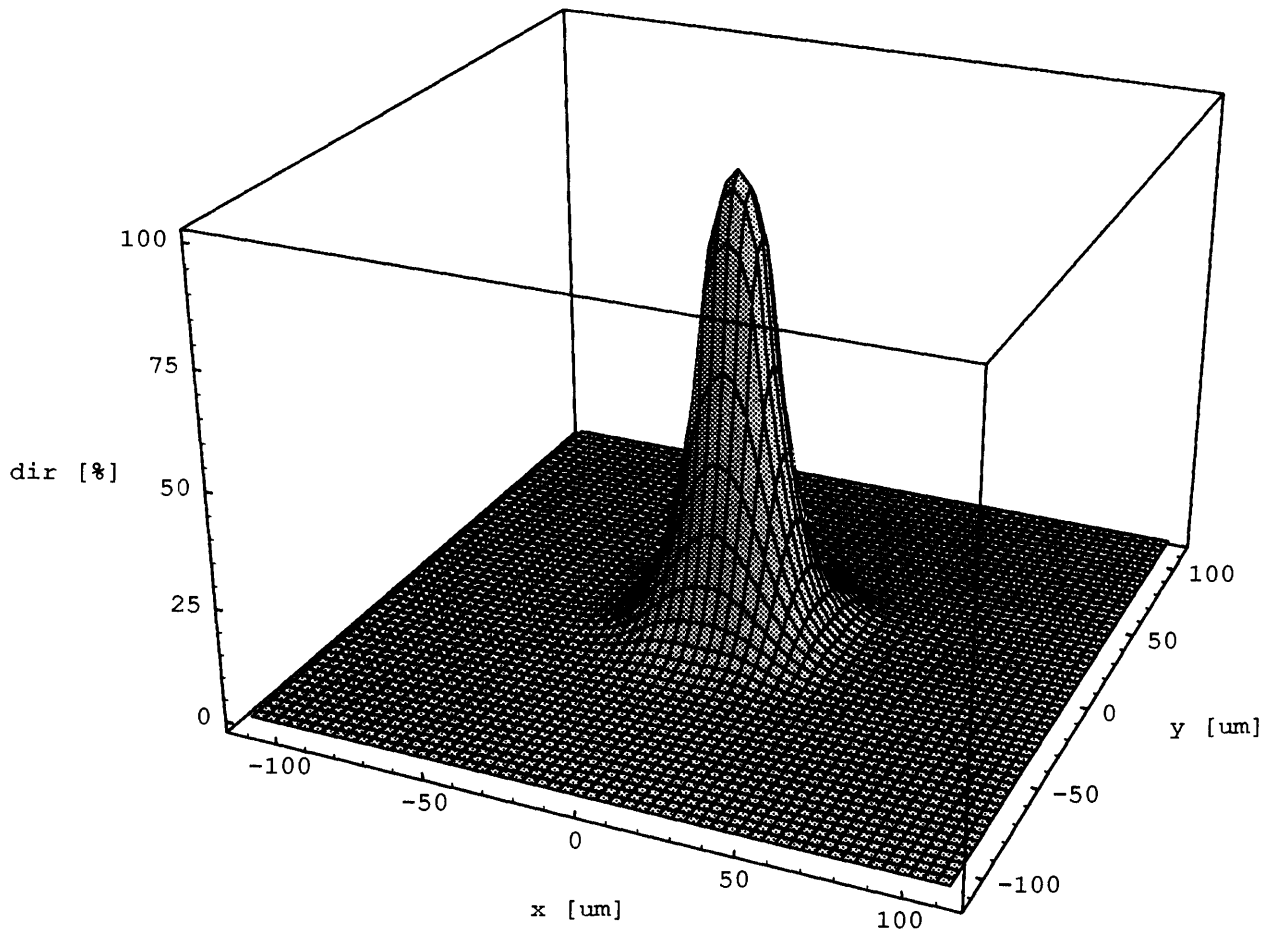

Figure 3-12: Small Staring Array simulation. The diode impulse response(x, y) is the full scan of the diode in x and y by an infinitesimally small spot.

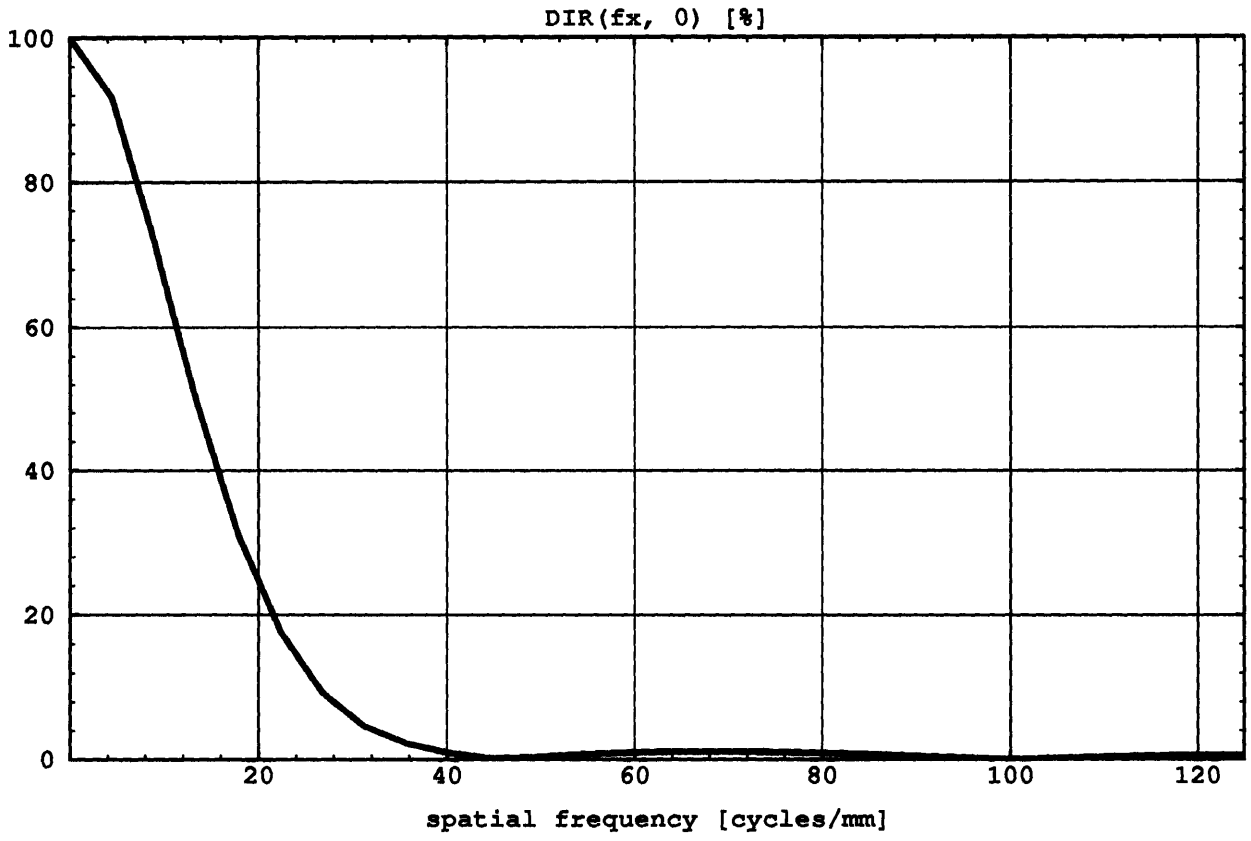

Figure 3-13: Small Staring Array simulation. The Diode Impulse Response($f_x, 0$) is the f_x axis profile slice through the full two-dimensional MTF. It is equivalent to the transform of the slit response.

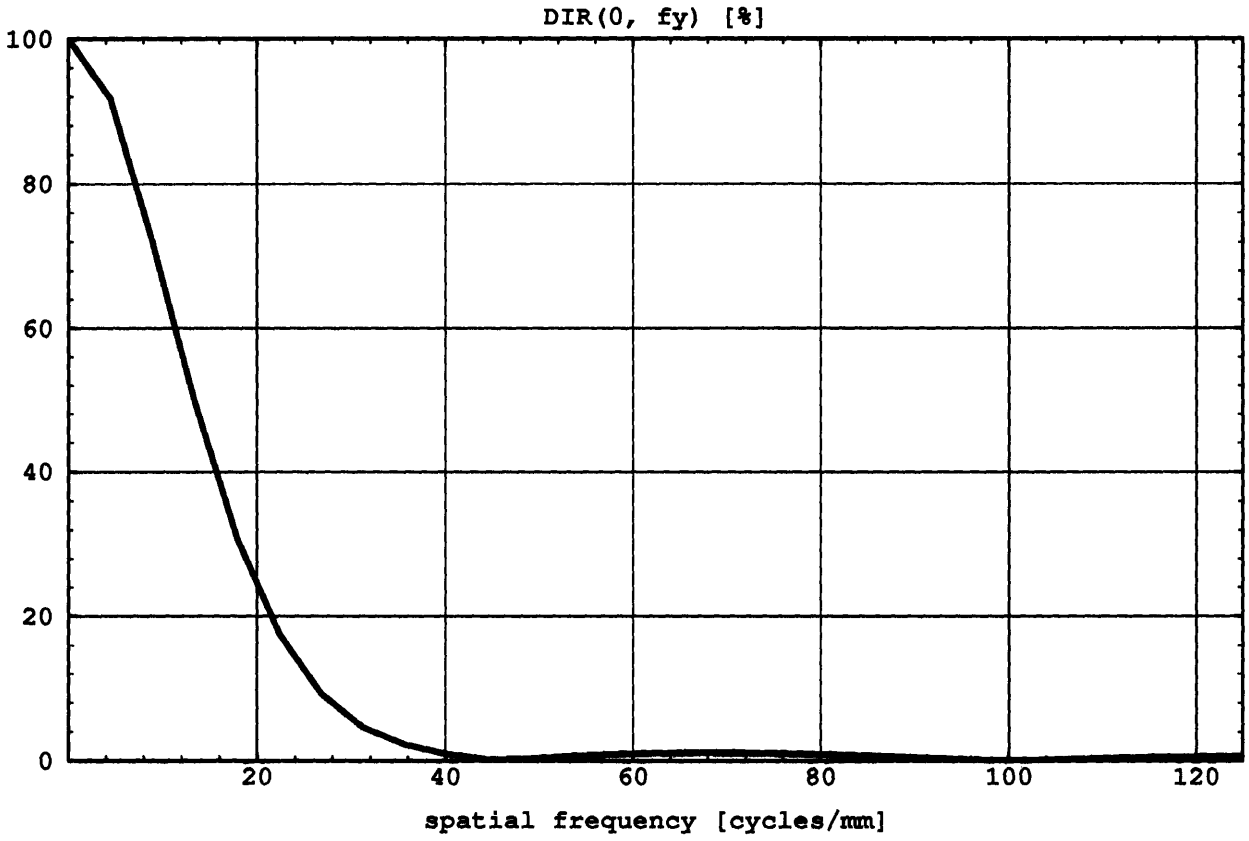

Figure 3-14: Small Staring Array simulation. The Diode Impulse Response$(0, f_y)$ is the f_y axis profile slice through the full two–dimensional MTF. It is equivalent to the transform of the slit response.

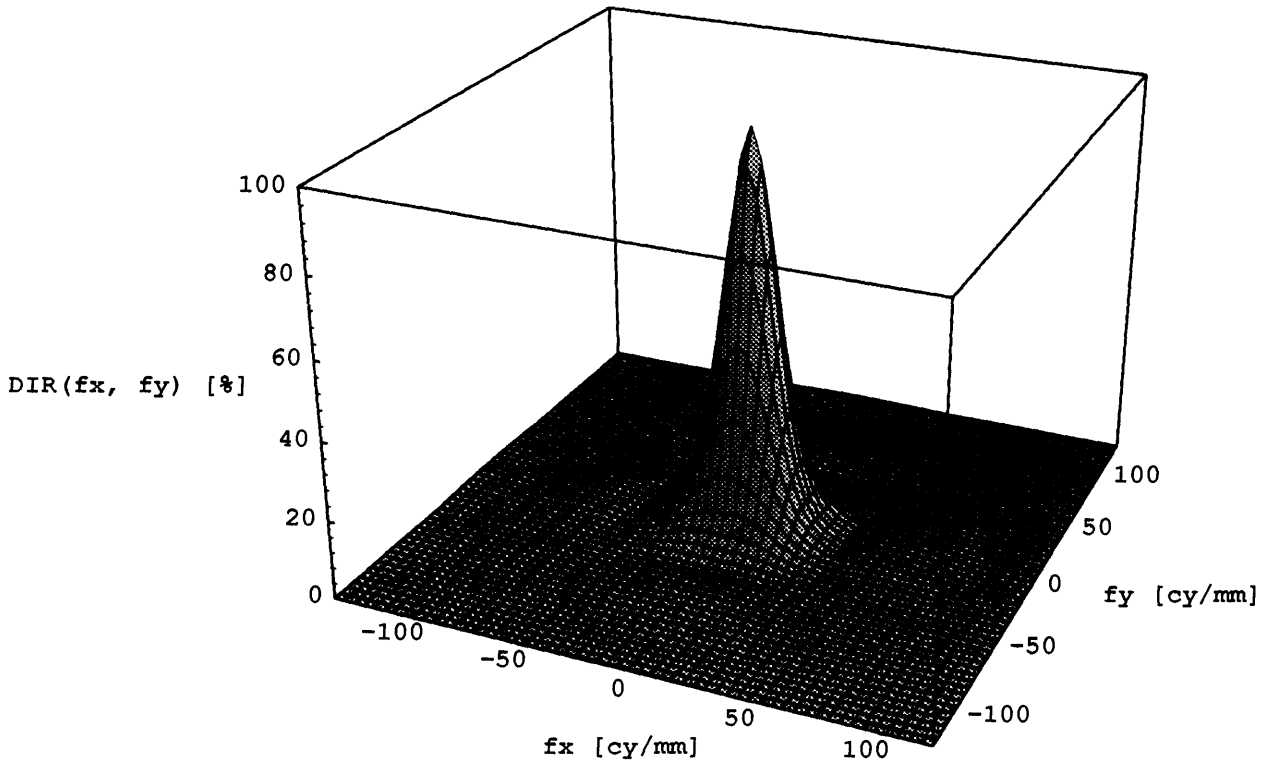

Figure 3-15: Small Staring Array simulation. The Diode Impulse Response(f_x, f_y) is the normalized Fourier transform of the dir(x, y). This is the full two–dimensional MTF of the diode.

3.3.2 Parameter variations

The main objective of this investigation was to find ways to improve small pixel MTF and examine the small pixel MTF design space. Permutations of one parameter at a time were made and slit scan simulations were run, generating the profile, or on–axis MTF. Both physical parameters, specifically α, l_p, E_z, and s as well as geometric parameters such as base thickness, cut depth, and pitch/mesa size ratio were changed. All the variations which increase MTF, except for pitch/mesa size ratio and collection enhancing field, tend to decrease flood illumination quantum efficiency. Figure 3-16 shows the results of varying the absorption coefficient on diode MTF. The calculated MTF increases with decreased α, as the carriers are photogenerated closer to the junctions. The influence of diffusion length is given in Figure 3-17, with MTF behaving inversely with diffusion length as expected. Figure 3-18 shows the strong influence of composition gradient field on MTF. The composition gradient arises from melt depletion of Cd as the film is grown. Estimates based on typical LPE growth by LIRIS personnel show an x–value gradient of $0.0005/\mu$m, which is consistent with SIMS (Secondary Ion Mass Spectroscopy) data. This gradient yields an electric field of 8 V/cm magnitude. This field essentially makes the diffusion of carriers anisotropic, directing carriers closer to the junction. Frontside (passivation) surface recombination velocity aids the MTF as shown in Figure 3-19. The ideal passivation case of $s = 0$ is included for reference. The recombination velocity is estimated at about 1000 cm/s for ZnS passivation, and about 100 cm/s for CdTe. Base thickness is changed in Figure 3-20, influencing the MTF relatively strongly. Figure 3-21 shows the effects of changing the mesa cut depth, which is far less influential since it does not bring the junctions closer to the light source. Finally Figures 3-22, 3-23, and 3-24 show the influence of varying mesa size on MTF, for the pitches of 20 μm, 25 μm, and 35 μm respectively. The influence of mesa size appears small, and an explanation is proposed in the discussion.

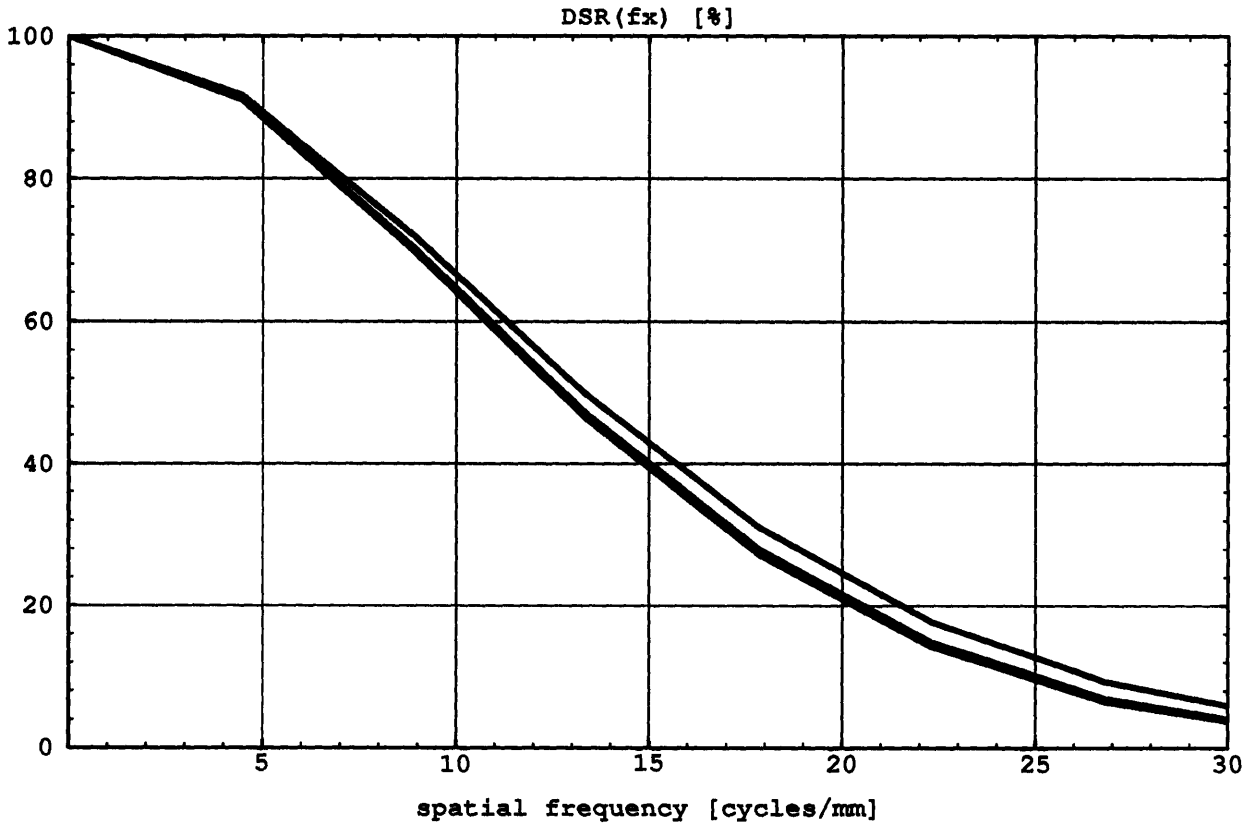

Figure 3-16: Small Staring Array simulation. varying the absorption coefficient. Upper curve, $\alpha =$ 2000/cm; Middle, 5000/cm; Lower, 10000/cm. The lower coefficient allows photogeneration closer to the junction, thus increasing MTF.

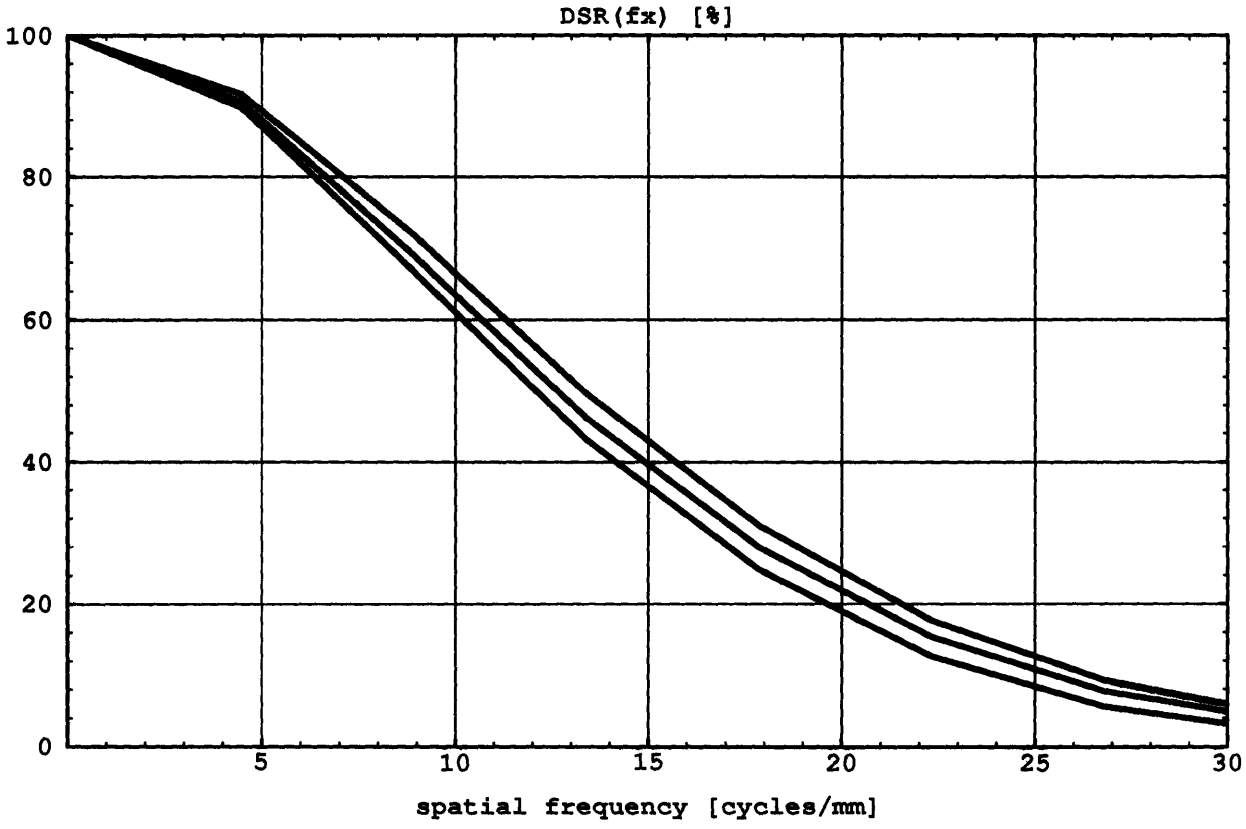

Figure 3-17: Small Staring Array simulation, varying the diffusion length. Upper curve, $l_p = 15$ μm; Middle = 20; Lower = 25. Increased diffusion length allows carriers to diffuse to other cells, thus degrading MTF.

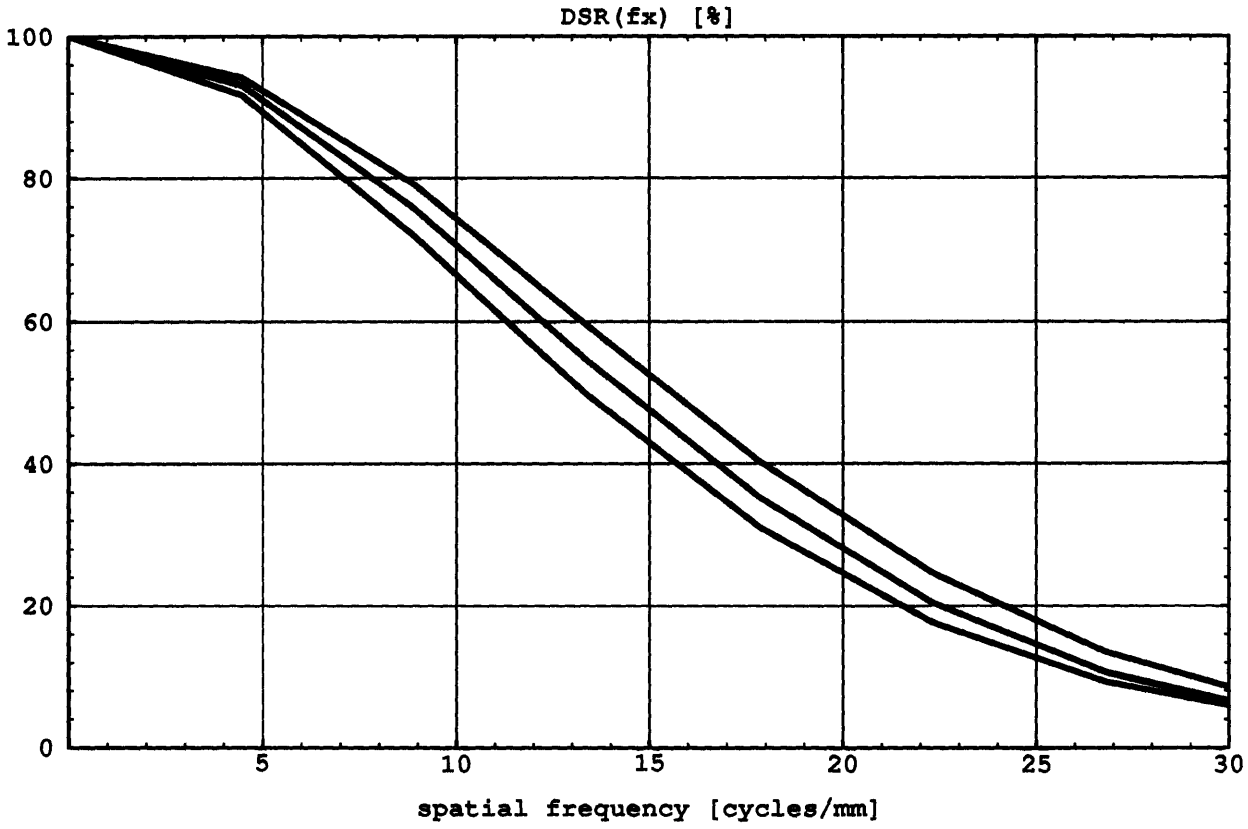

Figure 3-18: Small Staring Array simulation, varying the collection enhancing field. Upper curve, E_z = 24 V/cm; Middle, 16; Lower, 8. The field forces the carriers toward the junctions, increasing MTF.

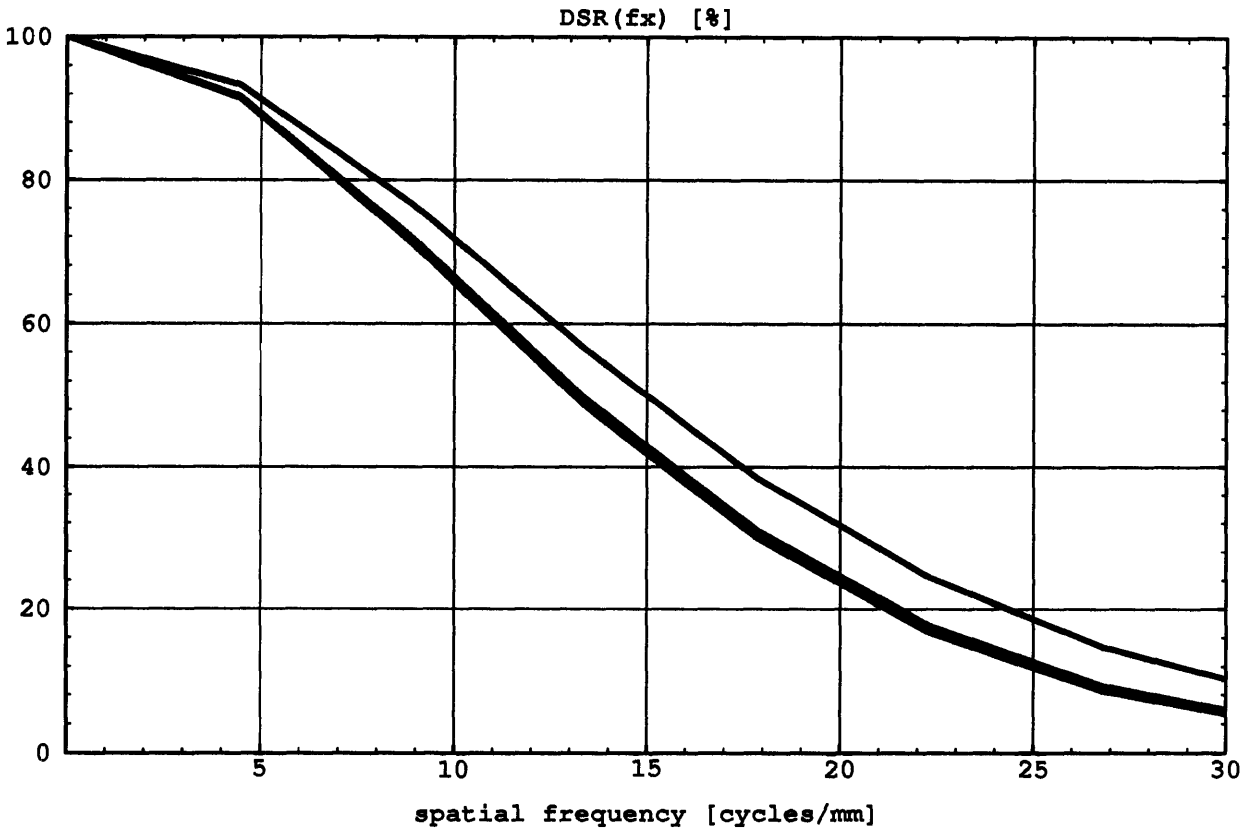

Figure 3-19: Small Staring Array simulation, varying the surface recombination velocity. Upper curve, s = 1000 cm/s; Middle, 100 cm/s; Lower, 0 cm/s. Increased velocities tend to shrink the width of the diffusion point spread function, thus increasing MTF.

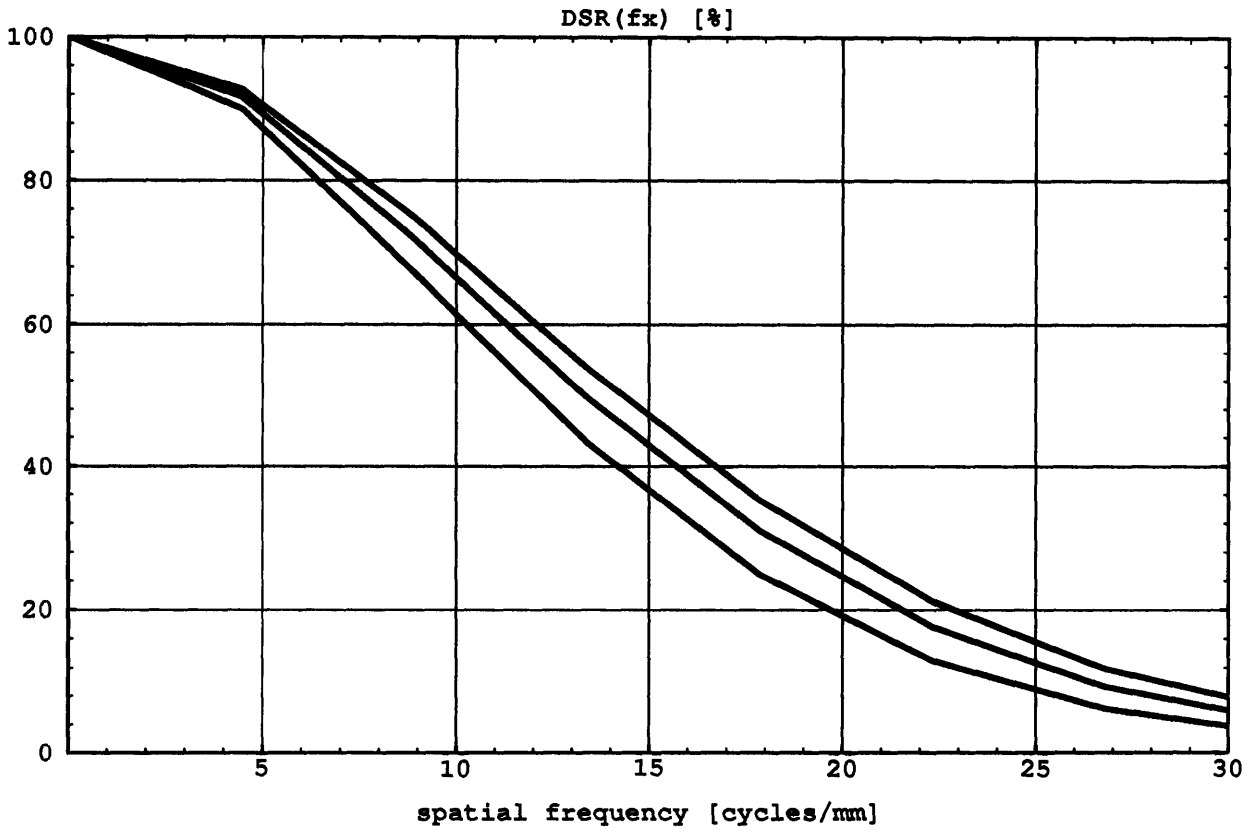

Figure 3-20: Small Staring Array simulation, varying the base layer thickness. Upper curve, Base thickness = 12 μm; Middle, 15; Lower, 20. The thin base layers increase MTF by bringing the junctions closer to the photogeneration.

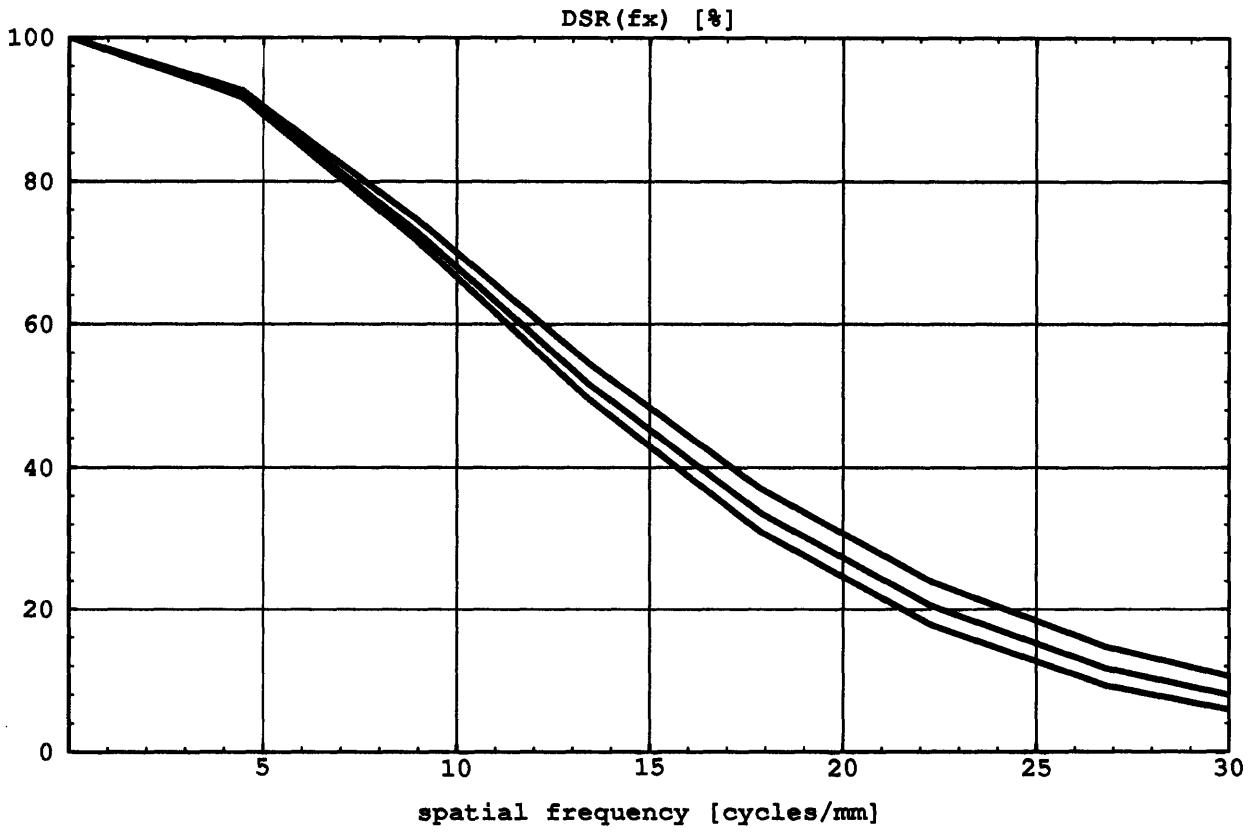

Figure 3-21: Small Staring Array simulation, varying the mesa cut depth. Upper curve, Cut depth = 7 μm; Middle, 5; Lower, 3. As the cut depth is increased, junctions become more spatially isolated, increasing MTF.

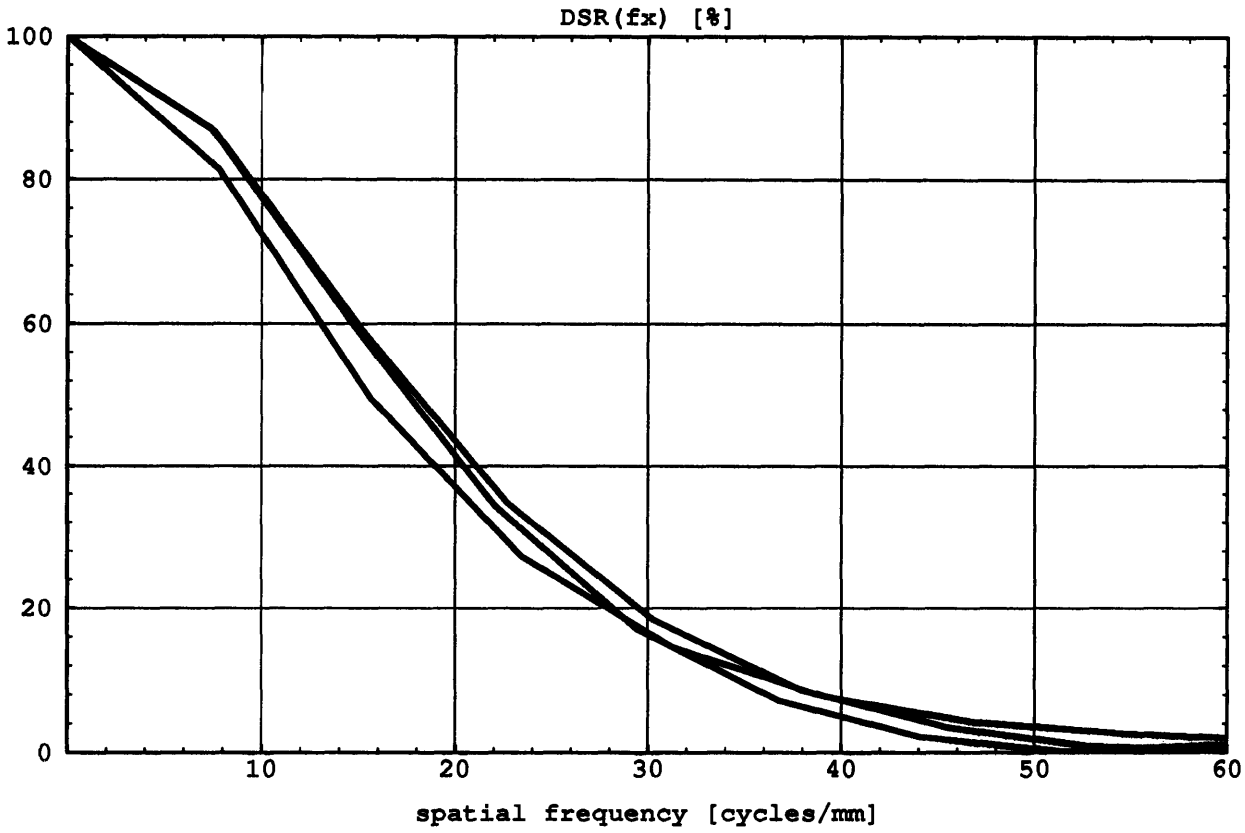

Figure 3-22: Small Staring Array simulation, 20 μm pitch, varying the pitch/mesa ratio. At the array Nyquist frequency of 25 cycles/mm: Upper curve, Mesa of 16 μm; Middle, 20; Lower, 10. Discussed in text.

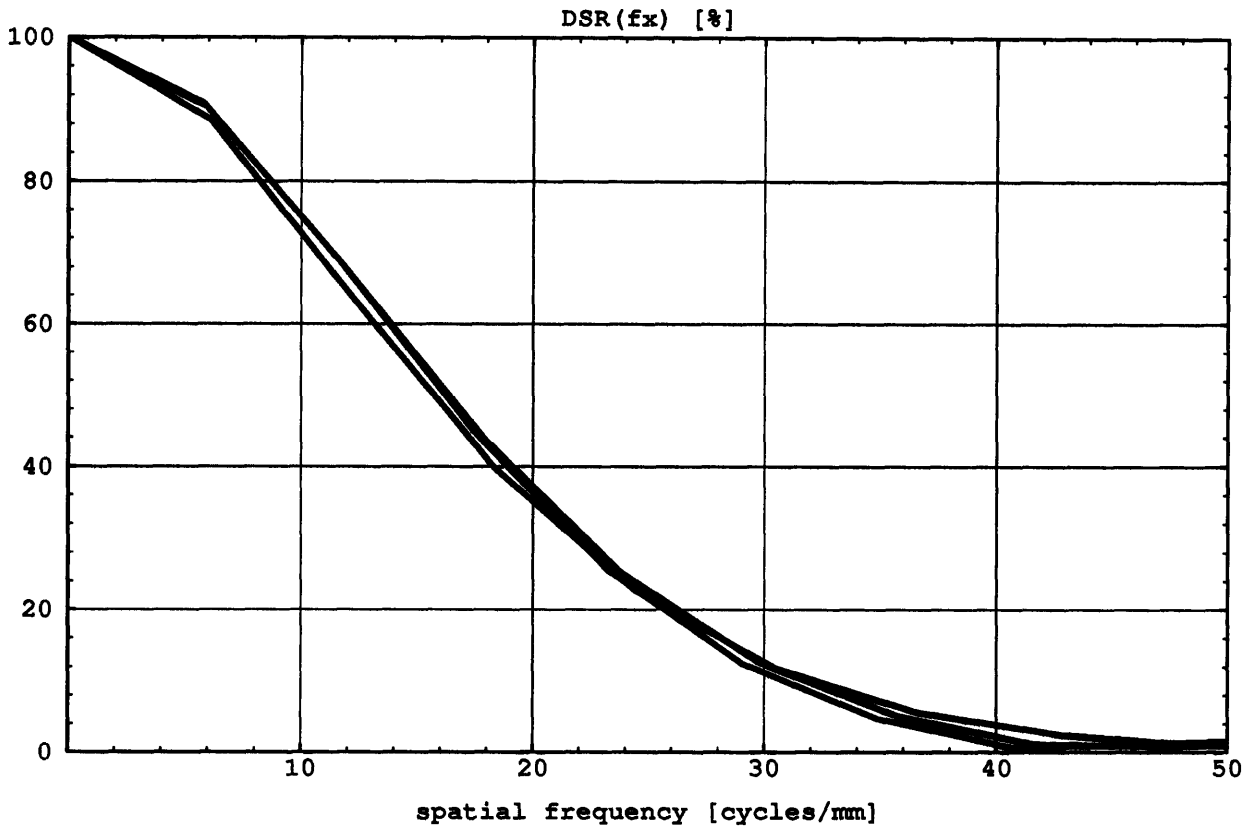

Figure 3-23: Small Staring Array simulation, 25 μm pitch, varying the pitch/mesa ratio. At the array Nyquist frequency of 20 cycles/mm: Upper curve, Mesa of 20 μm; Middle, 25; Lower, 16. Discussed in text.

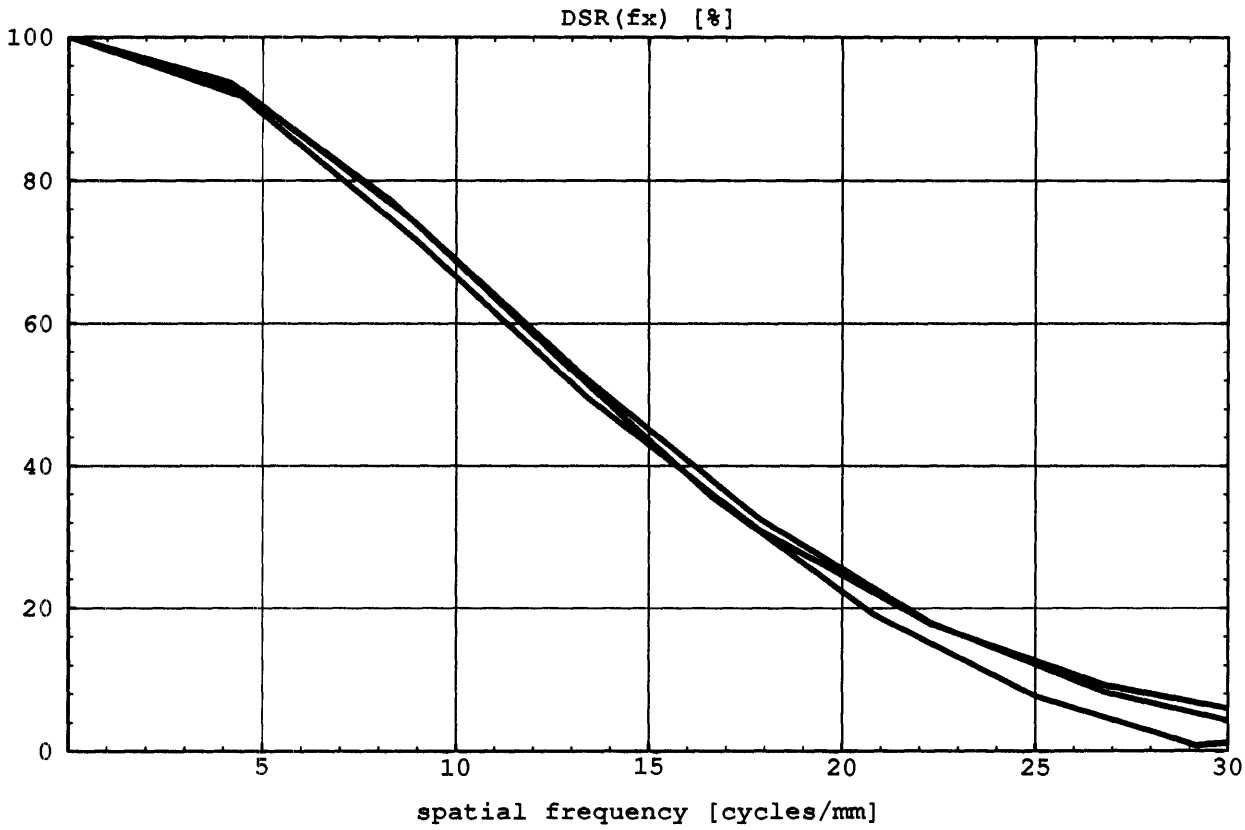

Figure 3-24: Small Staring Array simulation, 35 μm pitch, varying the pitch/mesa ratio. At 12 cycles/mm: Upper curve, Mesa of 25 μm; Middle, 35; Lower, 20. Discussed in text.

3.3.3 Discussion

While varying physical parameters varied MTF as expected, the results of the pitch/mesa tradeoffs were unexpected. The MTF does seem limited by the sinc function of the pitch, even when the mesa size is made smaller. An explanation might be that, although the diode junction size decreases, seemingly making the detector smaller and improving MTF, the smaller junctions allow the diffusion point spread function to be everywhere increased in size. The expected MTF gain due to smaller detector area is offset by increased lateral diffusion. The smaller mesa area does give lower quantum efficiency than the infinite area quantum efficiency with respect to the cell area.

The results achieved for the cases of equal mesa size and pitch may be compared to the Cheung model. With no trenches, the two problems are equivalent. The comparison is shown in Figures 3-25, 3-26, and 3-27. Unfortunately the results are not directly comparable in that Cheung's model as presently derived does not include a forcing field. The sinc function zeros are found to agree, however.

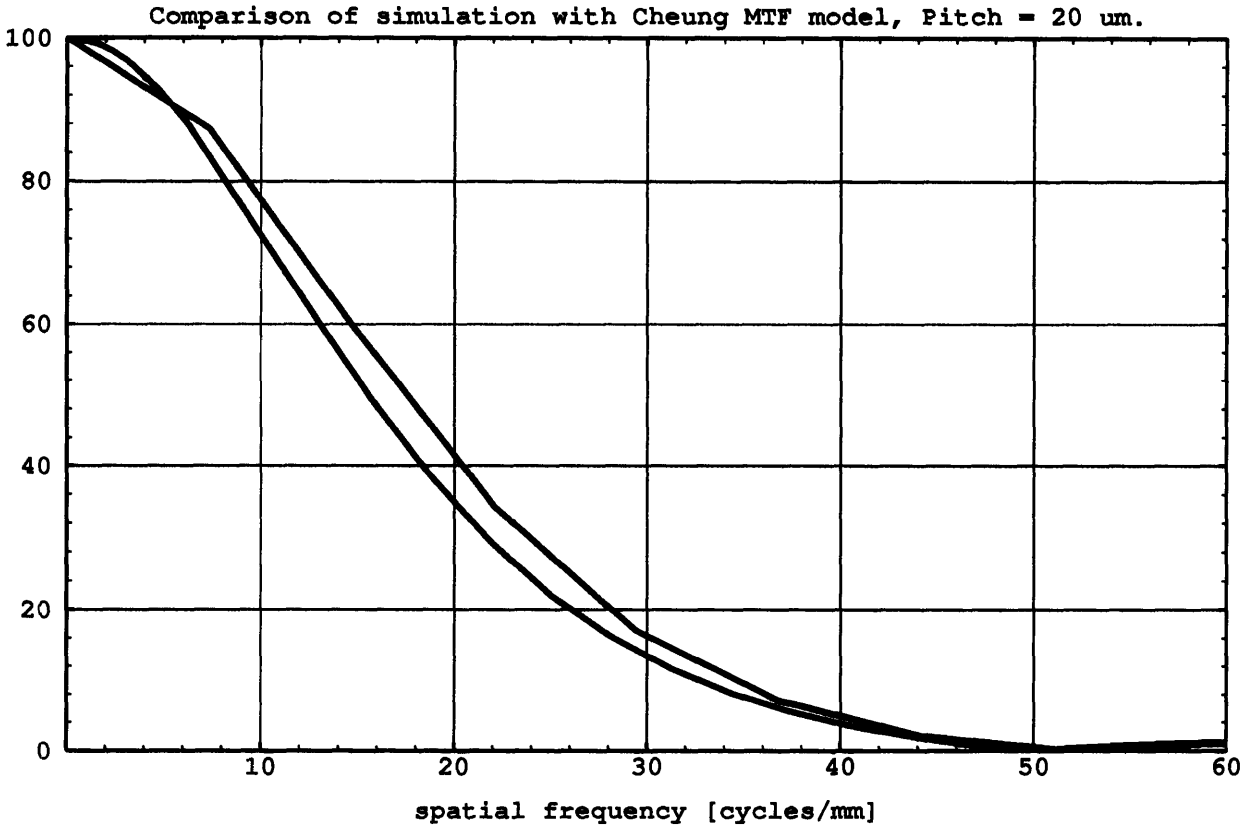

Figure 3-25: Small Staring Array simulation, 20 μm pitch. Upper curve, simulation, includes 8 V/cm drift field; Lower curve, Cheung model, without field. Simulation nearly matches the analytical case.

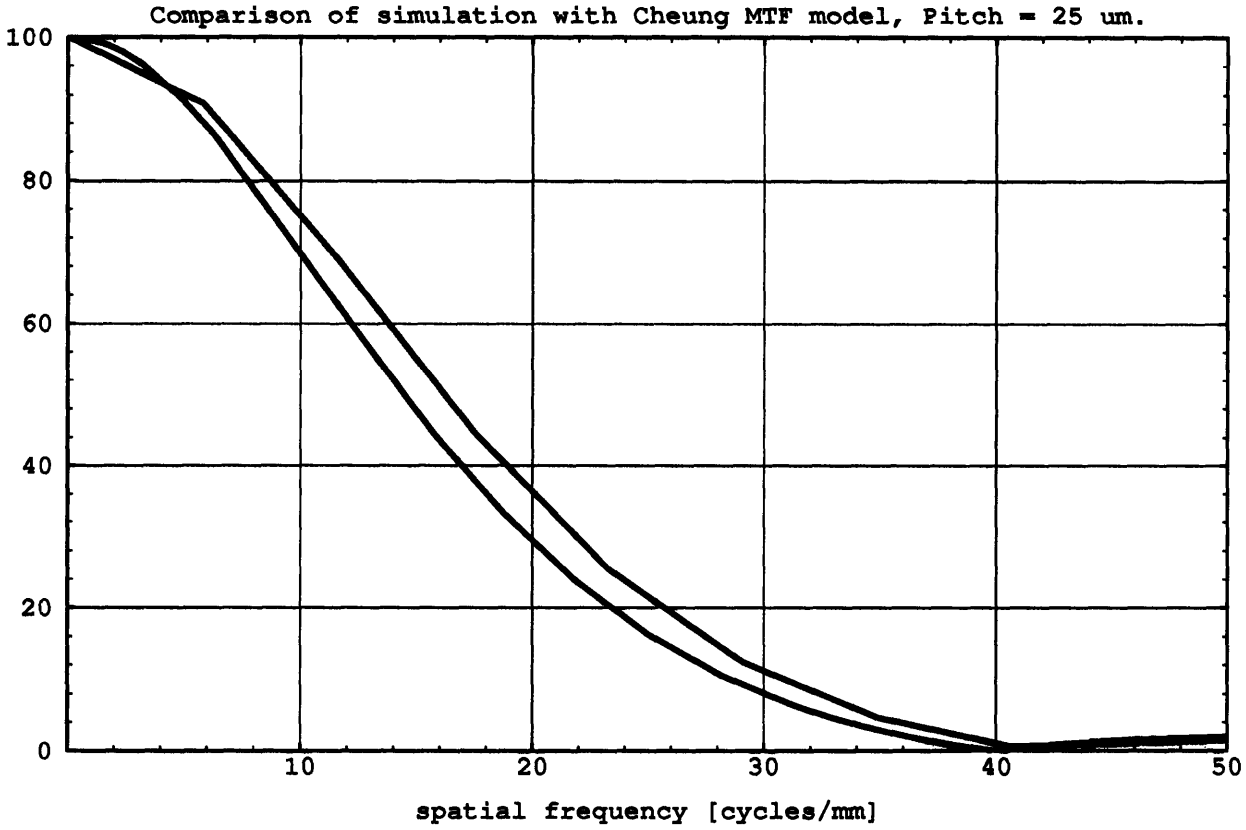

Figure 3-26: Small Staring Array simulation, 25 μm pitch. Upper curve, simulation, includes 8 V/cm drift field; Lower curve, Cheung model, without field. Simulation nearly matches the analytical case.

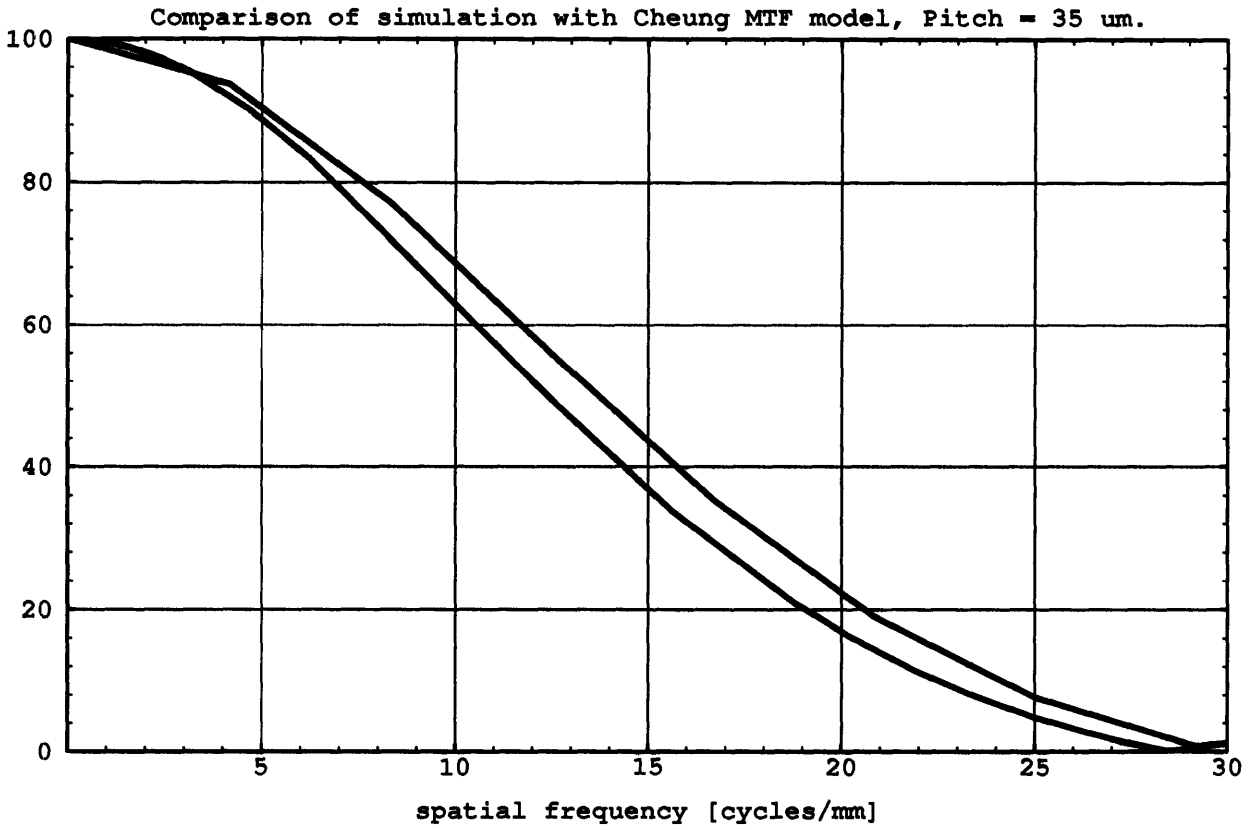

Figure 3-27: Small Staring Array simulation, 35 μm pitch. Upper curve, simulation, includes 8 V/cm drift field; Lower curve, Cheung model, without field. Simulation nearly matches the analytical case.

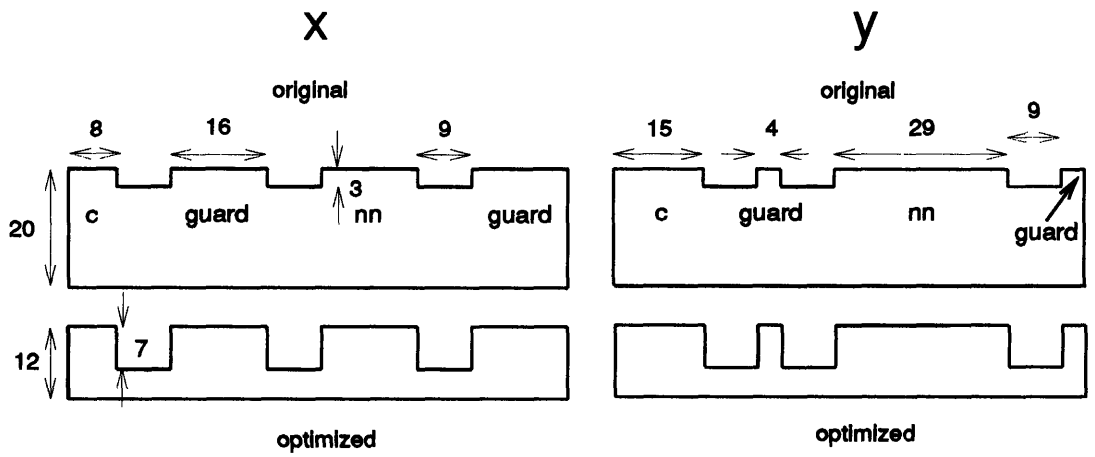

Figure 3-28: Cross sections of Small Scanning Array geometries, as input to the simulation, before and after optimization. Only half of the center diode (c) is shown in each view. Nearest neighbor is indicated by (nn). All dimensions in μm.

3.4 Optimization example

As an example of both a non–square scanning array and the use of this simulation as a design tool, the model was run on the array pictured in Figure 3-28, which is a crude approximation to the "small scanning array" geometry at LIRIS. While all lateral (x, y) dimensions remain the same, Table 3.1 shows the parameters used for both the present and the optimized Small Scanning Array FPA. Some parameters remain the same because they are fixed by other parts of the system. Decreasing the pitch was not possible since the array sampling frequency is fixed by system requirements. The absorption coefficient is typical of LWIR HgCdTe, and remains the same. Increasing s would unnecessarily cut flood illumination quantum efficiency and reduce the detector resistance. The pitch/mesa ratio was kept the same because of its small effects on MTF. The improved tightness of the response in direct–space and improvements in MTF are significant, providing useful targets for fabrication. The flood illumination quantum efficiency does decrease from 77.3% to 61.3%.

Figure 3-29 shows a simulated LWIR slit scan across the narrow dimension (x) of the photodiode. At the nearest neighbor distance of 50 μm, the response has been reduced by roughly two orders of magnitude. The corresponding improvement in x–direction profile MTF is shown in Figure 3-30. The analogous figures for the y direction are Figure 3-31 and 3-32. The detector is geometrically much wider in y than x. The optimized detector has a very uniform real–space response across this larger dimension, similar to a rect function. A response due to a infinitesimal spot, scanned along the x direction, is given in Figure 3-33. What is sometimes referred to as nearest neighbor crosstalk (i.e., the value on this graph at the center of the nearest neighbor) appears to fall roughly four orders

Parameter	Original	Optimized
α [/cm]	2000	2000
cut [μm]	3	7
d [μm]	20	12
E_z [V/cm]	8	24
kT/q [mV]	6	6
l_p [μm]	20	15
s [cm/s]	100	100
τ_p [μs]	1	1

Table 3.1: Small Scanning Array dif3d.c simulation parameters.

of magnitude. The improvement in the response for the y direction, shown in Figure 3-34, is not so substantial since the guarding is less extreme, but it is significant. Figure 3-35 presents the full two–dimensional detector response of the pixel before optimization. Figure 3-36 shows the result after optimization, with the detector becoming considerably more aperture–like. Figure 3-37 and Figure 3-38 show the two–dimensional MTFs corresponding to those two profiles. The two MTF figures are on the same scale. The width of the response in frequency space is markedly increased, and sinc function–like lobes become evident.

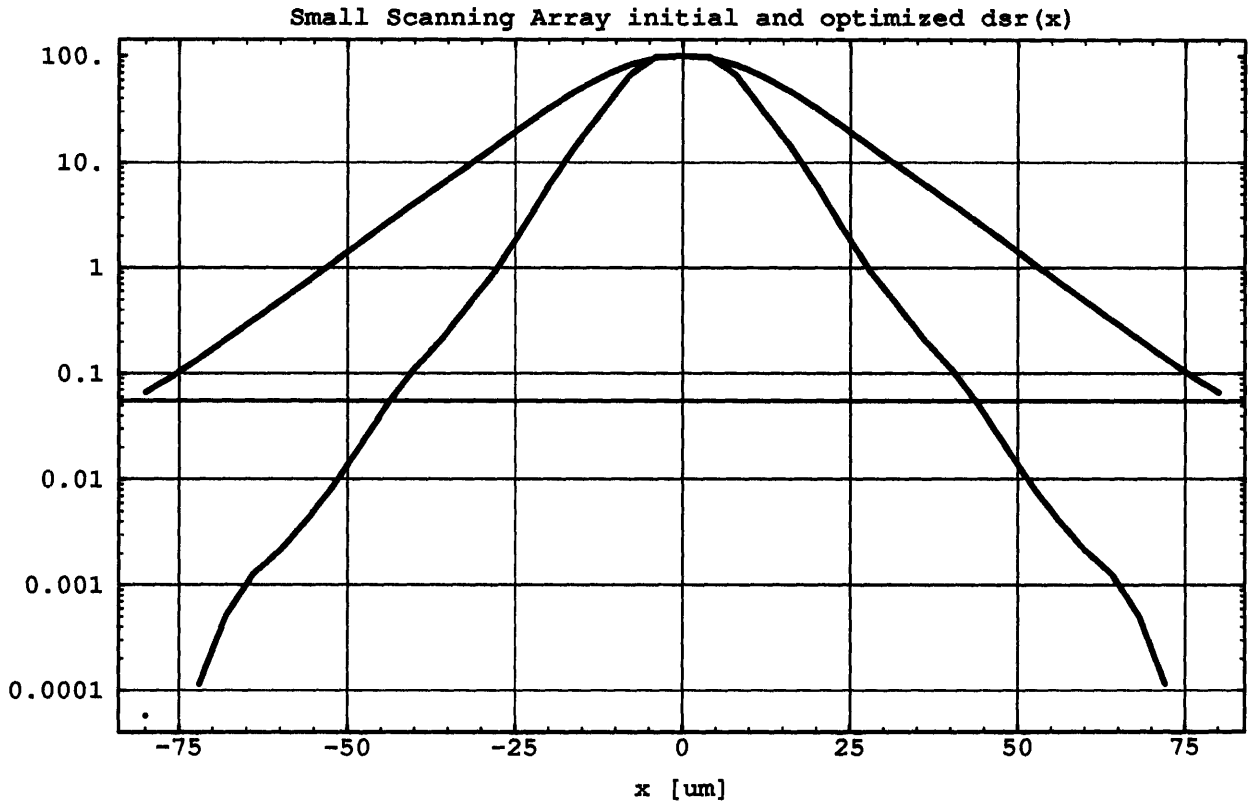

Figure 3-29: Small Scanning Array simulation, showing improvement of x direction slit response. Upper curve, original dsr(x); Lower curve, optimized dsr(x).

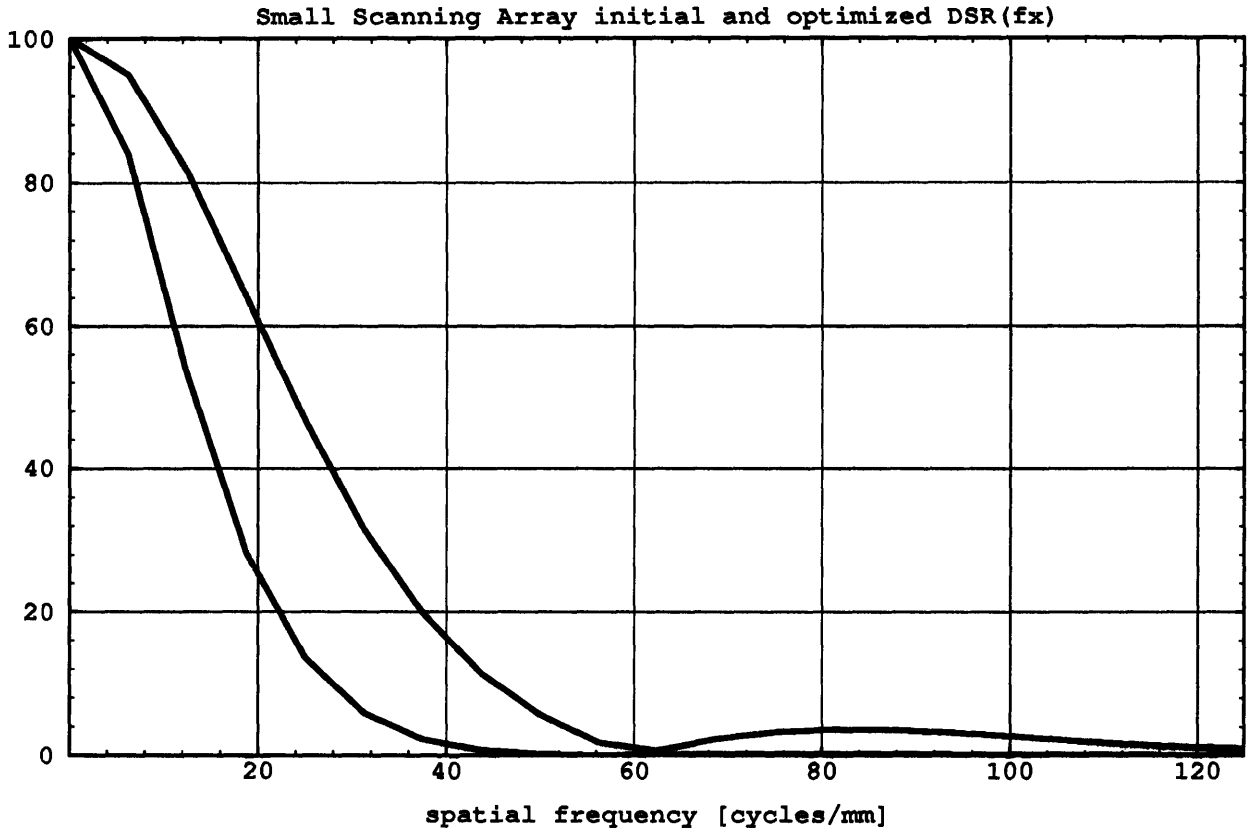

Figure 3-30: Small Scanning Array simulation, showing improvement of x direction profile MTF. Upper curve, optimized DSR(f_x); Lower curve, original DSR(f_x).

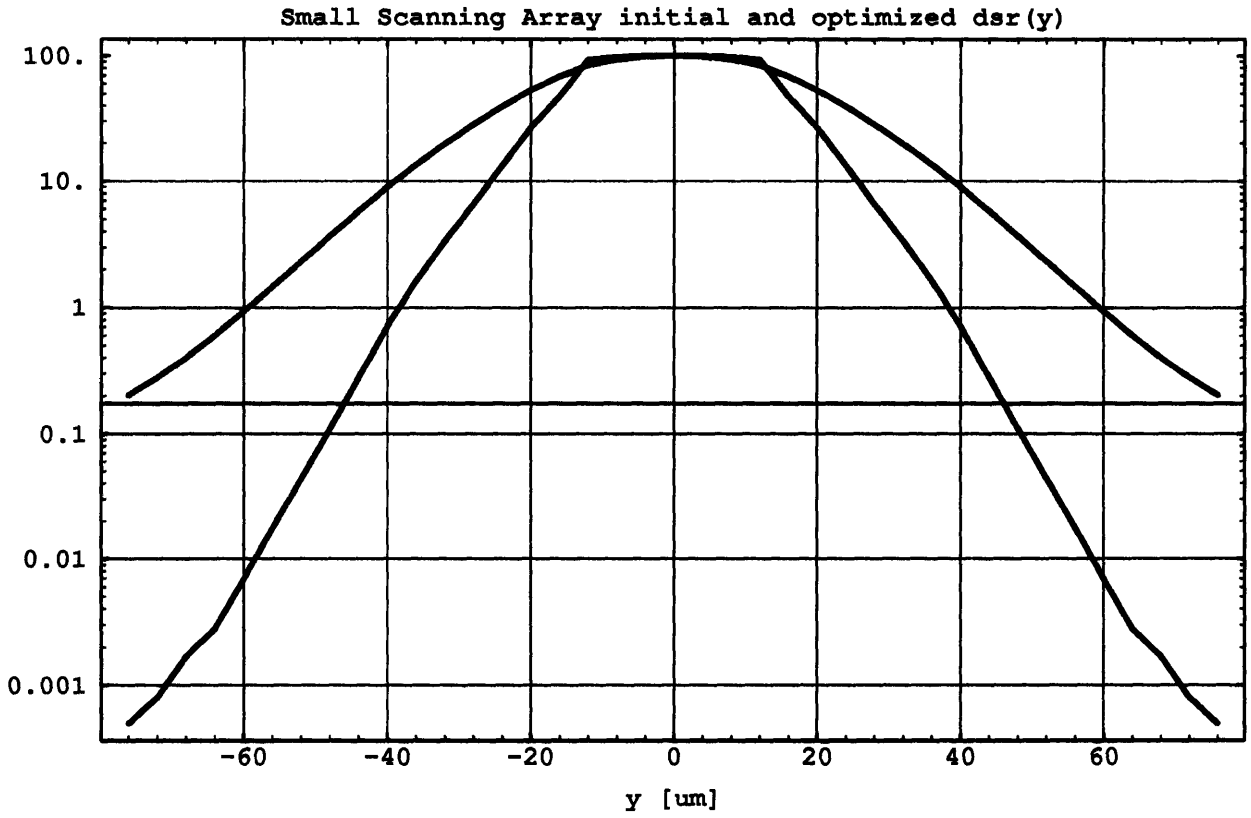

Figure 3-31: Small scanning array simulation, showing improvement of y direction slit response. Upper curve, original dsr(y); Lower curve, optimized dsr(y).

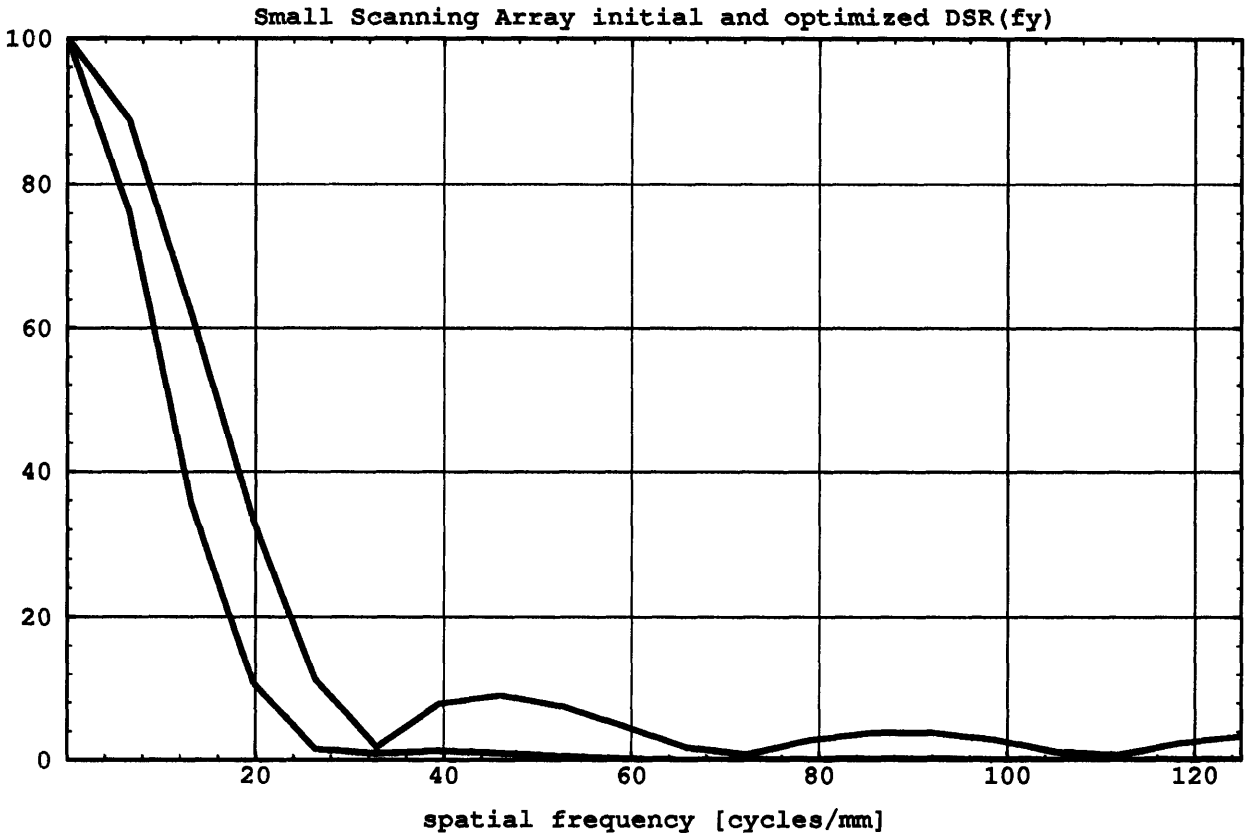

Figure 3-32: Small Scanning Array simulation, showing improvement of y direction MTF. Upper curve, optimized DSR(f_y); Lower curve, original DSR(f_y).

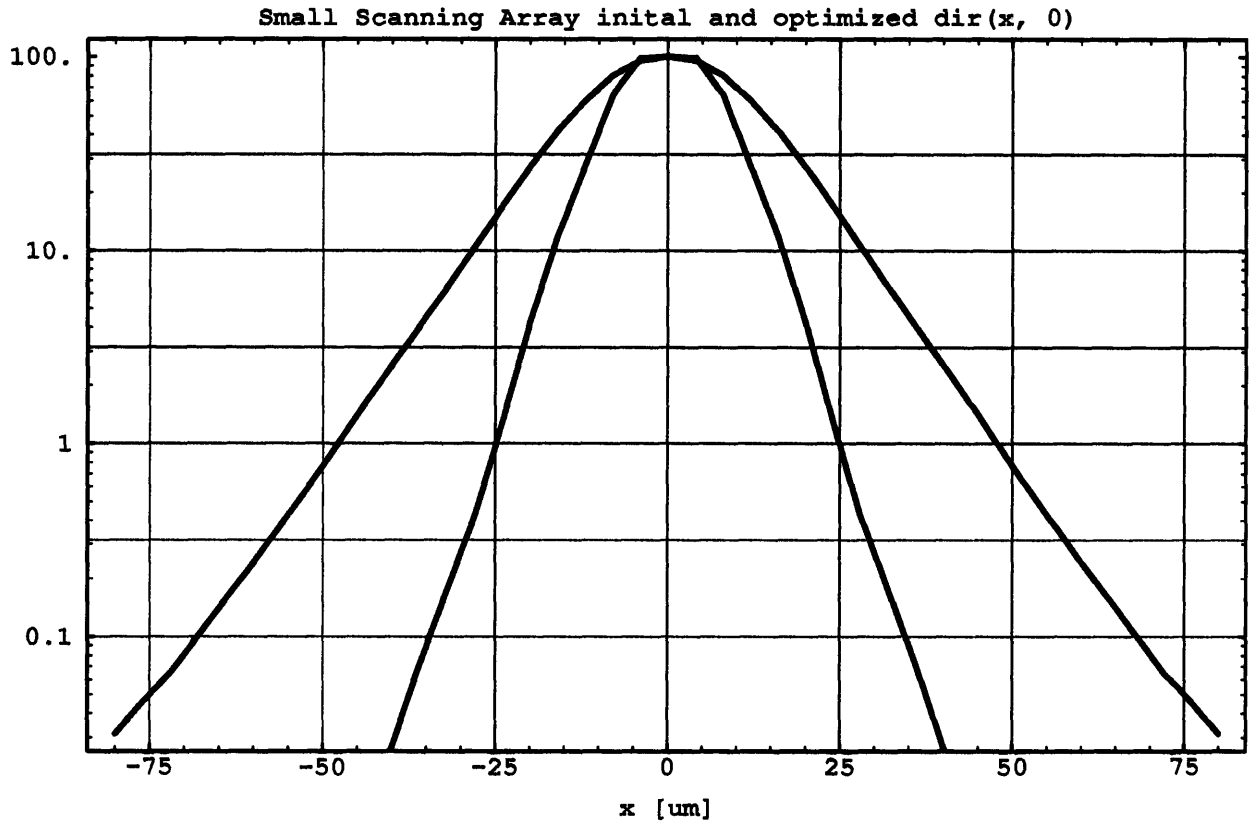

Figure 3-33: Small Scanning Array simulation, showing improvement of x direction spot scan response. Upper curve, original dir$(x, 0)$; Lower curve, optimized dir$(x, 0)$.

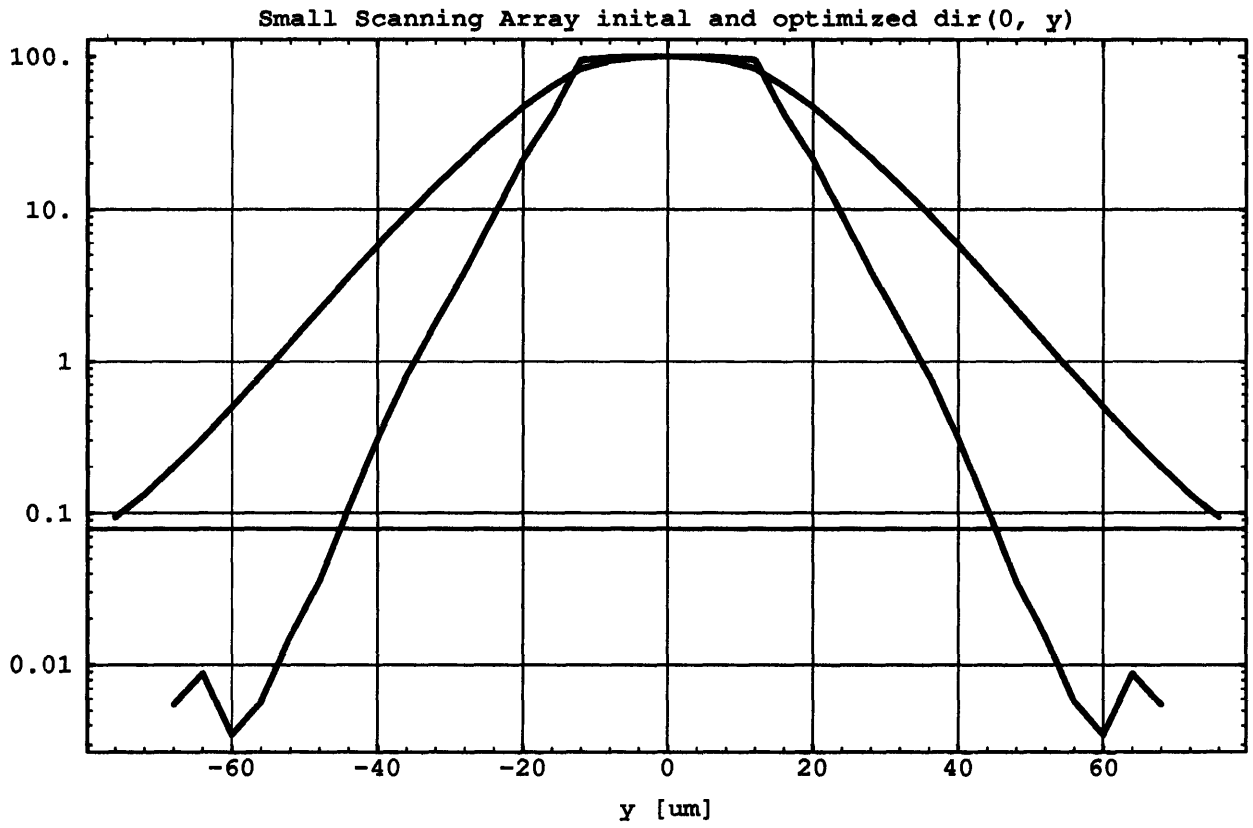

Figure 3-34: Small Scanning Array simulation, showing improvement in y direction spot scan response. Upper curve, original dir$(0, y)$; Lower curve, optimized dir$(0, y)$.

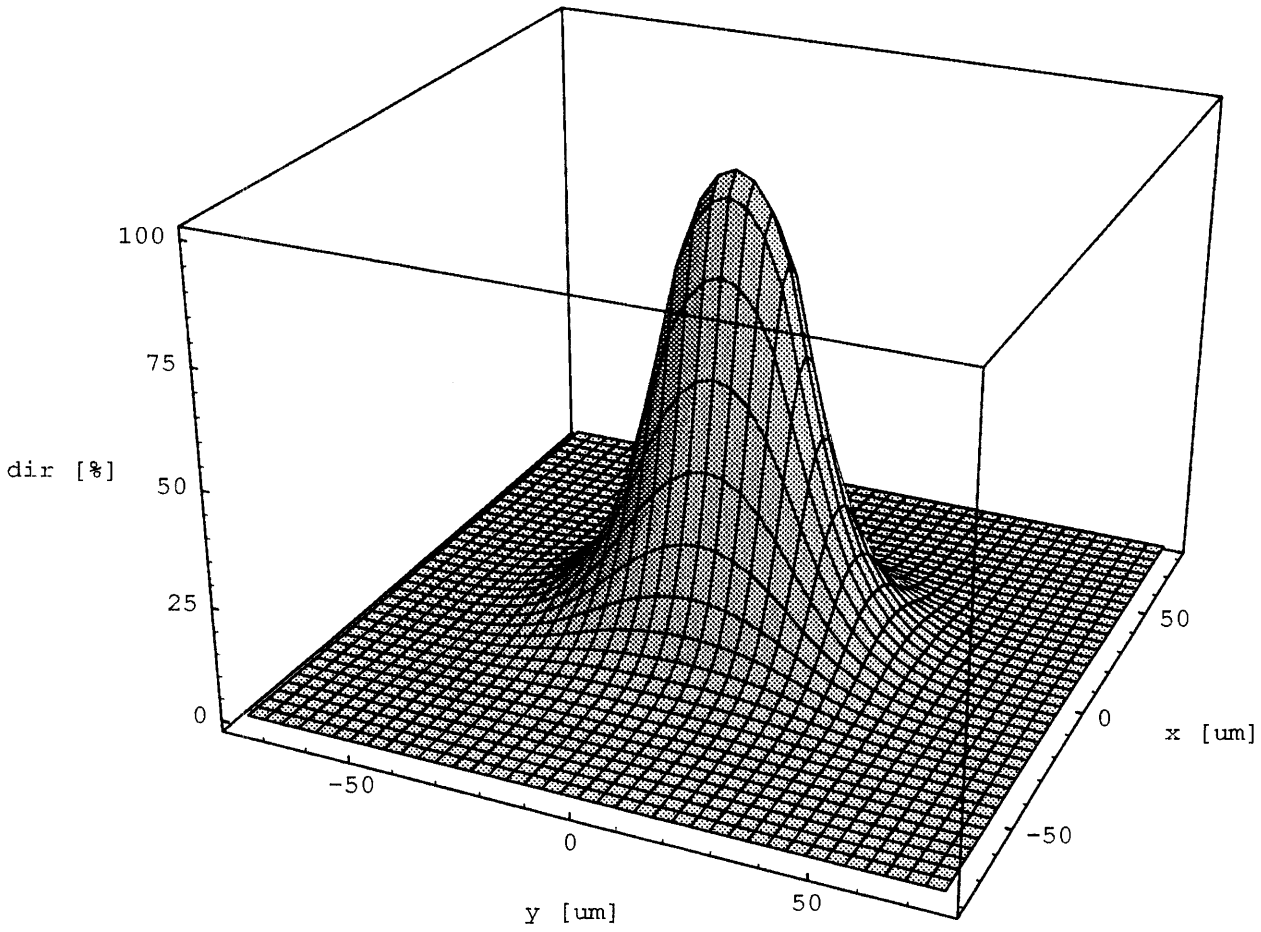

Figure 3-35: Small Scanning Array simulation showing original dir(x, y), or infinitesimal spot scan response.

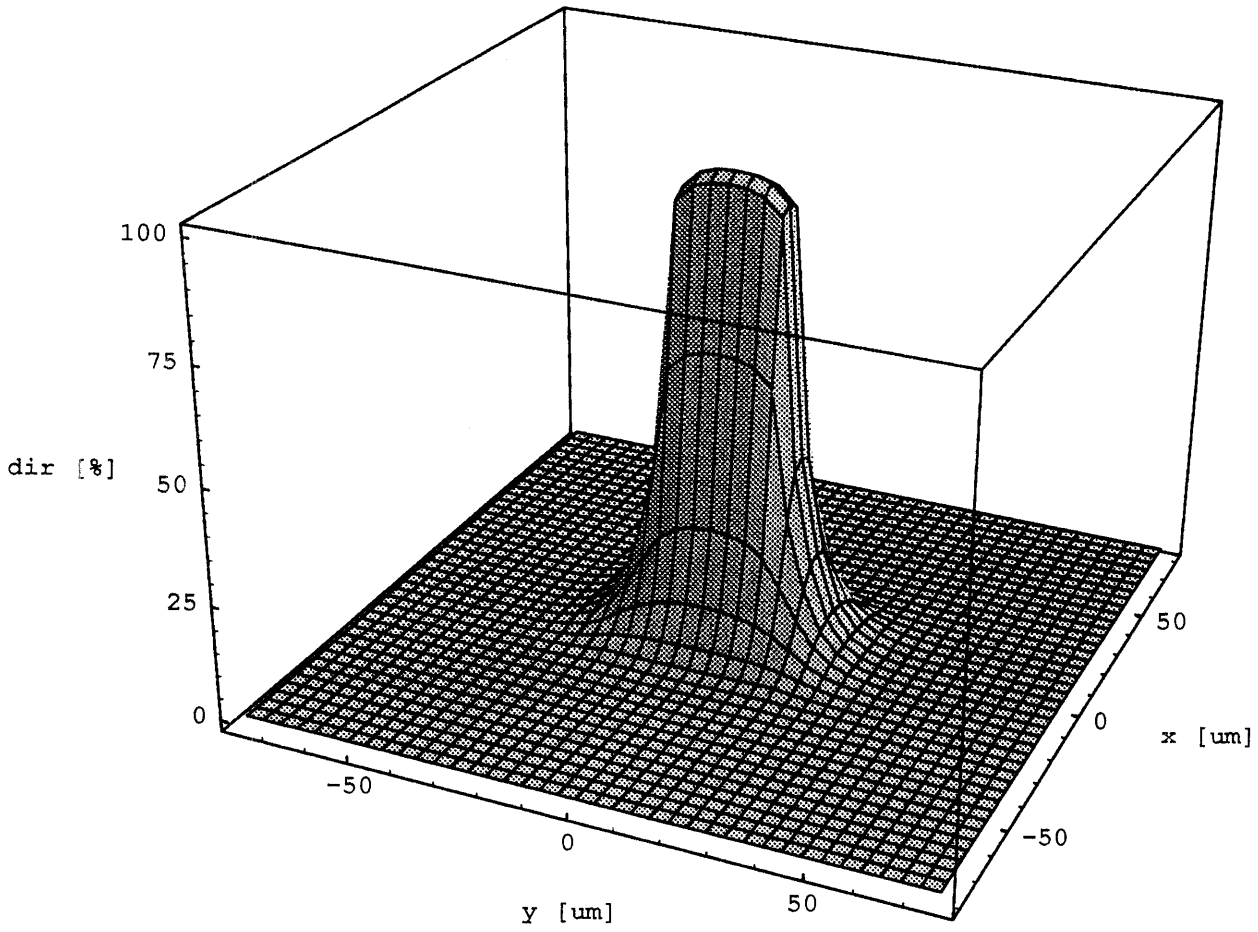

Figure 3-36: Small Scanning Array simulation, showing optimized $\mathrm{dir}(x, y)$.

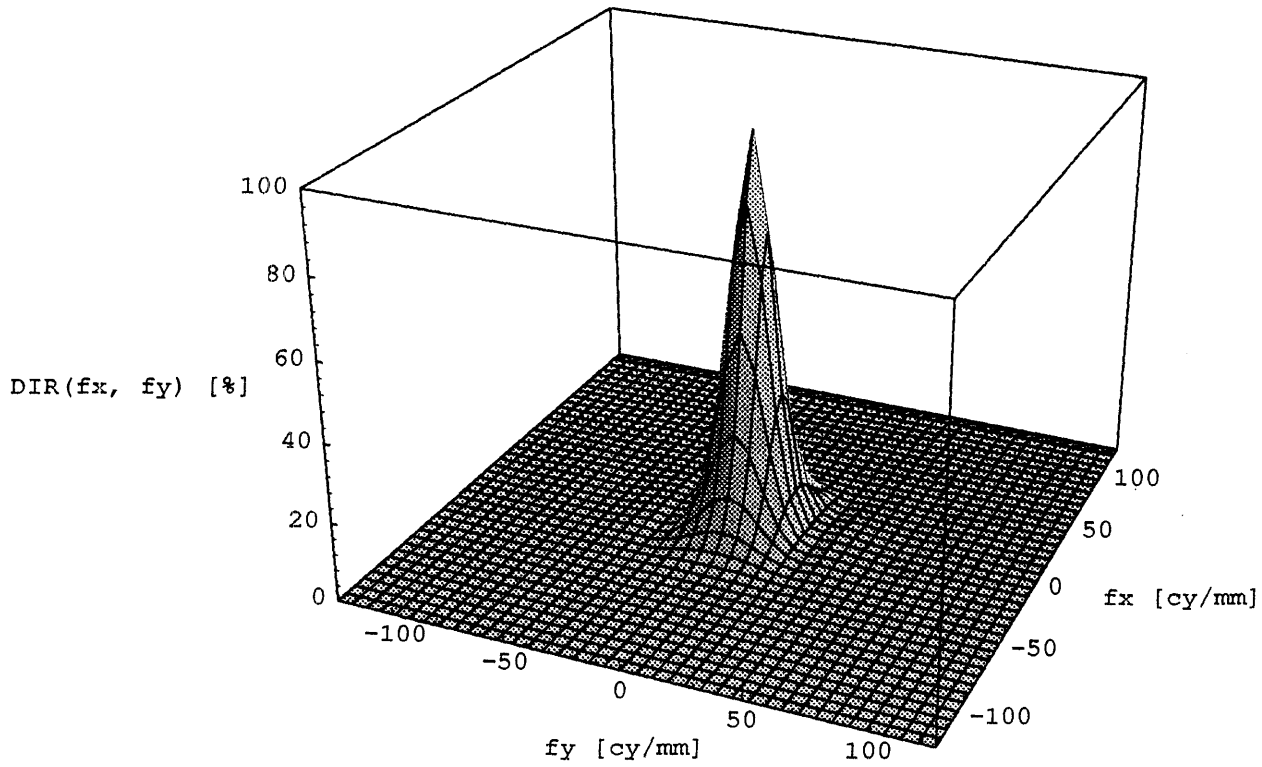

Figure 3-37: Small Scanning Array simulation, showing original DIR(f_x, f_y), or full two-dimensional diode MTF.

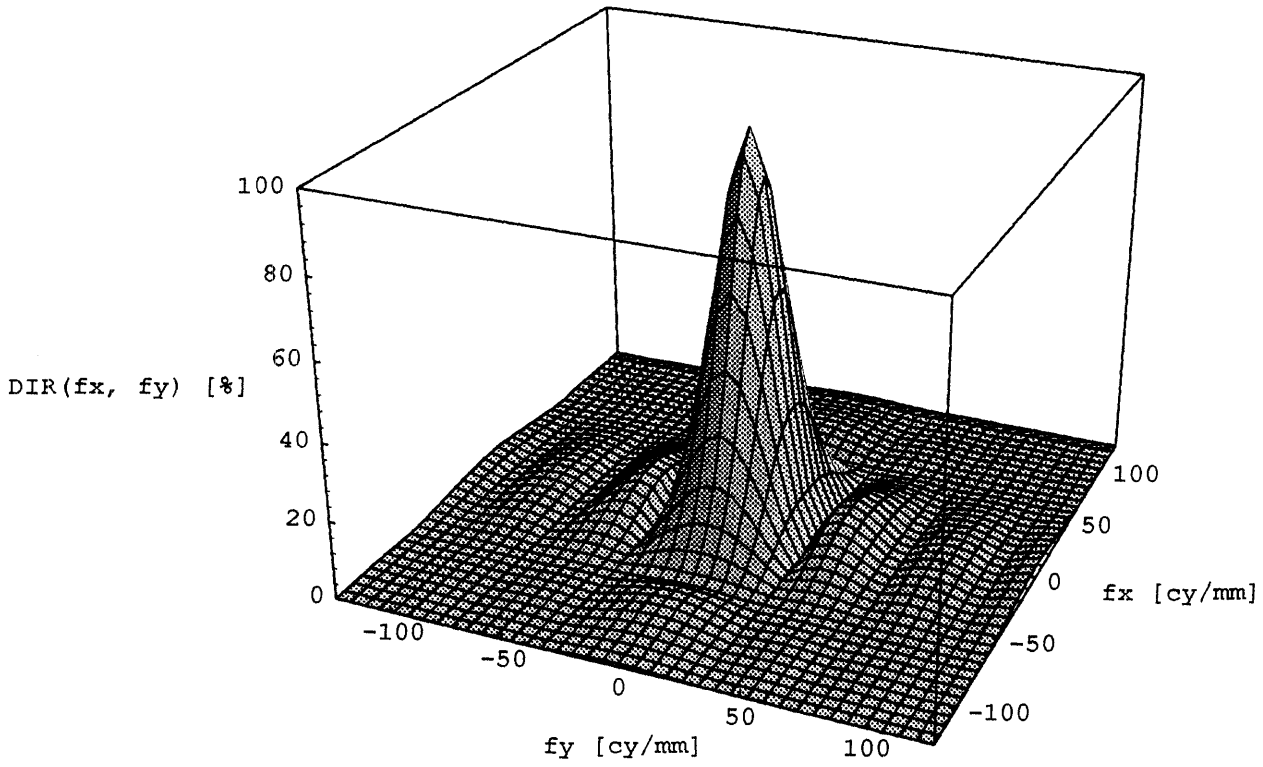

Figure 3-38: Small Scanning Array simulation, showing optimized DIR(f_x, f_y), or new full two-dimensional MTF.

Chapter 4

Characterization Theory

4.1 The test as an LSI system

Consider an illumination input, a spot intensity, $\mathrm{si}(x, y)$, which may be represented as the sum of weighted, shifted impulses. The response to such an input is just

$$\mathrm{ssr}(x, y) = \mathrm{dir}(x, y) * \mathrm{si}(x, y) \tag{4.1}$$

where $\mathrm{ssr}(x, y)$ is the spot scan response of the diode, and the $*$ denotes convolution. This result provides the means for measuring the MTF of detectors. As long as there is confidence in the measured data, $\mathrm{ssr}(x, y)$, and as long as the input form, $\mathrm{si}(x, y)$, is well characterized, detector MTF may be obtained by

$$\mathrm{DIR}(f_x, f_y) = \frac{\mathrm{SSR}(f_x, f_y)}{\mathrm{SI}(f_x, f_y)} \tag{4.2}$$

By these means a two–dimensional scan might be taken on some diode and the result back–transformed to yield $\mathrm{dir}(x, y)$. If an appropriate one–dimensional scan were taken in, for example, the y direction, the results may be used to yield $\mathrm{DSR}(f_y)$ and $\mathrm{dsr}(y)$, as were simulated in Chapter 3.

4.2 Test geometry

To be more specific, consider the schematic of the blackbody spot scanner at LIRIS, shown in Figure 4-1. In the scanner, blackbody radiation is chopped and may be filtered. The "Aperture" in the diagram is what will be reimaged onto the FPA. After a tube length of 300 mm, the radiation enters a NA 0.28 Schwarzschild reflecting objective, with 17.5% central obscuration. The objective has been corrected for the 300 mm finite conjugate and for a 1 mm thick ZnSe cover glass. The

Schematic of blackbody spot scanner optical elements; typical PV FPA target. Not to scale.

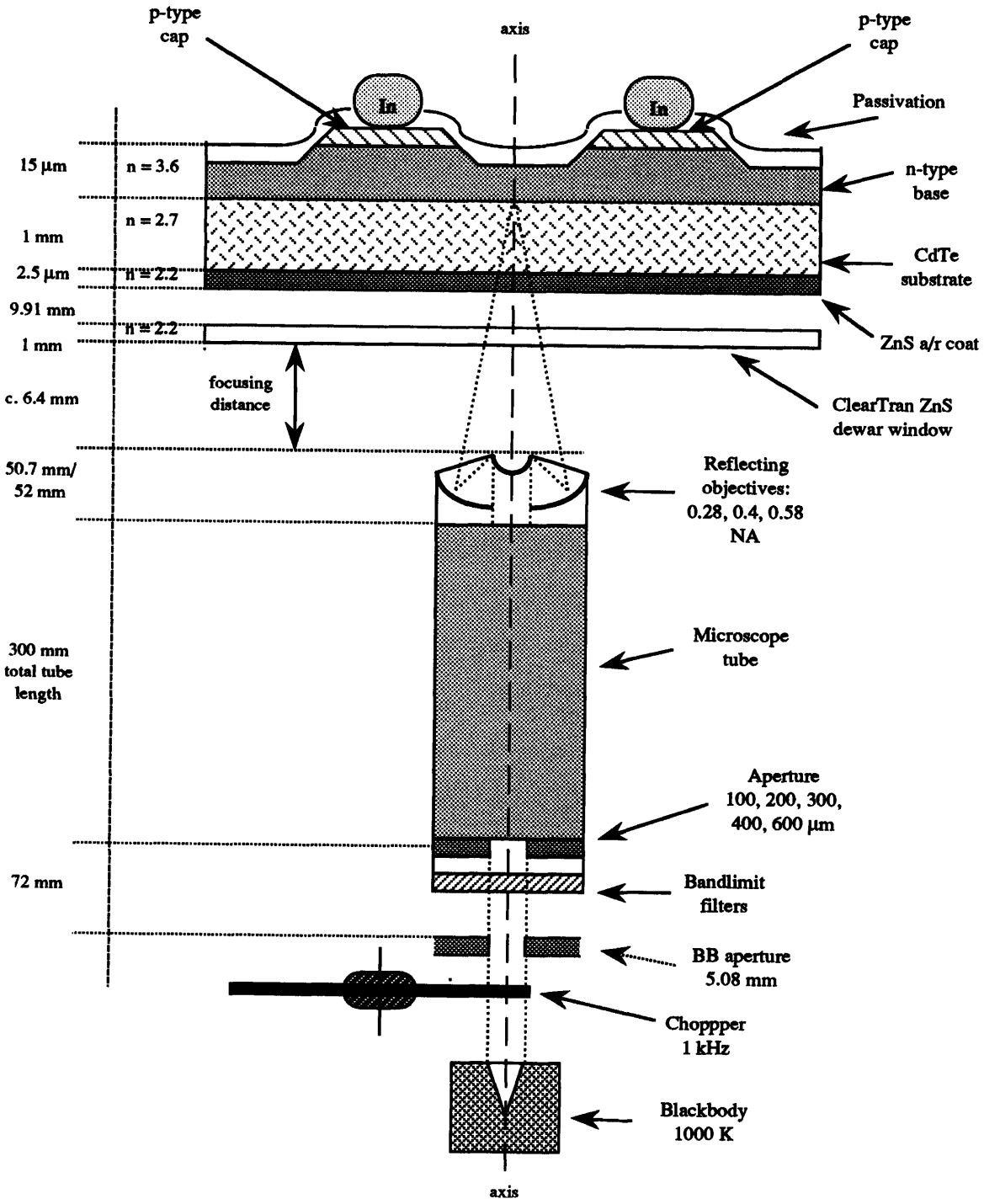

Figure 4-1: Spot/Slit scanner optical schematic, indicating all major optical elements of the scanner.

demagnification of the objective, used in this way, is approximately 27x. The image then passes through a ZnS window, of slightly different index than that for which the objective was corrected (ZnSe) and into an evacuated, cryogenic dewar. The FPA is mounted inside the dewar. The array has a 2.5 μm ZnS antireflection coat. The image then needs to pass through about 1 mm of CdTe, the IR–transparent substrate, until it finally reaches the absorbing n–type base layer. The detector photocurrent at zero bias is measured via a lead–out board, dewar wiring and connectors, a switchbox and then a transimpedance amplifier. The TIA output voltage is then amplified by a lock–in amplifier tuned to the chopping frequency, and read by a voltmeter connected to the station–controlling computer.

If the optics are diffraction–limited, and if the geometric input (the blackbody aperture) is a long slit, the slit scan response may be found by

$$\mathrm{ssr}(x,y) = \int_{y'=-\infty}^{y'=+\infty} dy' \int_{x'=-\infty}^{x'=+\infty} \mathrm{rect}(\frac{x'}{w})\mathrm{si}(x-x',y')\mathrm{dir}(x-x',y')dx' \tag{4.3}$$

This is not a function of y, however, since all information in that dimension is integrated out. Recalling Equation 3.32, and taking the transform of Equation 4.3,

$$\mathrm{SSR}(f_x,0) = \mathrm{sinc}(\pi w f_x)\mathrm{SI}(f_x,0)\mathrm{DIR}(f_x,0) \tag{4.4}$$

the profile MTF, DIR(f_x, 0) is made available, assuming knowledge of SI(f_x, 0).

4.3 Optical input

The key piece of information is the form of the optical input. This has two parts: one due to the shape of the input, and one intrinsic to the optical system itself. The optical system is also LSI and so it has some point spread function from which images can be built up by convolution. In these tests, the input light was filtered by a long–pass filter ($\lambda > 7.5$ μm), and the blackbody temperature was 1000°K. The optical modeling program *Code V* was used to create polychromatic diffraction limited MTF curves for this system by weighting seven monochromatic MTFs throughout an 8–12 μm spectral region.[1] The weights were just the photon flux density per unit wavelength due to the blackbody. This approximately matches the cut–on (7.5 μm, from the filter) and the cut–off (approximately 11.5 μm, from detector spectral response) of the the illumination relevant to determining the spatial response. While these MTFs were a function of radial spatial frequency, the direct space integration in y means that just the profile is being taken in frequency space, and f_r and f_x may be equated directly. Slit apertures with reimaged widths in the focal plane of 10 μm

[1] Courtesy R. Hassler, LIRIS optical design engineer.

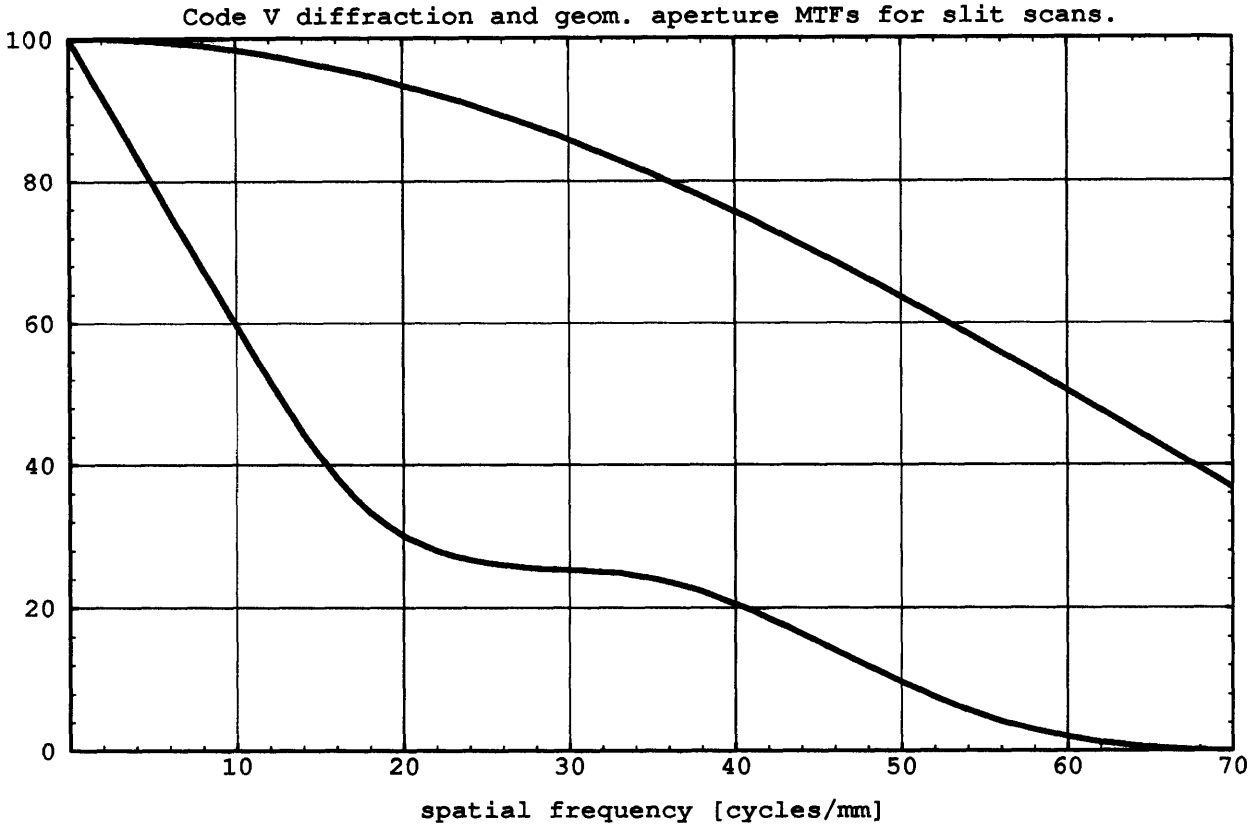

Figure 4-2: Code V polychromatic diffraction MTF for the optical system, and geometric aperture MTF of the 10 μm slit. The diffraction MTF is physically cut off beyond 70 cycles/mm.

and 20 μm were also used, whose transforms are simply given by the relevant sinc functions, as in Equation 4.4. In practice, these slits have a finite reimaged length of roughly 630 μm. This extends over at least 4.5 pixel neighbors in either direction for all pixel sizes of interest (pitches less than or equal to 60 μm). These are the input forms one needs to divide out to determine the response of the diode to a infinitesimal slit, which cannot exist physically due to diffraction. The MTF of the optics and the slit are shown in Figure 4-2. The diffraction limited MTF has spatial frequency content only out to

$$f_{\text{cutoff}} = \frac{2 \text{ N.A.}}{\lambda} \tag{4.5}$$

where the numerical aperture is 0.28 for this system, and λ is the shortest wavelength of electromagnetic radiation passed by the system [10]. Thus the input form in the *Code V* modeling has no content beyond 70 cycles/mm. Hence the output form also cannot have content beyond this frequency.

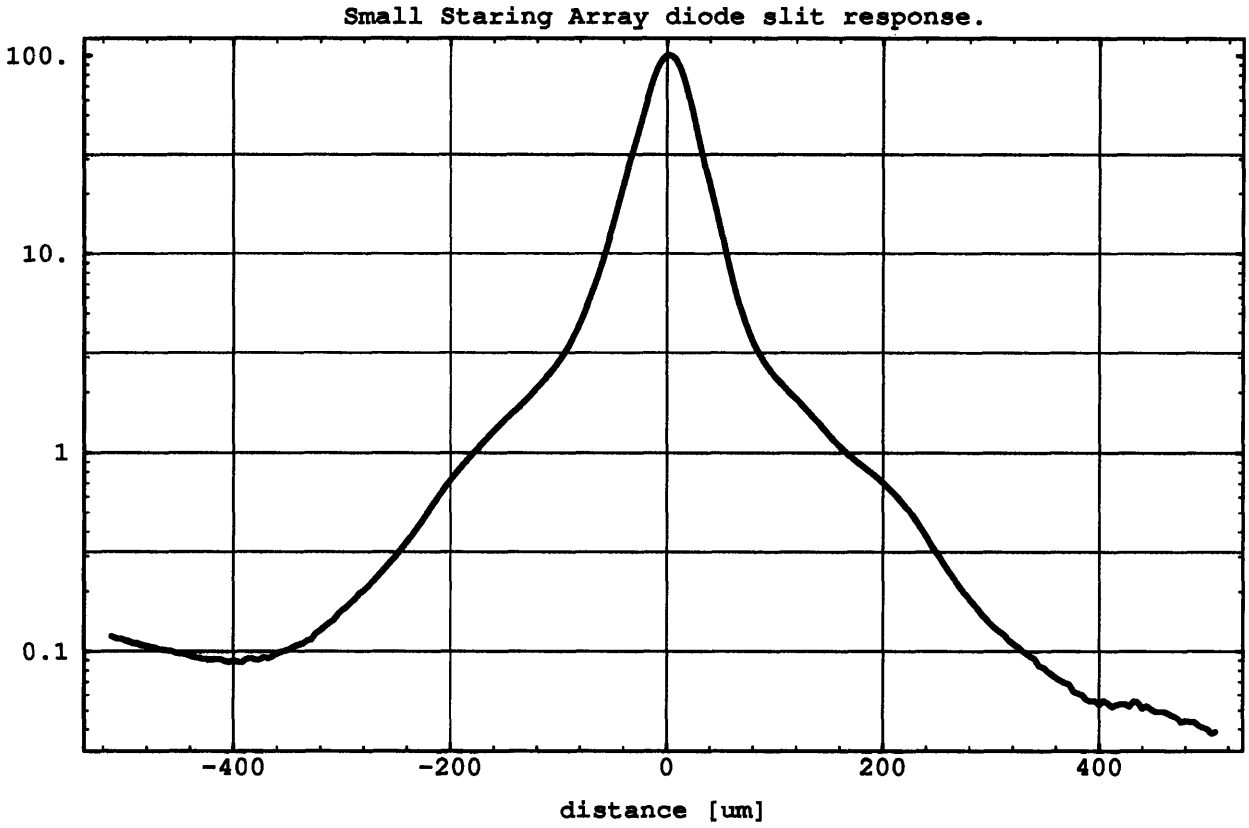

Figure 4-3: Small Staring Array diode slit response data.

4.4 Example output

An example of a raw slit profile, taken on a Small Staring Array diode, is shown in Figure 4-3. This is the normalized, direct–space response to the chopped bandlimited slit. The 256 points were taken on 4 μm steps. Direct space slit or spot scan data is typically shown on a log–linear scale so that the levels of response at the centers of the nearest–neighbor and next–nearest–neighbor diodes can be easily seen. While this slit scan data appears free of random noise, spot scan data does exhibit a signal–to–noise ratio problem for low signal levels. The mechanisms by which scan data may be corrupted are considered in the next chapter.

Chapter 5

Application of the test model

In this chapter, sources of error in the slit scan measurement are considered. Uncertainty in the optical input to the system is described and modeled. Uncertainty due to the data acquisition electronics is added to the output of the system. A less physical but equally problematic uncertainty is introduced by the choice of analysis — the use of the discrete Fourier transform (DFT). An attempt to quantify the total error is presented. The final section, optimizing the test procedure, discusses which test conditions were chosen in light of these signal–to–noise concerns. It is these issues, and testing time constraints which prevent taking two–dimensional "raster" spot scans since the lateral stepping uncertainty, the liquid nitrogen boil off, and instrument drift all preclude a long scan.

5.1 Uncertainty (Signal–to–noise ratios)

5.1.1 The optical input

Three problems are considered: lack of control in the z direction, resulting in defocused scans; lack of control in the lateral directions x and y, resulting in positional uncertainty; and the possibility of high level injection (HLI) affecting the minority carrier lifetime and causing a non–linear response.

Defocus

The *Code V* MTF modeling program was run for the defocus cases of 0, 25, and 50 μm. The results are shown in Figure 5-1. The defocus degrades the MTF and would cause the response to be wider than at proper focus. The focus adjustment knob on the z–stage of the spot scanner optics is marked off in divisions of 4 μm steps. Experimentally it was found that the backlash in this staging was approximately 24 μm. This is likely to be large compared to any defocus which is caused by the differential expansion of dewar parts as nitrogen boils off during the course of a normal scan.

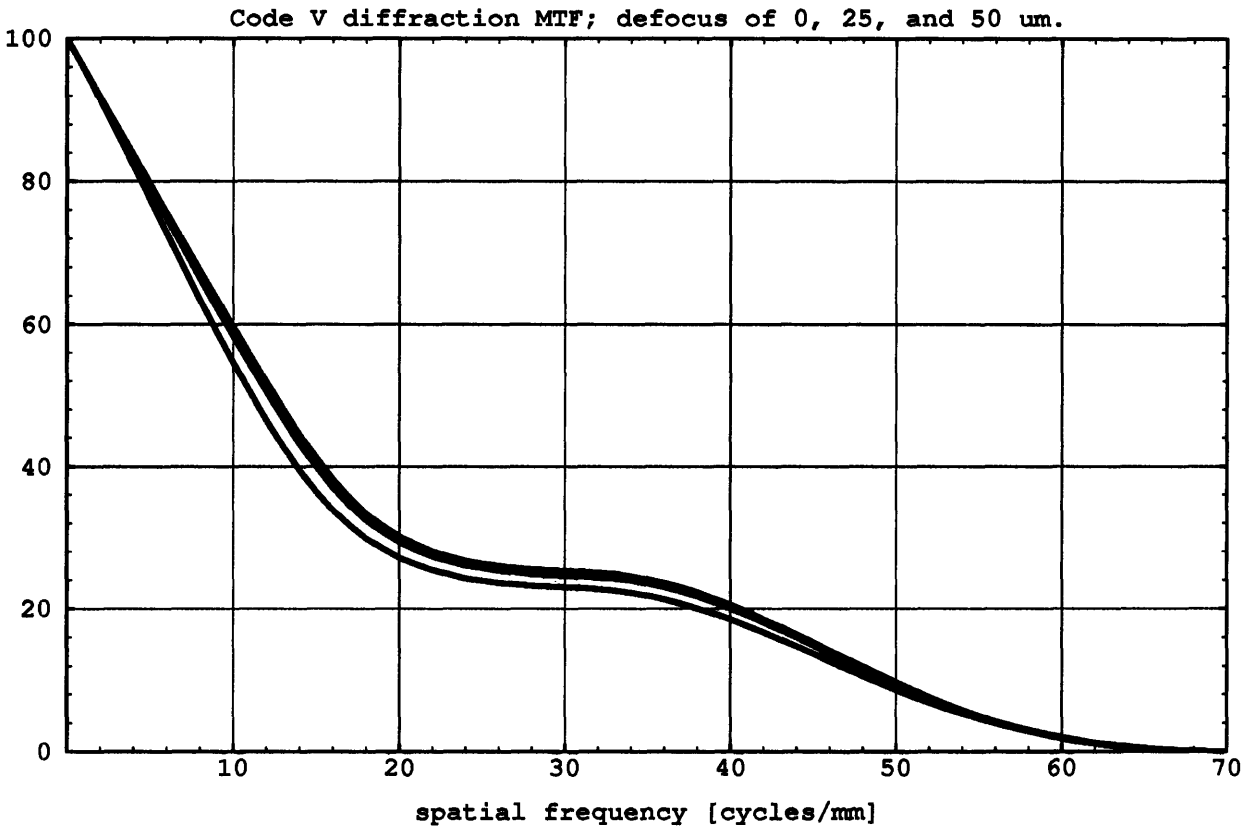

Figure 5-1: *Code V* polychromatic diffraction MTFs for the optical system. Upper curve, at focus; middle curve, defocused 25 μm; lower curve, defocused 50 μm. The quality of MTF decreases with defocus.

Typically then, the station operator should be able to work within that range ($\pm$ 24 μm). The spot or slit is focused by centering the input on the detector under test (DUT), adjusting the focus until the signal is peaked, and then centering and peaking again until no improvement can be made. The figure indicates that under these LWIR conditions, the depth of focus is adequate enough so that the MTF is not degraded significantly. The *Code V* model was also run for cases involving short wavelength infrared (SWIR), specifically a 2–4 μm band and an "unfiltered" 2–12 μm band. The MTF degradation with defocus is more severe for optical inputs involving short wavelengths. For all cases, when the SI(f) is divided out, the at–focus model is used, and the quality of detector MTF is not overrepresented.

Lateral Uncertainty

The translation of the spot is made possible by two computer–controlled stepper motors which move the x and y translation stages, upon which the dewar rests. When the software directs these motors, there is presently no way to verify how far they have moved. Typically, the motors are moved in either 2 μm or 4 μm steps. As described above, the signal is peaked and centered on the detector by iteration. The center of a detector, then, can only be found to a certainty of $\pm$ 2 μm. Furthermore, it is known that the scanner can lose steps when directed to make a large ($>$ 100 μm) motion, and end up a small, but variable number of steps away.

A way to model this is to take an approach similar to [7], and assume that the location of the input is uncertain everywhere by a standard deviation amount of $\sigma = 2$ μm. This problem can then be expressed as a line–of–sight (LOS) jitter problem [6] with

$$\mathrm{MTF_{LOS}} = \exp(-2(\pi\sigma f)^2) \tag{5.1}$$

This model is somewhat extreme in that the location is not everywhere uncertain to $\pm\sigma$, but it does provide a limiting case. Figure 5-2 shows this potential degradation in MTF for the cases of $\sigma = 2$ μm (lower) and $\sigma = 0.5$ μm (upper). The 0.5 μm case could be achieved by adding encoders of that resolution to the staging, and allowing them to feed back to the software. Most MTF concerns apply to the frequency region below 20 cycles/mm, but future systems may be interested in the MTF at even 60 cycles/mm.

Rotational uncertainty occurs when the slit is not perpendicular to the scan direction. This possibility was not quantitatively examined in this research, but its minimization was of interest (see Section 5.2).

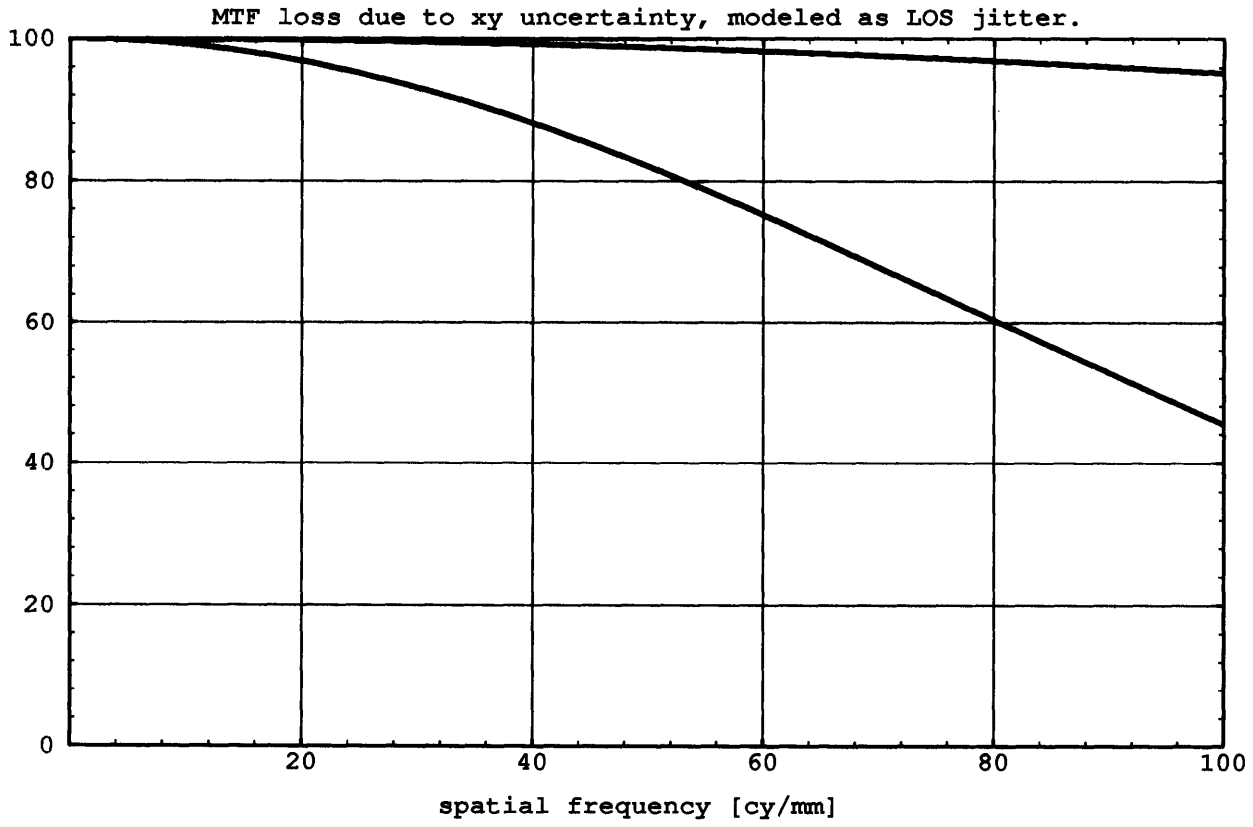

Figure 5-2: Line of sight jitter MTFs, modeling lateral uncertainty. Upper curve, $\sigma = 0.5$ μm; lower curve, $\sigma = 2$ μm. MTF decreases with increasing jitter.

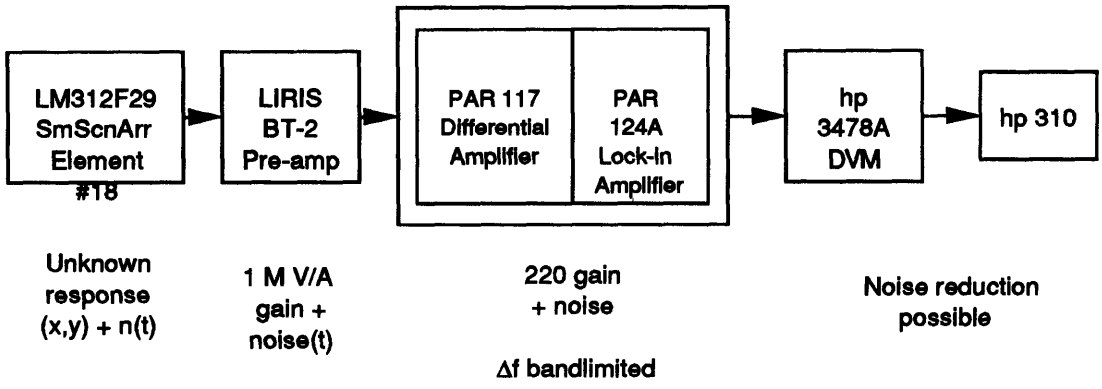

Figure 5-3: Spot scan signal acquisition path. Each component potentially introduces or suppresses noise.

Nonlinearity

LIRIS n–type base layers are doped to a concentration of 10^{15} cm^{-3} and are limited by an Auger hole lifetime. HLI is a concern because the system would have a non–linear response. The uncold-shielded 300°K detector background flux, for a typical cutoff wavelength of 11 μm, was found to be approximately 6×10^{17} photons per cm^2 per second. As a quick estimate of photogenerated carrier density, $\alpha\tau_p\Phi_0$ is roughly 10^{15} cm^{-3}, of the same magnitude as the doping. Furthermore, the rms flux due to an unfiltered (2 – 11 μm) spot and a 1000°K blackbody was found to be quite high, roughly 2.2×10^{18} photons per cm^2 per second. This number was based on a purely geometrical optics throughput argument. Diffraction lowers this peak flux by some factor. Actions to mitigate this high flux level are discussed in Section 5.2.

5.1.2 The electronics at system output

A case study was performed to determine the noise levels for a particular element of a Small Scanning Array during a spot scan. The essence of that study is presented here. This detector was spot scanned without filtering or coldshielding. Figure 5-3 shows the path by which data is acquired. The uncorrelated random noise produced by the detector and the other electronics will in general provide a noise floor for the system. The main noise contributions to the detector photocurrent are the Johnson–Nyquist rms noise current and the rms shot noise on the background dc photocurrent. For a spatially small spot, the chopped photocurrent is much smaller than the background dc

photocurrent, so its shot noise is negligible. The transimpedance amplifier (TIA) also contributes voltage and current noise. The lock–in amplifier contributes negligible noise, but it does have a dynamic range of 10^5 when used in the low–drift mode, implying measurement is only possible down to 0.001% of the peak response. This minimum discernible voltage limits the measurement before discretization of the voltage in the digital voltmeter (DVM) does. However, the most important function of the lock–in amplifier with respect to noise level is that its bandpass and lowpass filters determine the noise equivalent band width (NEBW) of the measurement. Assuming no averaging or integration by the DVM, this NEBW is 1.25 Hz at the DVM input, when the chopping frequency is at 1000 Hz. While the DVM readings are too fast to further attenuate the noise, the software averages 25 readings when it is trying to read the weaker signals. This may have the effect of limiting the NEBW to 0.8 Hz. Assuming the NEBW of 1.25 Hz applies, and using numbers for a typical detector, the spot scan noise floors were found to be 0.0029% in direct space and 0.0024% in frequency space. While the noise floors mentioned above may effect the diode impulse response to some degree, the MTF is not greatly affected since one is concerned with the MTF in linear, not logarithmic terms. The shot noise on the dc background photocurrent and the TIA noise were identified as the dominant components of the random noise.

Discretization

The continuous signal of a slit scan response is sampled discretely on some number of points. The choices of sampling density and number of points are important to insure accurate deconvolved MTF data.

The sampling frequency is determined by aliasing considerations alone. Since the signals have no content beyond the optical cutoff frequency, then the sampling frequency need only be at least twice the cutoff. In general, one would also want the first zero of the geometric aperture sinc function to lie outside the lowpassed region. This avoids the problem of dividing by either zero or small numbers. The number of points, N, used depends on two things: how faithful a reconstruction of the original is desired and if N is required to be a power of two by a Fast Fourier Transform (FFT) algorithm, although the signal could be "padded" with zeros in order to meet that constraint. For convenience, a density of about one point per cycle/mm was desired. This implies $N = 256$ for $f_s = 1/(4\ \mu\text{m})$ and $N = 512$ for $f_s = 1/(2\ \mu\text{m})$, in order to take advantage of the speed of the FFT.

As an illustration of these issues, consider Figures 5-4 and 5-5. These show the exact MTF for a 36 μm wide rect function as well as that obtained by DFT when the rect function is represented discretely. When the data is sampled on 4 μm steps, the spectrum is replicated about the sampling frequency of 250 cycles/mm, so information is aliased back into the lower frequency region between 0 and the Nyquist frequency (125 cycles/mm). When the data is taken on 2 μm steps, as in Figure 5-5, the spectrum is replicated about 500 cycles/mm and causes less of a problem. Typical bandlimited

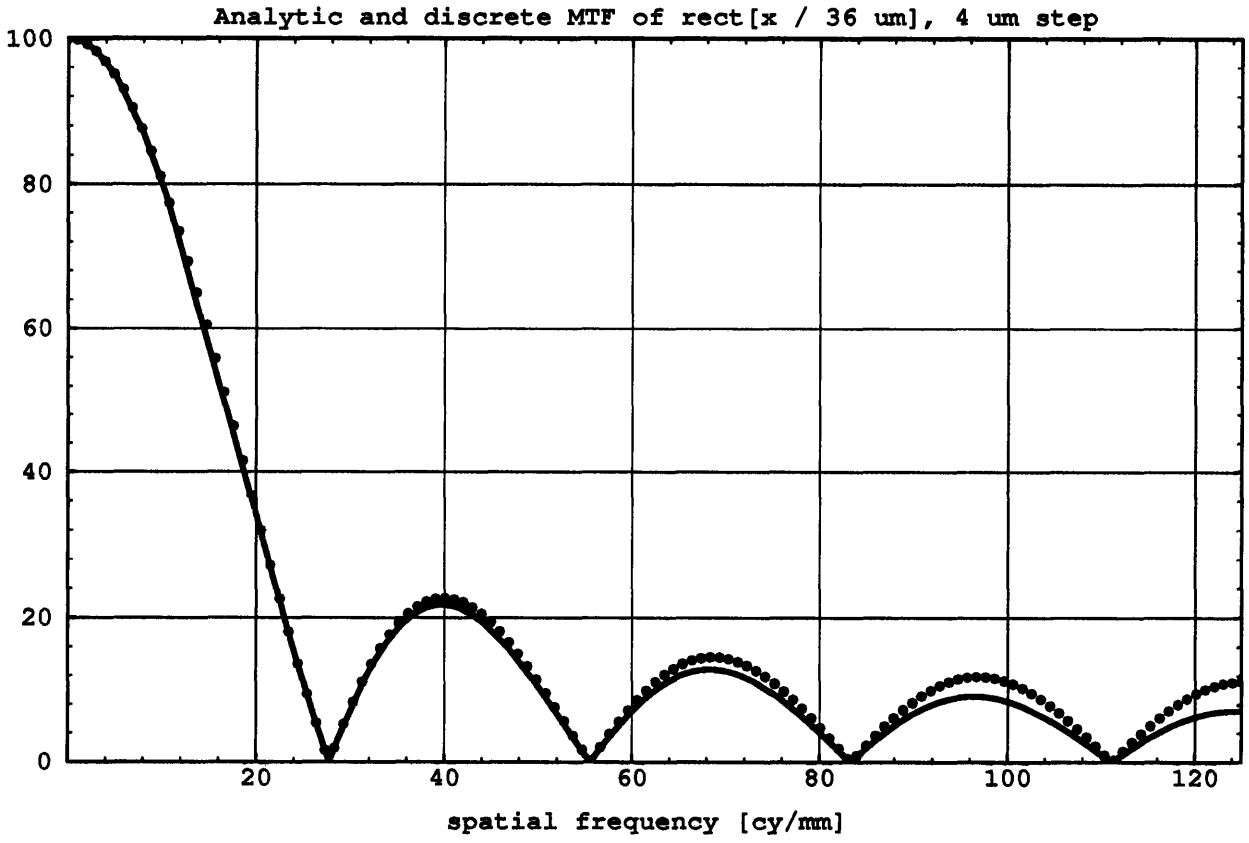

Figure 5-4: Analytic (solid line) and discrete (dotted line) Fourier transforms of a 36 μm wide rect function. The discrete data is on 4 μm steps, and becomes higher than the analytic transform due to aliasing.

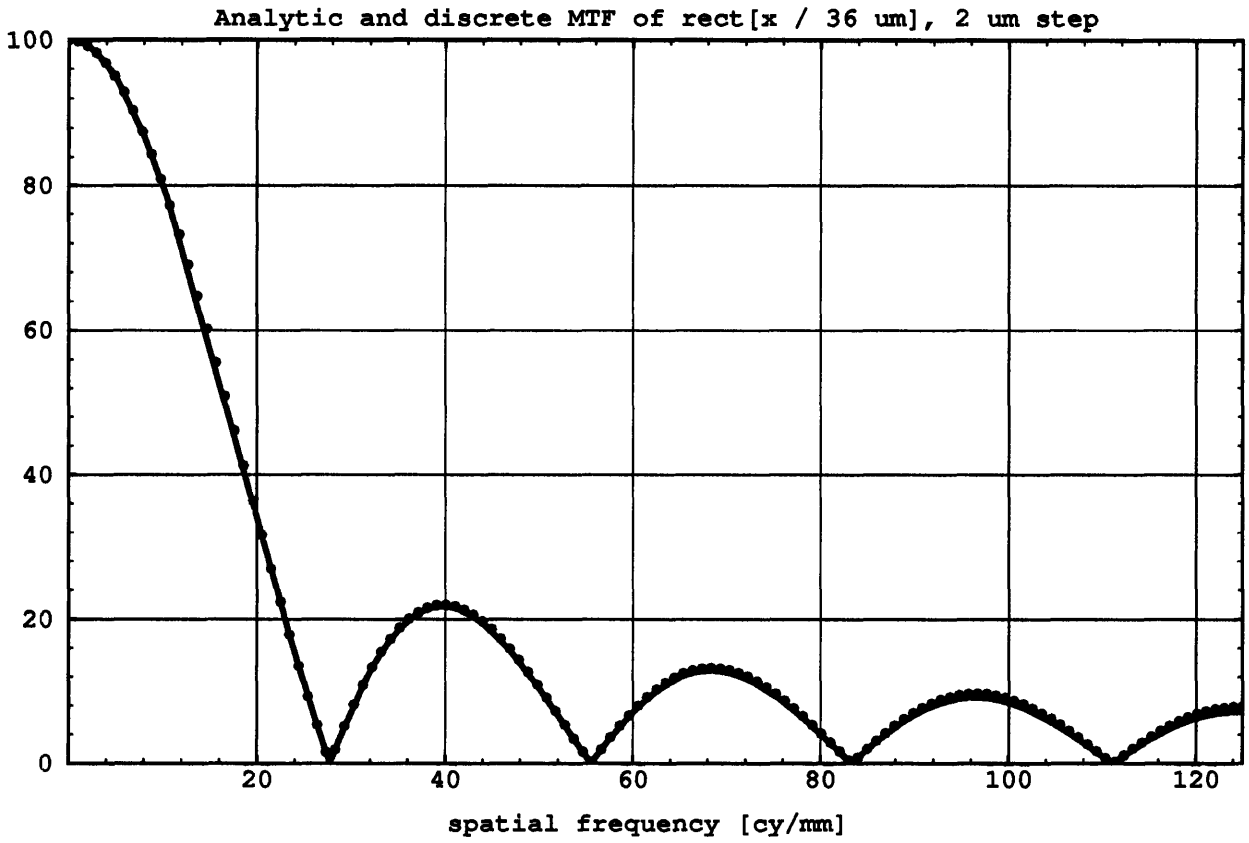

Figure 5-5: Analytic (solid line) and discrete (dotted line) Fourier transforms of a 36 μm wide rect function. The discrete data is on 2 μm steps, and becomes higher than the analytic transform due to aliasing.

signals will not be aliased, however.

Combined uncertainty

For a slit scan response, the chopped photocurrent has a much higher signal level than that of spot scans. This implies that the shot noise level is also higher. However, the signal–to–noise ratio for the collected slit photocurrent and its shot noise is just $\sqrt{I_{ph}}$, which improves with larger current. Therefore, shot noise on the chopped photocurrent is neglected for the case of slit scans. The magnitude of the other random noise contributions remain the same as in the spot scan case. Since the signal level from the slit scan is larger than that of a spot, the noise floors found above occur at even smaller percentages of the peak response.

Neglecting the random noise from the electronics, the dominant sources of uncertainty are from the optical input: lateral uncertainty and defocus. Considering the hypothetical 36 μm aperture again as a test case, the total uncertainty may be quantified as a function of spatial frequency. While the dc, flood illumination MTF is always unity, the MTF at all other spatial frequencies can contain errors. Figure 5-6 shows a sinc function bandlimited to 70 cycles/mm and the uncertain MTF of a discrete sinc function corrupted by jitter, defocus, and aliasing, and then divided by the MTF of the optics at focus. The reported MTF is lower due to the defocus and jitter.

Figure 5-7 shows the relative error in each point as a function of spatial frequency. The under-reporting of the MTF increases with frequency. In the region of current performance specifications, this error is roughly 5% or less.

More troubling is the backtransformed aperture function shown in Figure 5-8. The discrete, corrupted, ideally lowpass filtered MTF shown in Figure 5-6 was reverse transformed and displayed on a logarithmic scale with the ideal 36 μm aperture. While the response is symmetric as before, the "wings" of crosstalk on this ideal diode arise from the abrupt lowpass filtering and/or the corrupted MTF. This result puts a limit on using deconvolved slit scan data for extracting column–to–column or row–to–row crosstalk in the manner that spot scan crosstalk is defined. This issue will be revisited in Chapter 6.

5.2 Optimizing the test procedure

Given all the sources of uncertainty discussed above, the test procedure was designed to mitigate as many as possible. Since the time to acquire one scan in one direction is three to four minutes, a raster spot scan would not be practical due to the long test time, the lack of positional surety, and instrument drift. By using slit scans, however, the profile MTF is reliably yielded.

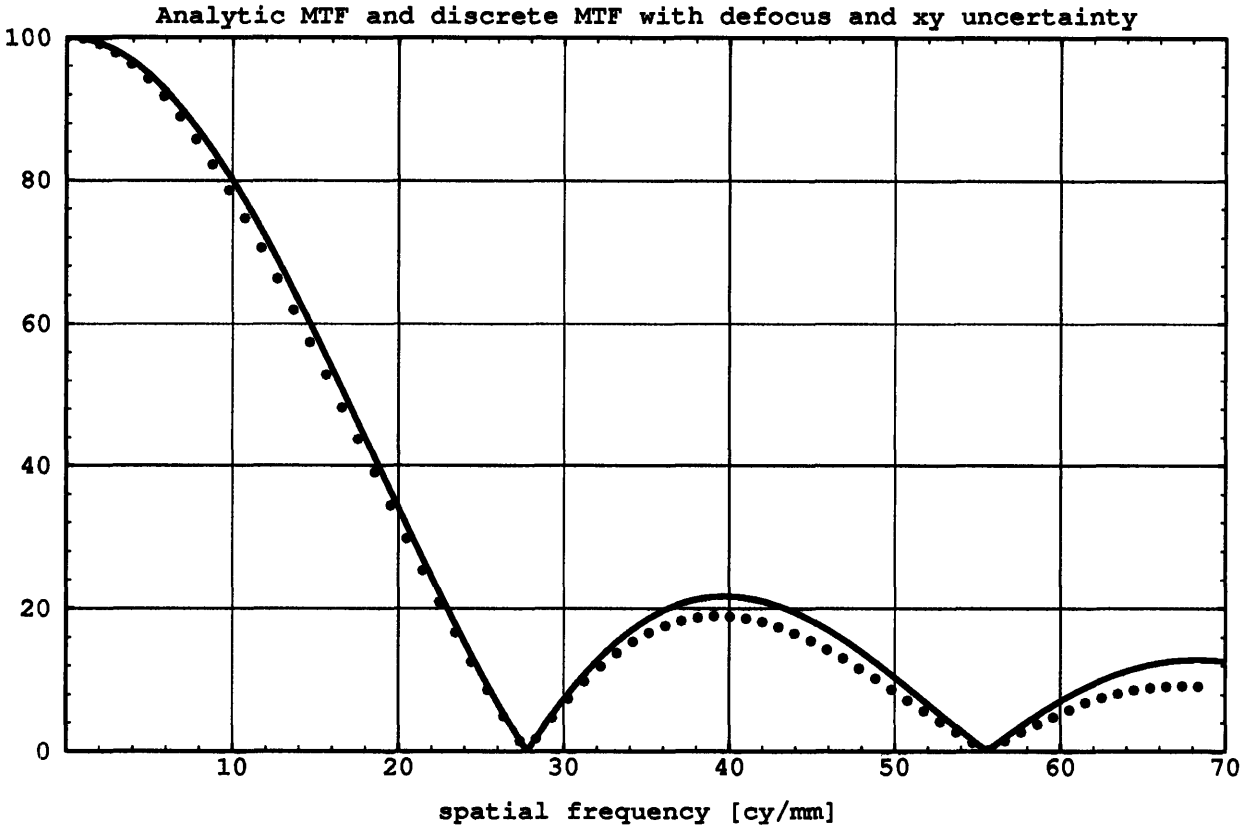

Figure 5-6: Analytic Fourier transform of a 36 μm wide rect function, solid line. Discrete deconvolved transform, dotted line, has been corrupted by defocus, jittter, and aliasing, lowering the MTF. 2 μm steps were used.

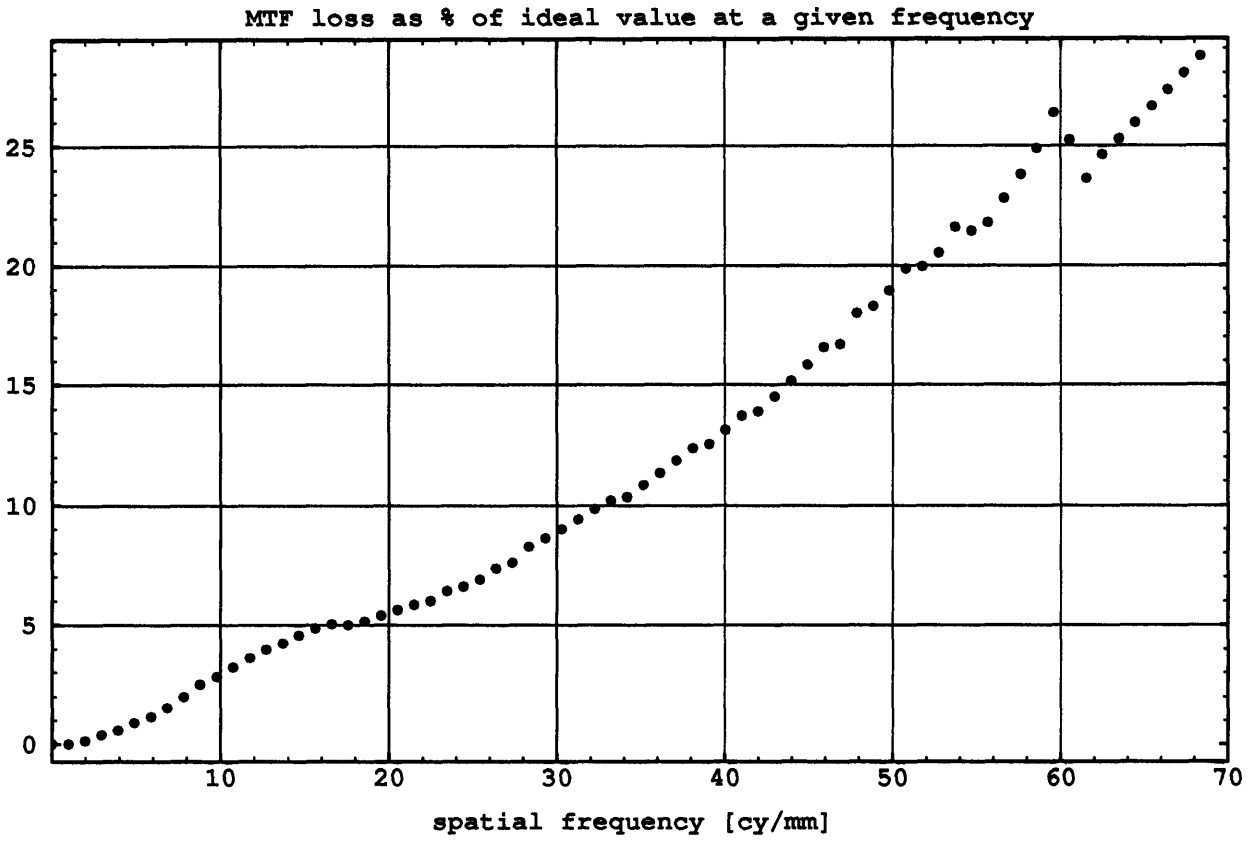

Figure 5-7: Percentage of MTF lost in that point as a function of spatial frequency. This shows by what percentage of its value each point is low.

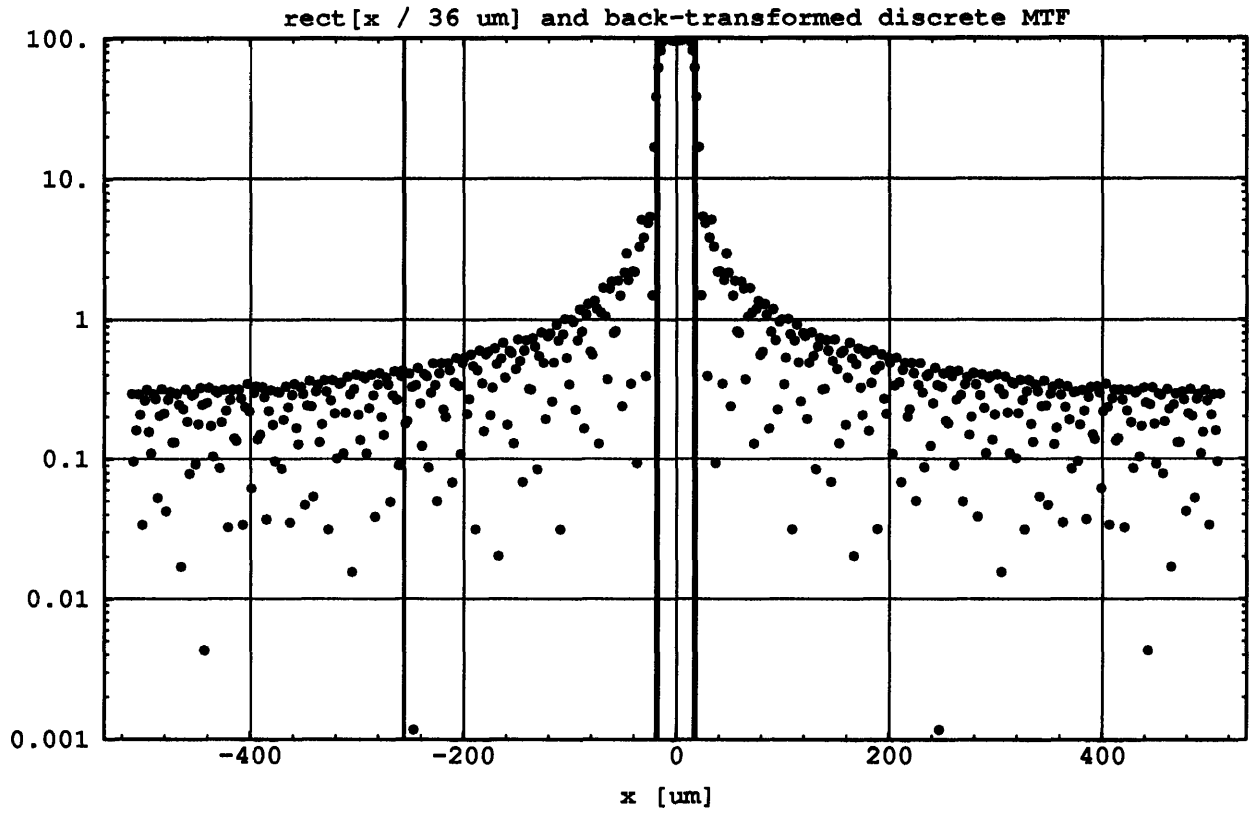

Figure 5-8: Reverse transform of the truncated and corrupted MTF (points), shown with an ideal 36 μm rect function.

5.2.1 Optimizing the optical input

LWIR light was chosen so that defocus would be minimized. This also tests the detectors in their region of spectral operation. Slits of 10 μm and 20 μm reimaged width were both used in order to test if there would be a difference. (The 20 μm slit presents a zero at 50 cycles/mm.) The lateral uncertainty problem should not affect the measurement as strongly as it has been modeled. While this research does not compensate for that problem, encoders are being procured for the station.

Rotational uncertainty is more of a problem. During this testing, the slit alignment approach was this:

1. Screw the slit aperture holder into the bottom of the optical tube, using two adapters with an o–ring and vacuum grease on one of the threads, so that the slit adapter is not easily turned.
2. Rotate dewar until motor translation directions are aligned to the lead–out board tracks and the edge of the CdTe. (A microscope and illuminator allows one to see the part when not scanning with the blackbody.)
3. Slide beamsplitter block over, switching to blackbody illumination.
4. Translate to vicinity of DUT.
5. Center slit as well as possible by translation, focus, and iterate.
6. Access a collinear diode, preferably about 500 or 600 μm away (as defined by photolithography) and put its waveform on the oscilloscope.
7. Translate slit to roughly the center of the two diodes.
8. Simultaneously peak the signal out of both diodes by x and y translation, slit rotation, and focusing.
9. When peaked, translate slit back to the original diode, and center. Slit is now aligned for scans in the direction perpendicular to its length.
10. For a scan in the other direction, do not perturb slit. Using the rotary stage, rotate the dewar 90^o.
11. Translate until the signal is found again. Refocus and recenter.
12. Now scan in the same direction as step 9, remembering that this is now really the perpendicular direction.

While this method works, it is labor–intensive. Since the scanner is now in an open frame station, permanent alignment marks in x and y could be scored on the optical tube. With suitable marks, an alignment of $\pm 1^o$ should be readily attained.

Nonlinearity due to HLI was addressed by procuring a coldshield to reduce the background flux and by filtering the radiation. From a design standpoint, it would be desirable to reduce these flux levels a further order of magnitude. This is not possible with the background radiation, given the present setup. The DUT needs to be within a short distance from the reflecting objective, so that focusing is possible. Therefore, only coldshields of relatively shallow height may be used in

the space between the dewar cap and the clamp which holds the FPA flatpack. The chopped flux level could be reduced by either tighter filtering or by lowering the blackbody temperature, which is possible since the slit signal data have a much higher current level than spot scan data, with no signal–to–noise ratio problems evident. As a check on HLI, the *HET–III* code was run. The *HET–III* code numerically models the full heterojunction diode physics in one–dimension. This was run with parameters to match this scan, and the results indicated that the quantum efficiency losses due to HLI were small even at backgrounds of 10^{19} photons per cm^2 per second, and only became significant at levels of 10^{20} photons per cm^2 per second. If this model is accurate, then these test flux levels, while high, should be tolerable.

5.2.2 Optimizing to reduce random noise

The slit signal is very much stronger than that of a spot. However, the TIA based on bipolar transistors was replaced with a FET based amplifier which should have negligible current noise, and thus overall lower noise. Furthermore, the background flux and background current were reduced. Both of the main random noise sources were thereby mitigated.

5.2.3 Optimizing the discretization

Since the signal is lowpass filtered, either the 4 μm or the 2 μm step size should not be affected by aliasing. Data were taken with both for comparison purposes. Assuming the information is equivalent, 4 μm step/256 point scan is more useful since it is faster.

Chapter 6

Test results and analysis

This chapter presents the results of slit scans on Small Staring Array and Small Scanning test chip Array diodes. Section 6.1 gives the basic results for the symmetric Small Staring Array. Section 6.2 discusses the slit size and step size tradeoffs. The results from the Small Scanning test chip are presented in Section 6.3. Finally, Section 6.4 compares results from both arrays with the numerical results generated in Chapter 3.

6.1 Results of scanning the Small Staring Array

Slit scans were taken on the symmetric Staring Array geometry by the procedure detailed in Chapter 5, and the analysis was performed as outlined in Chapter 4. The basic results for the Small Staring Array are shown in Figures 6-1, 6-2, 6-3, and 6-4. Figure 6-1 shows the raw MTF, called SSR(f_x), the improved, deconvolved MTF, called DSR(f_x), and the ideal sinc function of a 35 μm wide aperture. Figure 6-2 shows the same curves on a spatial frequency scale extending from zero to the array sampling frequency (simply the reciprocal of the pitch). While the DSR(f_x) is well below that of an aperture function, its improvement over the raw data shows the necessity of deconvolving the input form. Figure 6-3 shows the direct space data as well as the deconvolved dsr(x) on a logarithmic scale and Figure 6-4 displays it on a linear scale. On the linear scale graph, it is evident that the scan origin was not at the detector center. This is probably due to the stepper motor skipping steps during its initial large shift. While the deconvolved data is narrower than the raw ssr(x), as expected, the many ripples are unphysical. The analysis process may use an incorrect optical form. The real optics waveform has electromagnetic content which is defined by both the filter and the detector spectral response. It was hoped that a polychromatic MTF, composed of seven linearly weighted monochromatic MTFs, could suitably approximate the continuous diffraction MTF. Two problems are then the discontinuous weighting of the polychromatic MTF and the choice of inexact endpoints.

Upon closer examination of the deconvolved waveform, the frequency of the unwanted oscillations is roughly 40 cycles/mm, where the deconvolved MTF has considerable content. One approach which would not overrepresent the spatial definition of the detectors would be to use a suitable function to lowpass filter the data. This would attenuate the ripples at the cost of lowering the the deconvolved MTF. Another issue is the angle of the slit with respect to the scan direction. If the slit is not perpendicular to the scan direction, a wider measured width will result. This will degrade the raw and deconvolved MTFs.

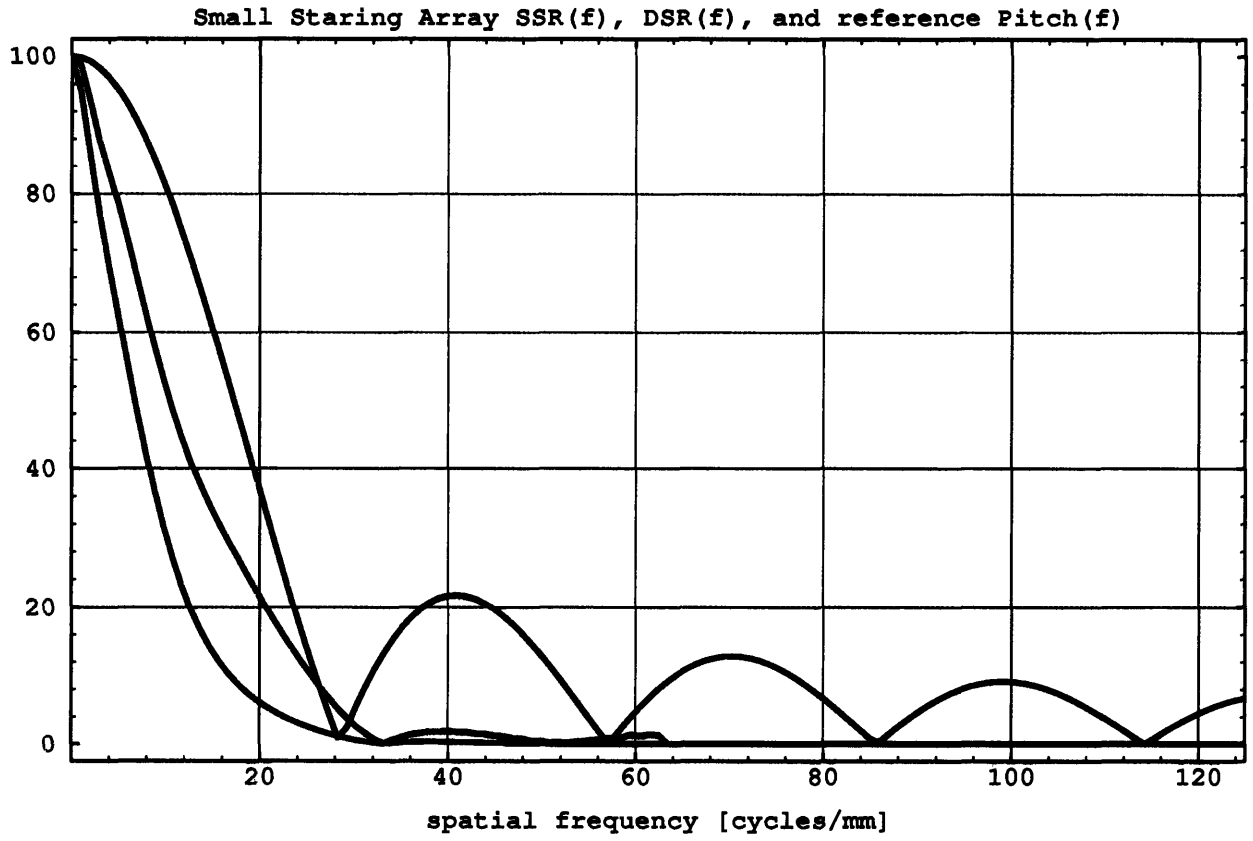

Figure 6-1: Transform of raw Small Scanning Array slit scan response, lowest curve, transform of deconvolved data, middle curve, and transform of 35 μm aperture, highest curve. The removal of the spot increases the MTF over the transform of the raw data. An aperture function continues to have content at high spatial frequency, since diffusion is not considered.

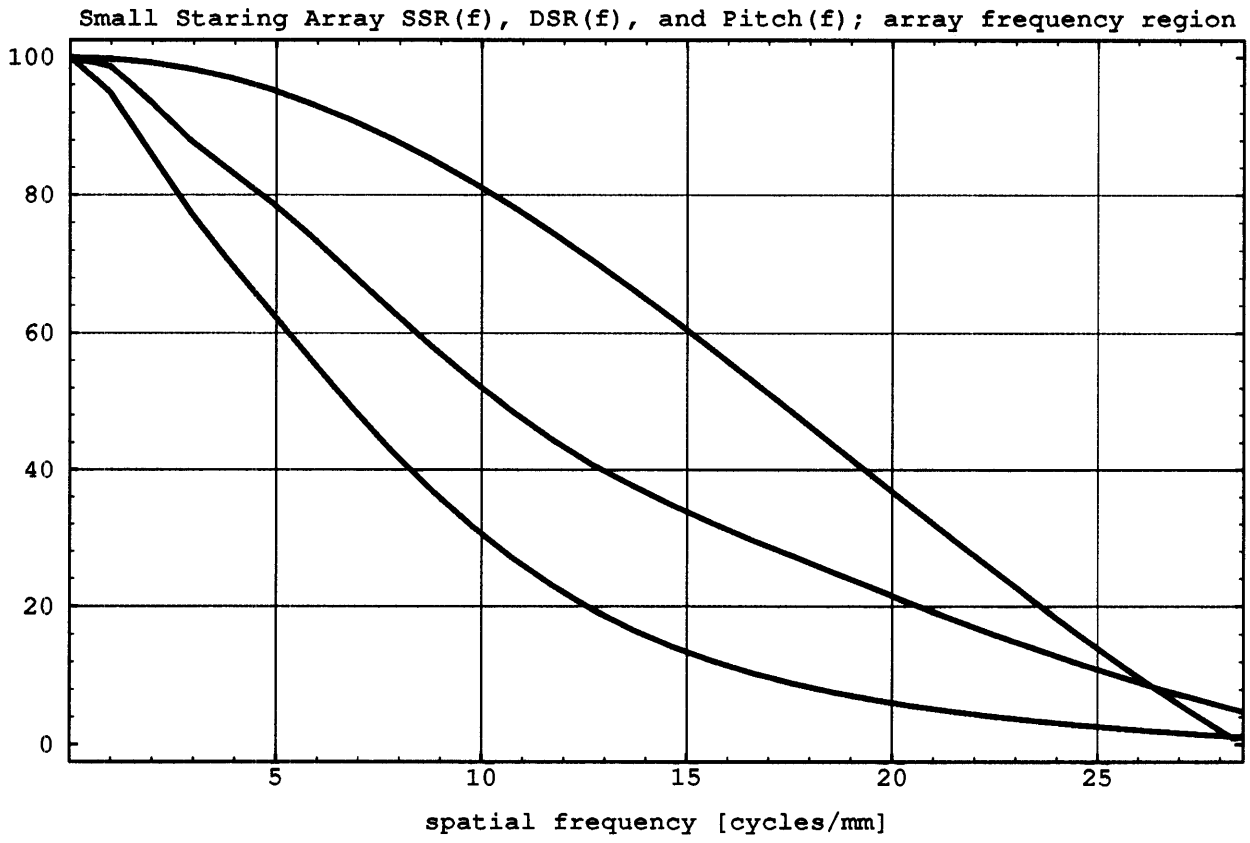

Figure 6-2: Transform of raw data, lowest curve, transform of deconvolved data, middle curve, and transform of 35 μm aperture, highest curve. This is the result of Figure 6-1, plotted out to the array sampling frequency.

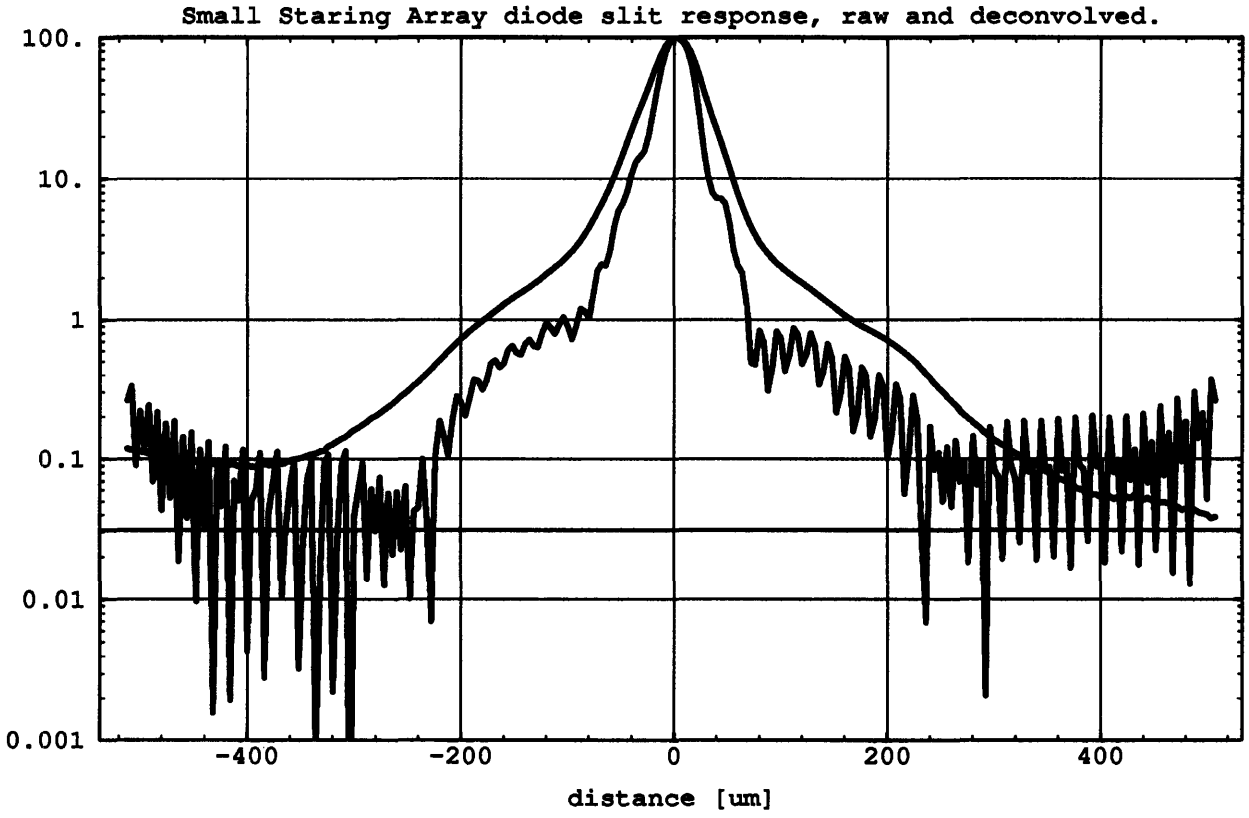

Figure 6-3: Raw slit scan data, upper curve; deconvolved data, lower curve. While the central lobe is made considerably more narrow, many ripples are introduced which are particularly visible on a logarithmic scale.

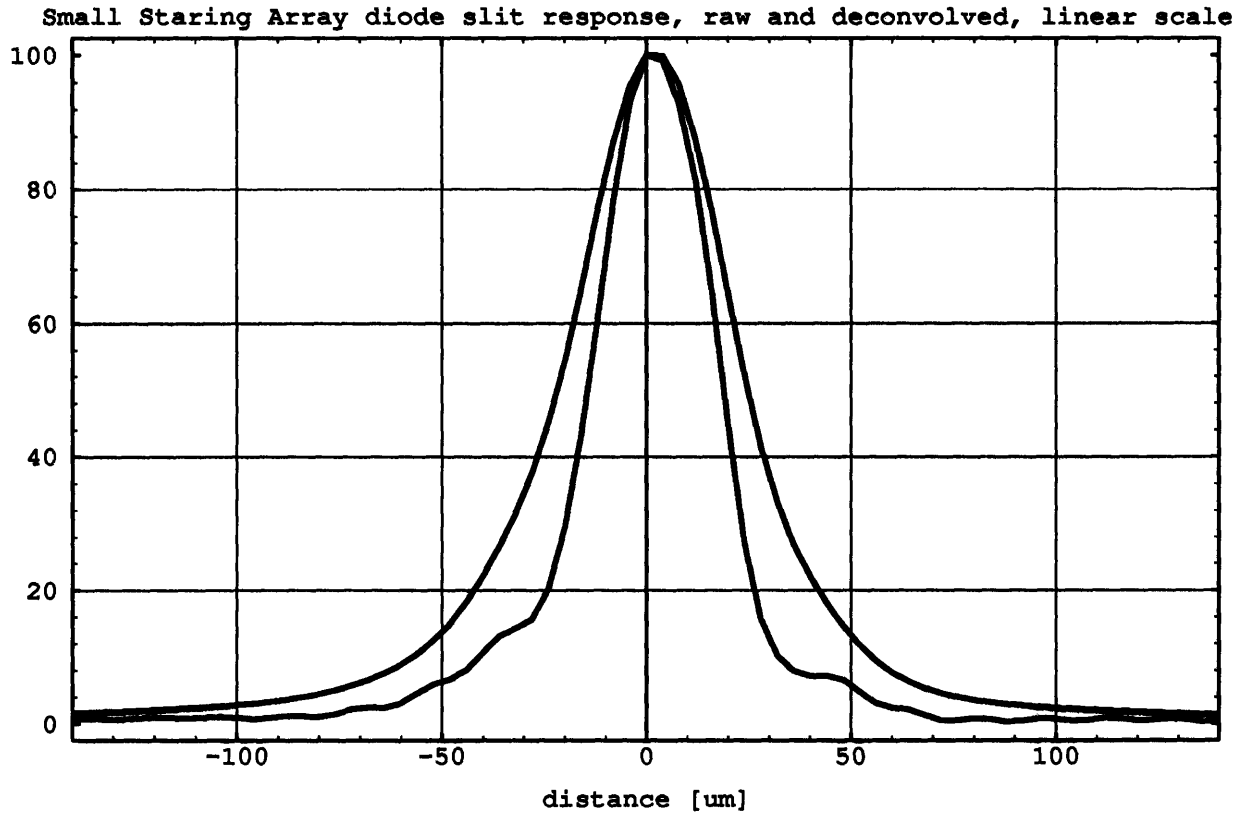

Figure 6-4: Raw data, upper curve; deconvolved data, lower curve. This is the data of Figure 6-3 on a linear scale, so the ripples are less visible.

6.2 Comparison of results with slit and step size trades

6.2.1 Step size

Figures 6-5 and 6-6 show the deconvolved MTF yielded from 2 μm and 4 μm steps. Apart from the slight peak in the 2 μm step waveform, around 62 cycles/mm, which is unphysical, the difference between MTFs is not appreciable.

Figures 6-7 and 6-8 show the deconvolved slit responses for the two cases. From Figure 6-8, the linear scale graph, it may be seen that the 2 μm scan was not initially well centered and appears to have more ripple. However, on the logarithmic scale, the 2 μm step size curve has a lower average value than the 4 μm curve on the extreme wings of the response.

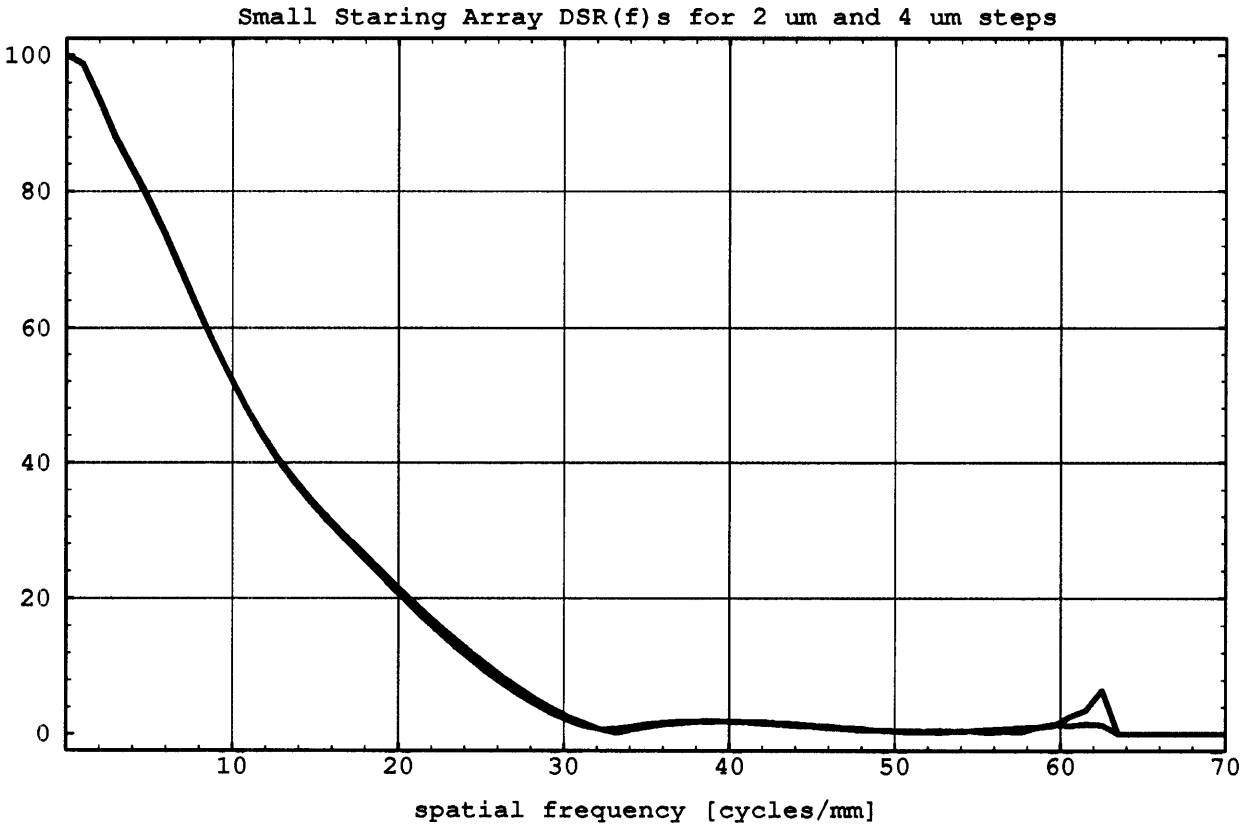

Figure 6-5: Deconvolved MTF for the 2 μm and 4 μm step size. 2 μm step size peaks slightly around 62 cycles/mm. Either step size should prove acceptable.

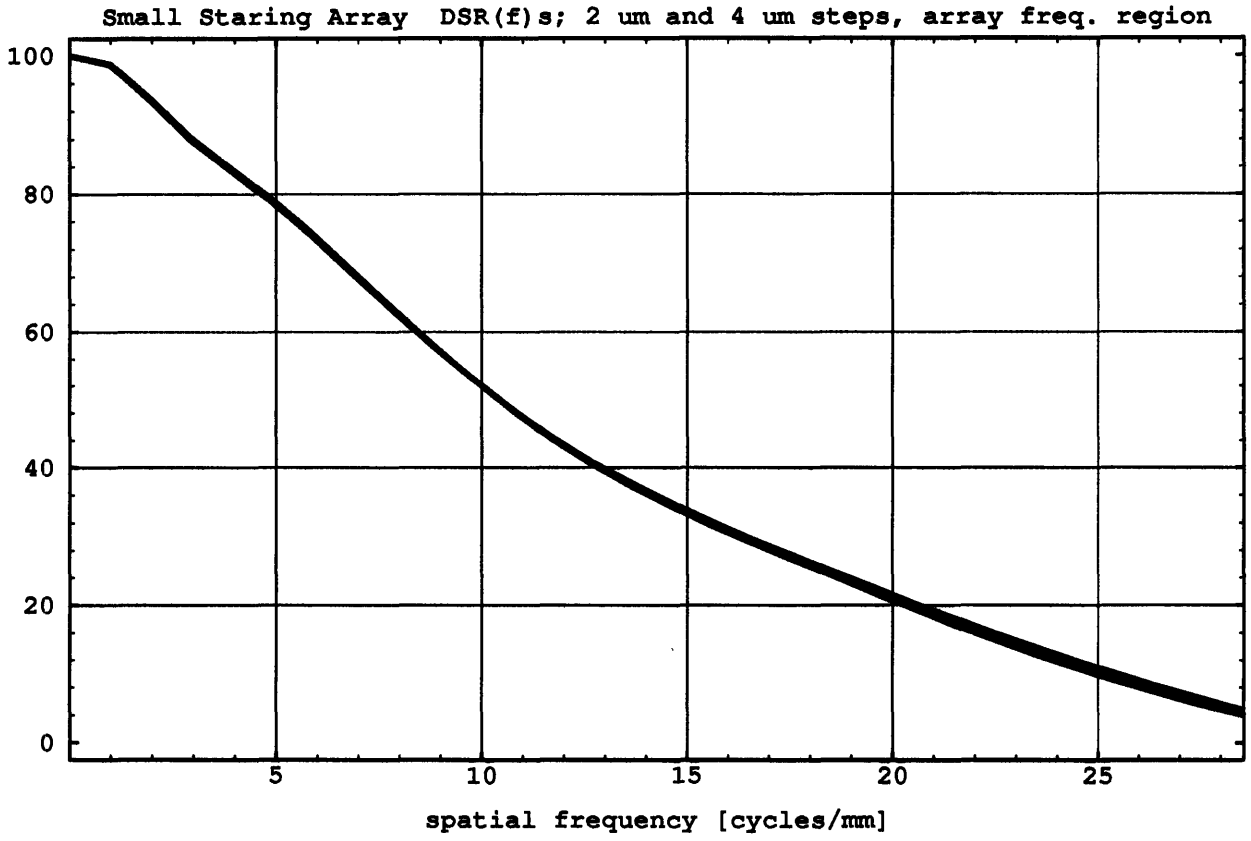

Figure 6-6: Deconvolved MTF for the 2 μm and 4 μm step size, showing negligible difference in the region extending to the array sampling frequency.

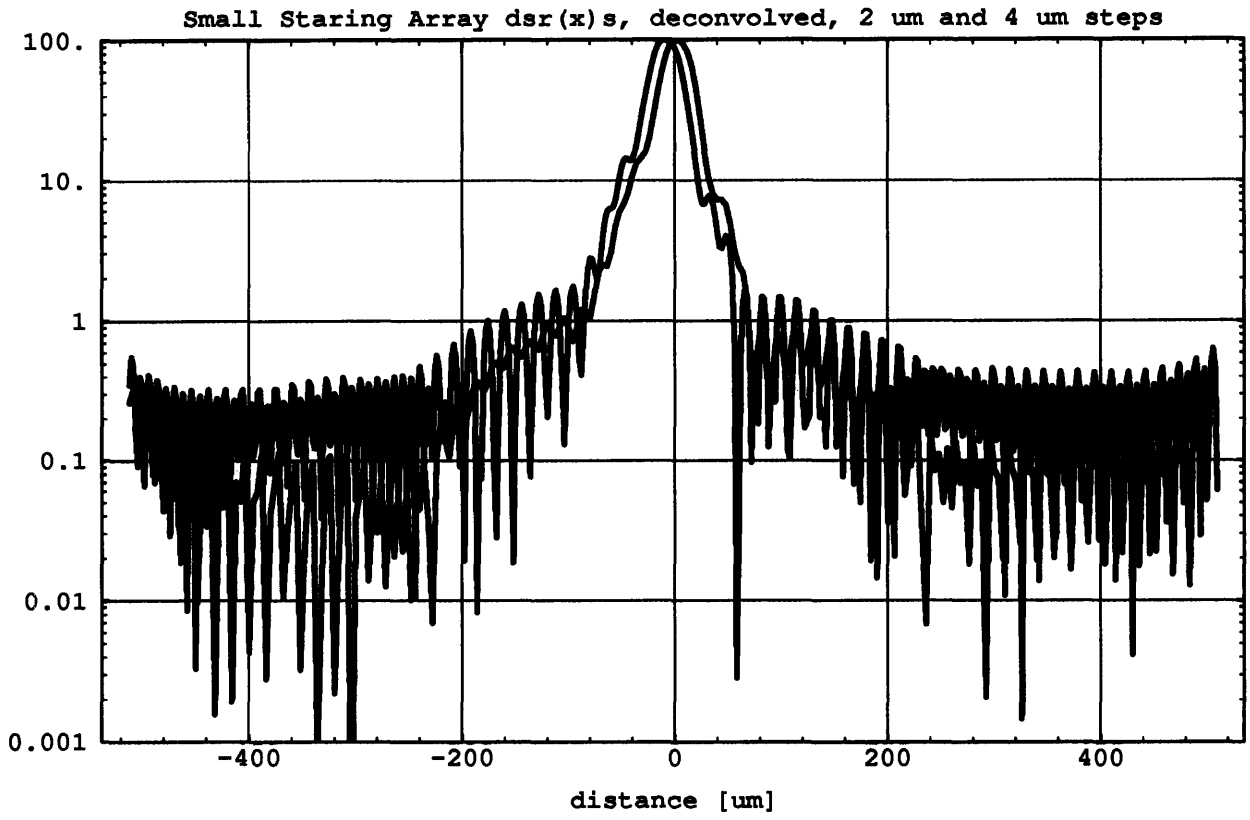

Figure 6-7: Deconvolved diode slit responses for 2 and 4 μm step sizes. Both are aggravated by ripples but the 2 μm scan has a lower average value at large distances from the origin.

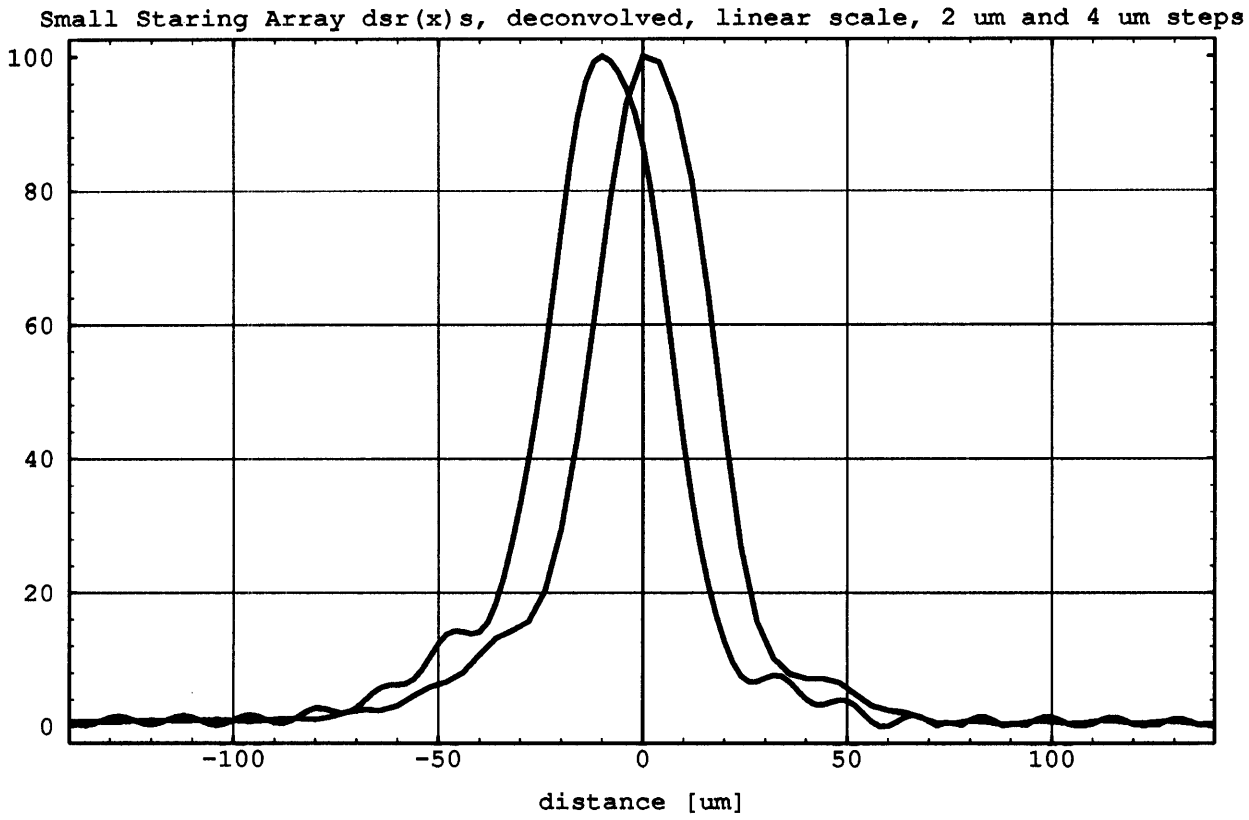

Figure 6-8: Deconvolved diode slit responses for 2 and 4 μm step sizes. The 2 μm scan is off center.

6.2.2 Slit size

Figures 6-9 and 6-10 show the result of varying the slit width on deconvolved detector MTF. 2 μm steps were used. Again, the results are not appreciably different. The logarithmic scale graph does not show an appreciable difference between the two, and the ripples persist. The linear scale graph shows that, while the 20 μm slit scan was not well centered, the central lobe shapes match very well.

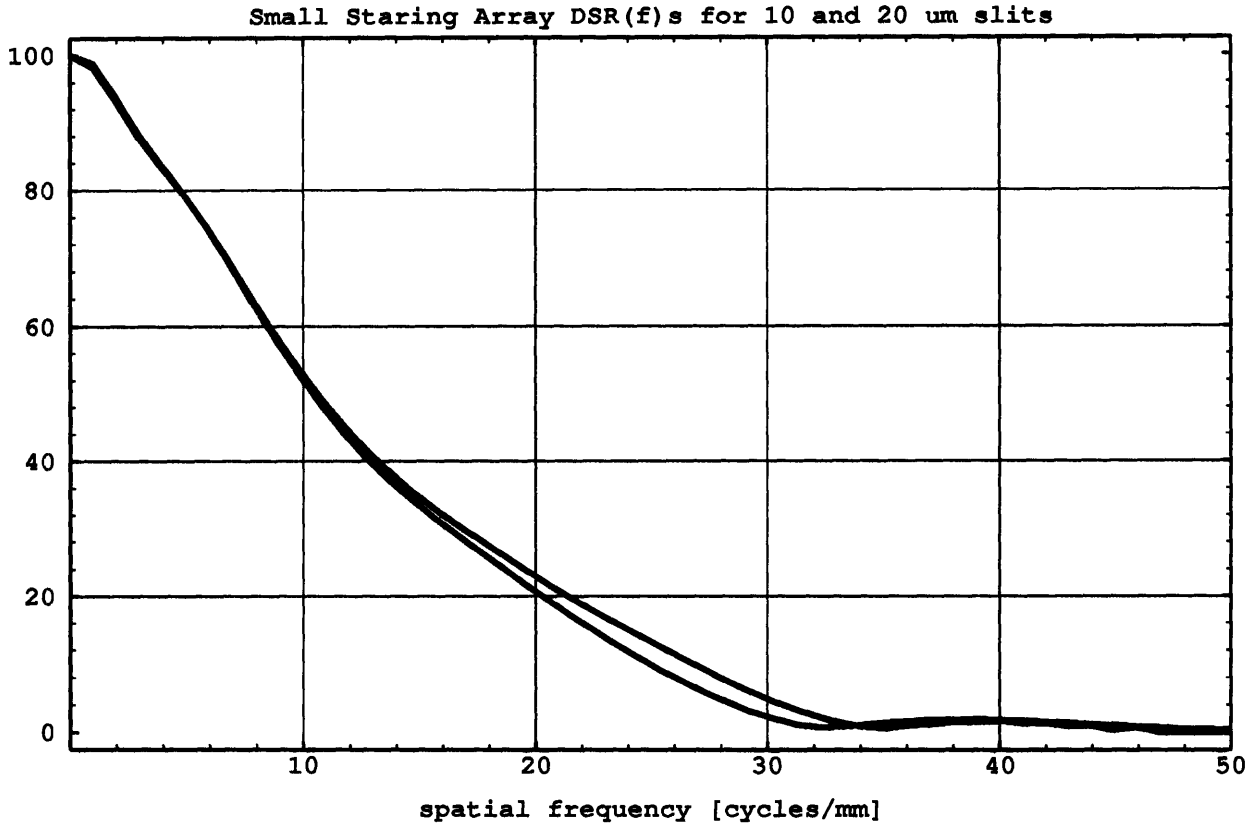

Figure 6-9: Deconvolved MTF curves for the 10 μm and 20 μm slit size, showing negligible difference.

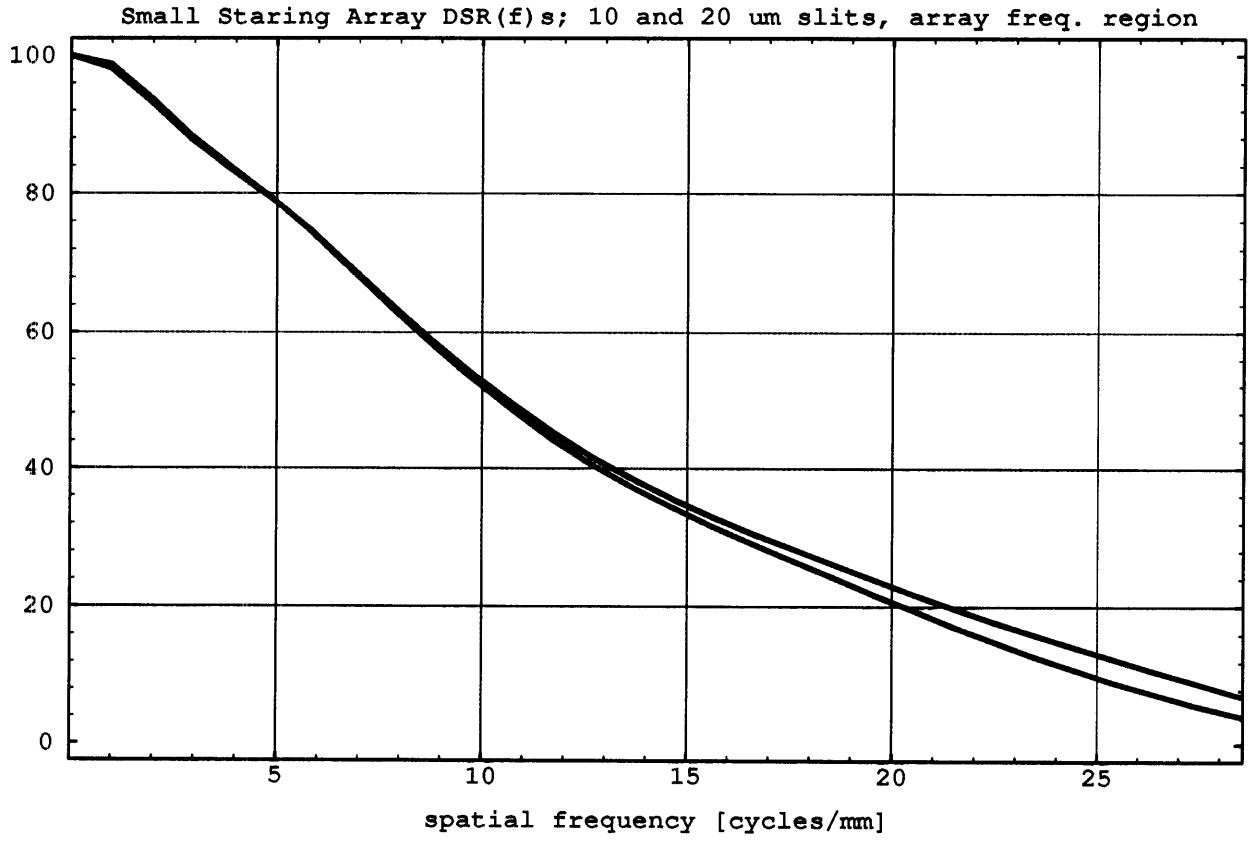

Figure 6-10: Deconvolved MTF curves for the 10 μm and 20 μm slit size, showing negligible difference out to the array sampling frequency.

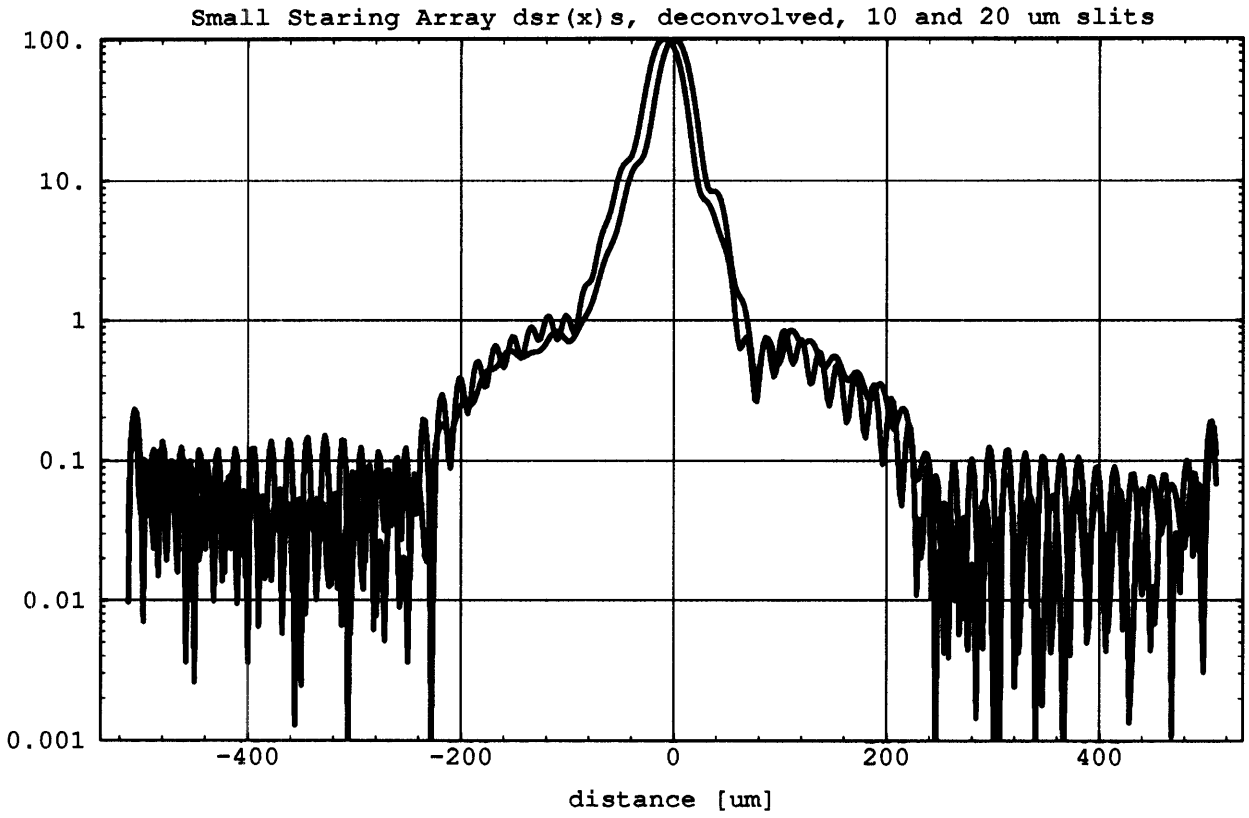

Figure 6-11: Deconvolved diode slit responses for 10 and 20 μm slit sizes. The ripple problem appears to be of equal magnitude for both.

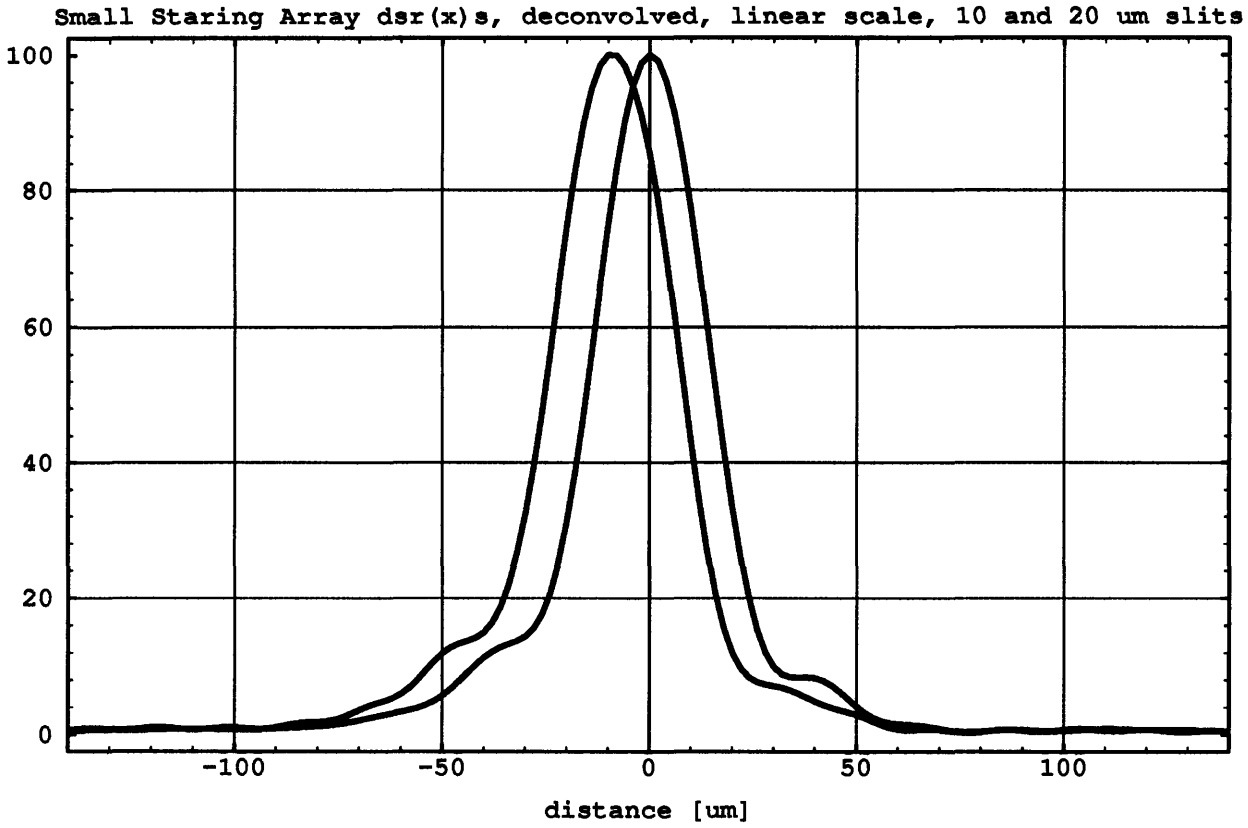

Figure 6-12: Deconvolved diode slit responses for 10 and 20 μm slit sizes. The 20 μm slit scan is off center, but the shape of the central lobe appears to match well.

6.3 Results of scanning the Small Scanning Array

The next group of figures shows the result of slit scans taken on the scanning array geometry. Figures 6-13 through 6-16 show the results of a scan taken in the x, or narrow direction with a 2 μm step size and a 10 μm wide slit. Figure 6-13 shows the MTF of the raw data, SSR(f_x), the deconvolved DSR(f_x), and the reference pitch sinc function for the width of 50.8 μm. Recall that the geometry is guarded, so the nearest pixel neighbor is not the nearest physical neighbor. Figure 6-14 shows the same curves in the region below the array sampling frequency. Figure 6-15 shows the original and deconvolved response in the x–direction. Again, unphysical ripples are an issue, but the deconvolved response is everywhere below the original data. Figure 6-16 shows the same data on a linear scale.

Figures 6-17 through 6-20 show the slit scan results for the same detector across the y, or wide direction. Figures 6-17 and 6-18 show the raw MTF, the deconvolved MTF and the MTF of an ideal sinc function, first out to the optical cutoff frequency and then out to the array sampling frequency. Figures 6-19 and 6-20 show the raw and deconvolved slit responses. Considerable asymmetry appears in both of these figures. This may be due either to some problem in grounding the neighboring diodes, secondary reflections occurring off some feature, or slit rotational error. The ripples persist as well.

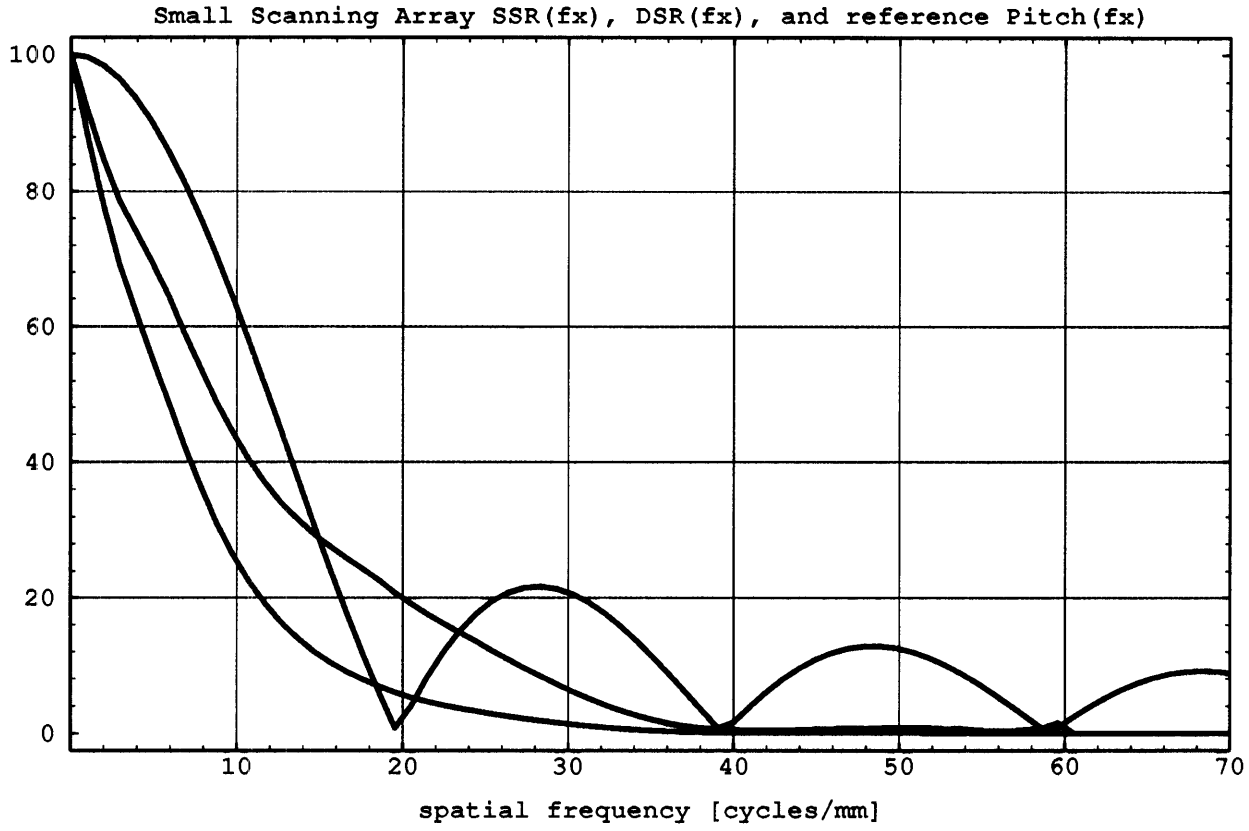

Figure 6-13: Transform of raw slit scan response for the narrow direction of the Small Scanning Array, lowest curve, transform of deconvolved slit response, middle curve, and transform of 50.8 μm aperture, highest curve.

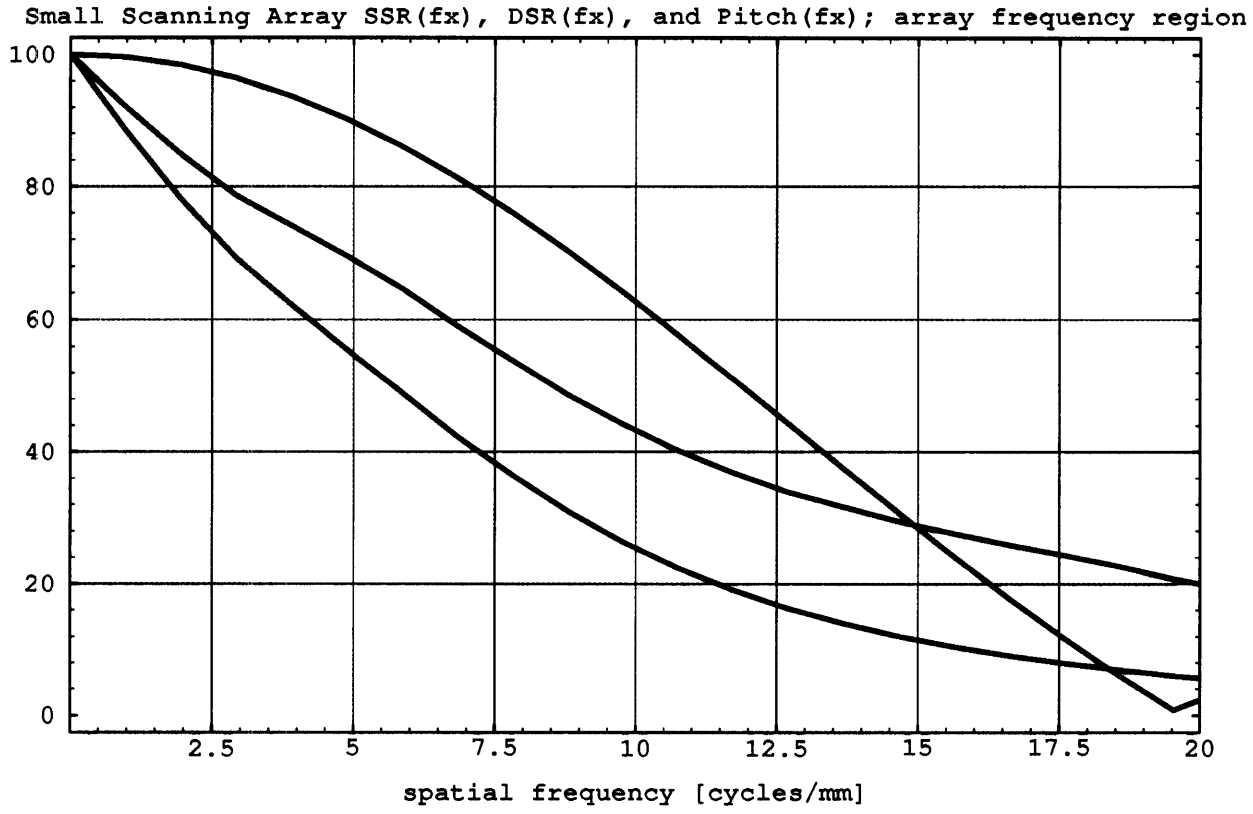

Figure 6-14: Transform of raw slit scan response, lowest curve, transform of deconvolved slit response, middle curve, and transform of 50.8 μm aperture, highest curve. This is just the data of Figure 6-13 plotted out to the array sampling frequency.

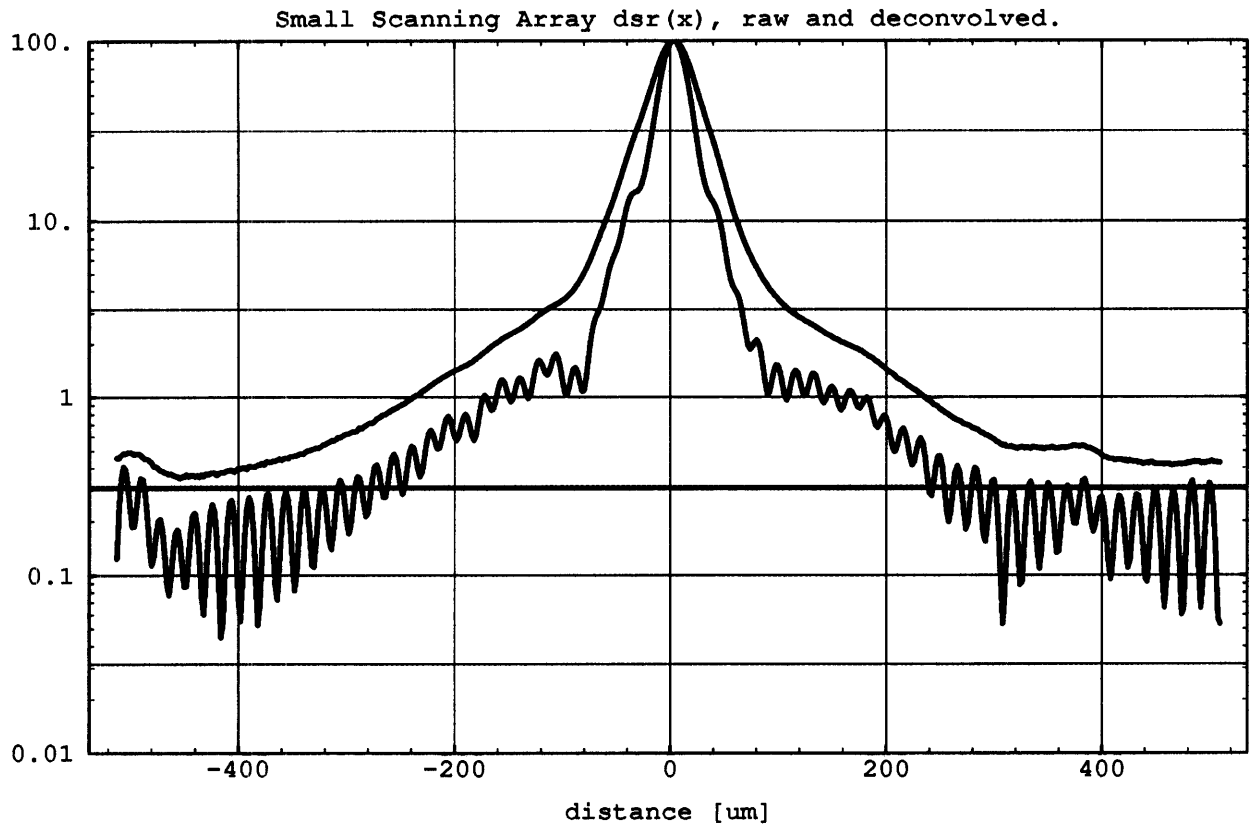

Figure 6-15: Raw slit scan response, upper curve; deconvolved slit response, lower curve. While ripples are evident, the deconvolved response is everywhere lower than the raw data.

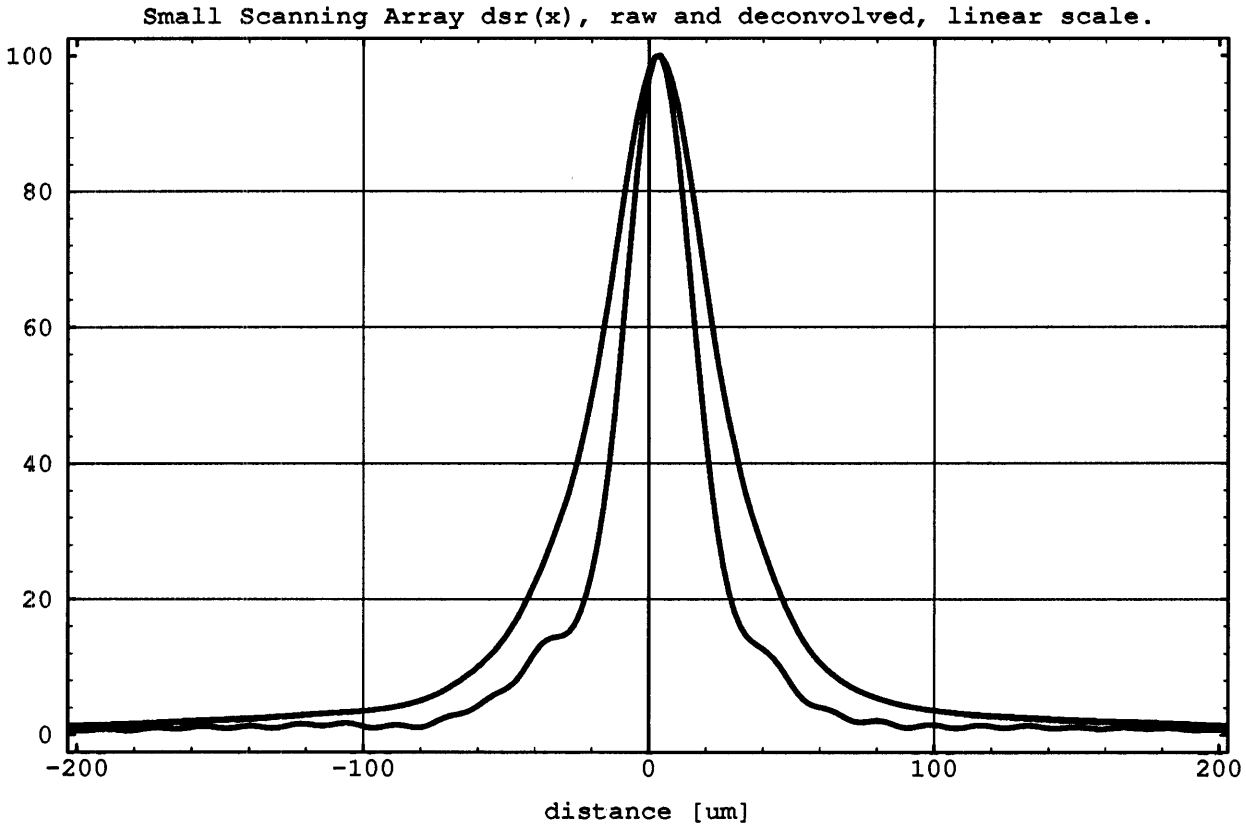

Figure 6-16: The data of Figure 6-15 on a linear scale. Raw data, upper curve; deconvolved data, lower curve. Deconvolution removes the width of the spot.

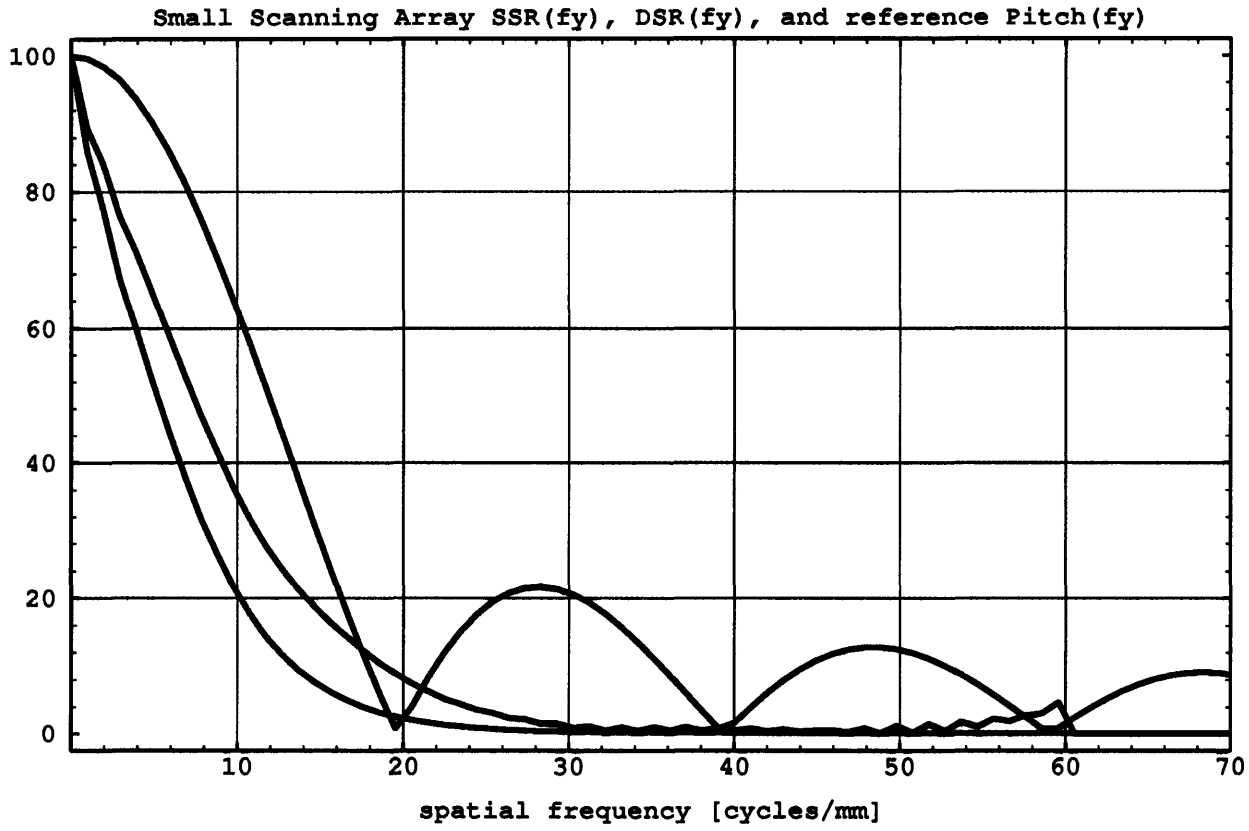

Figure 6-17: Transform of raw slit scan response for the wide direction of the Small Scanning Array, lowest curve, transform of deconvolved slit response, middle curve, and transform of 50.8 μm aperture, highest curve.

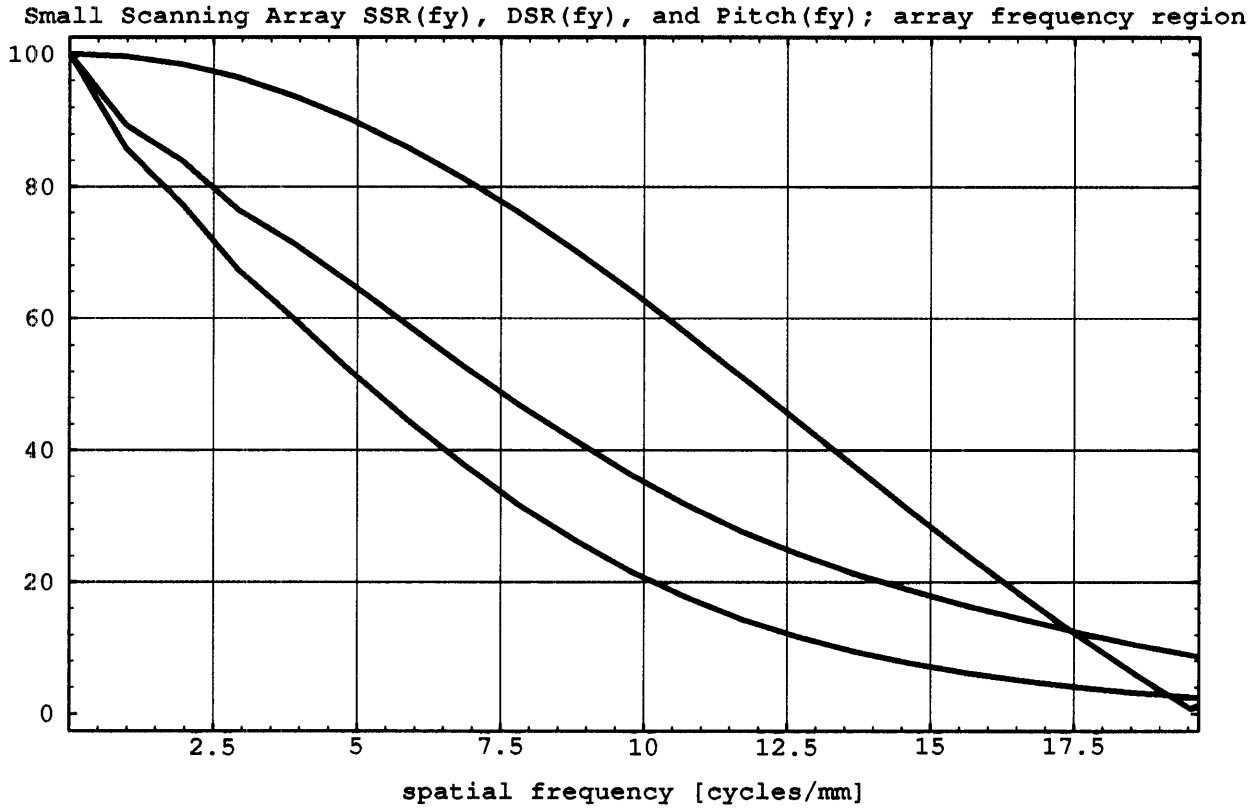

Figure 6-18: Transform of raw slit scan response, lowest curve, transform of deconvolved slit response, middle curve, and transform of 50.8 μm aperture, highest curve. This is just the data of Figure 6-17 plotted out to the array sampling frequency.

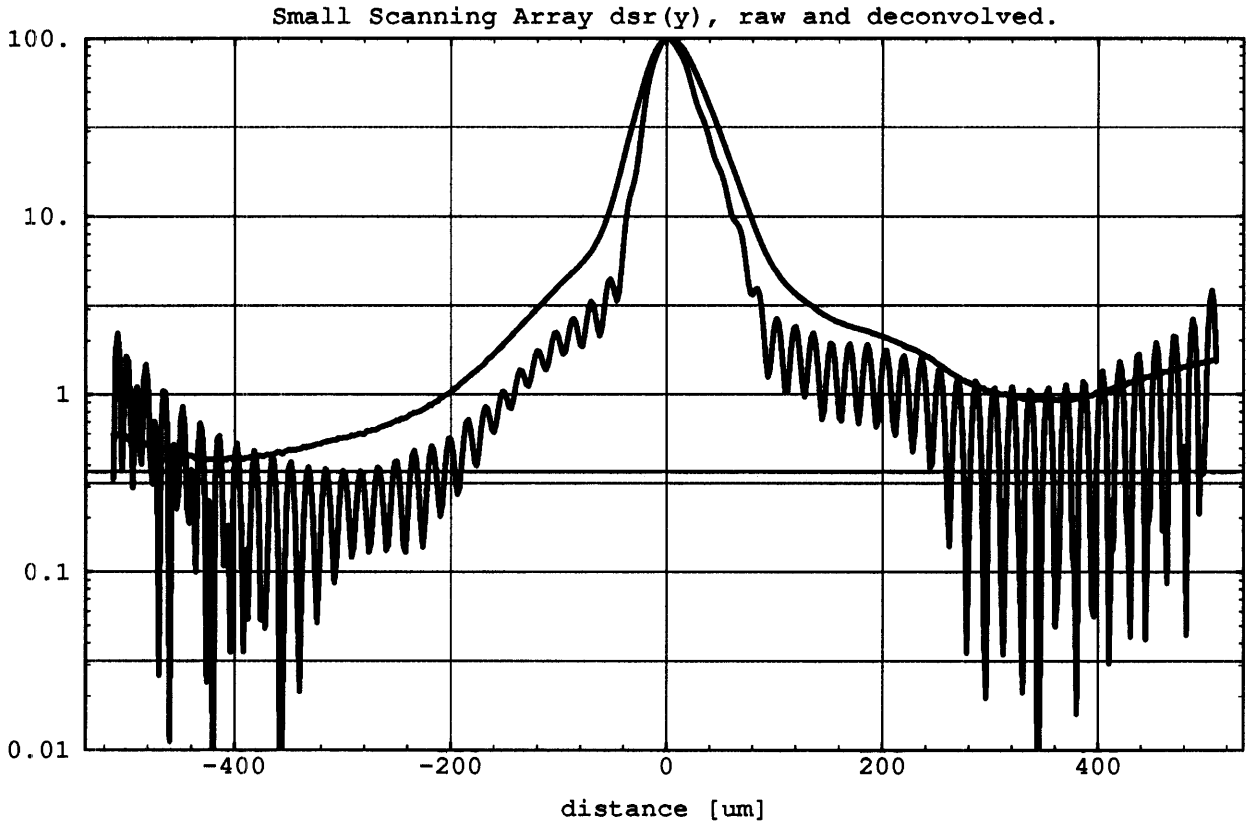

Figure 6-19: Raw slit scan response, upper curve; deconvolved slit response, lower curve. Ripples are evident, and the deconvolved response is not everywhere lower than the raw data.

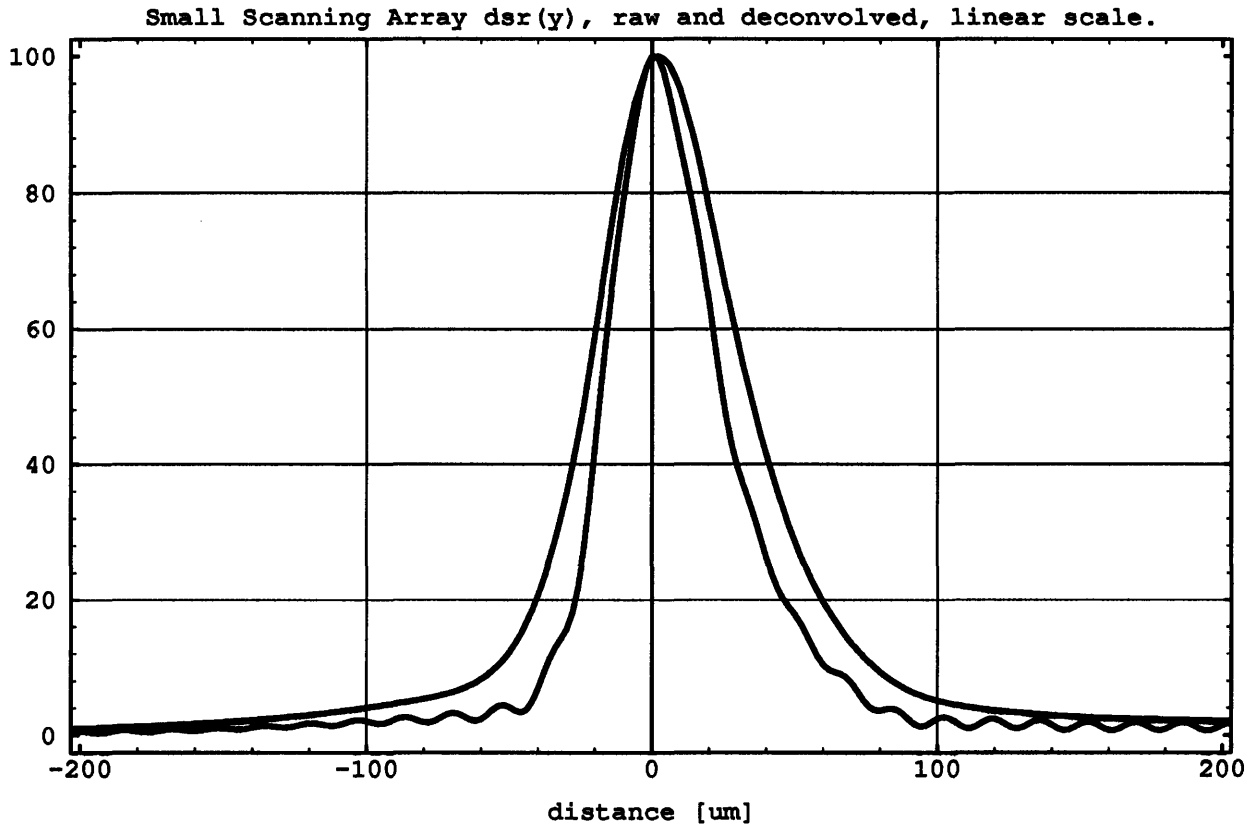

Figure 6-20: The data of Figure 6-19 on a linear scale. Raw data, upper curve; deconvolved data, lower curve. Deconvolution removes the width of the spot. The response is seen to be asymmetric.

6.4 Comparison of results with the numerical model

Figures 6-21, 6-22, and 6-23 compare the deconvolved results of the slit scans with the diode slit responses generated by the numerical model in Chapter 3. No effort was made to specifically match the data by varying model parameters. Figure 6-21 shows the Small Staring Array model MTF and the MTF obtained by slit scan. Figures 6-22 and 6-23 apply to the Small Scanning Array in the x and y directions respectively. These also show that the real data has a poorer MTF than the Chapter 3 numerical model MTFs. While the parameters were not varied here in order to match the data, they might be changed in order to do so, particularly diffusion length, which is the most uncertain parameter. The smoothly varying mesa cuts in real arrays also should lead to a lower MTF than that given by the model, which has abrupt right angled mesa cuts. Additionally, any rotational error in the slit scans would yield a physically wider measured detector response. The sinc function of the slit width would not compensate for this, and the reported deconvolved MTF would be too low.

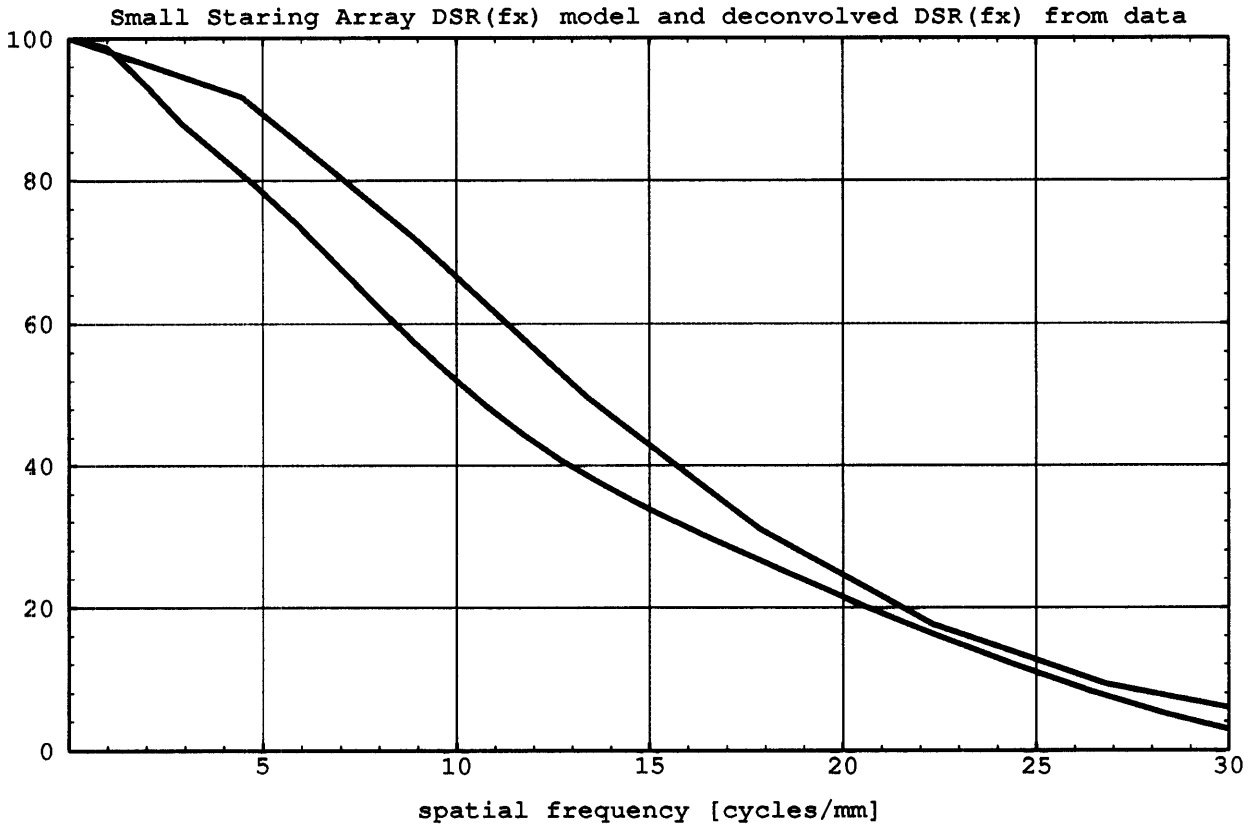

Figure 6-21: Deconvolved DSR of data for the Small Staring Array, lower curve. DSR yielded from numerical model, upper curve.

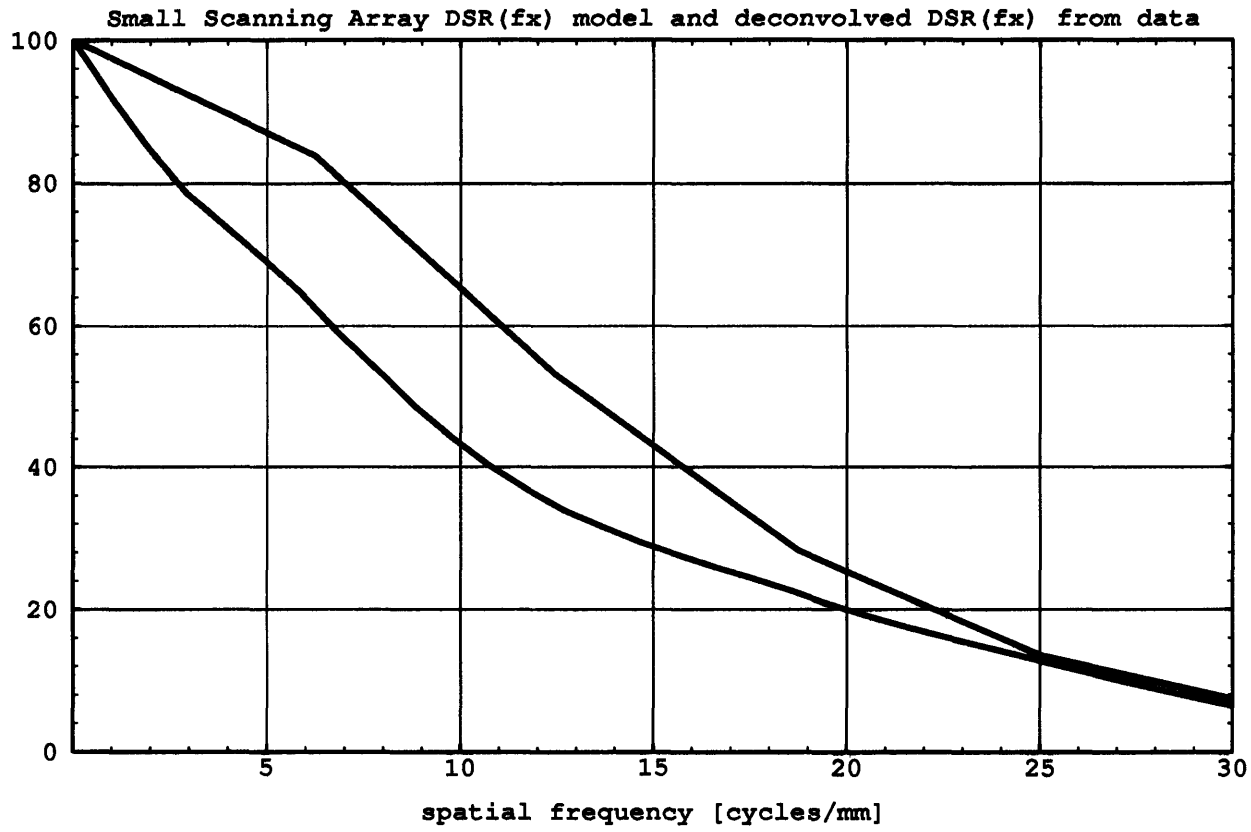

Figure 6-22: Deconvolved DSR(f_x) of data from the Small Scanning Array, lower curve. DSR yielded from numerical model, upper curve.

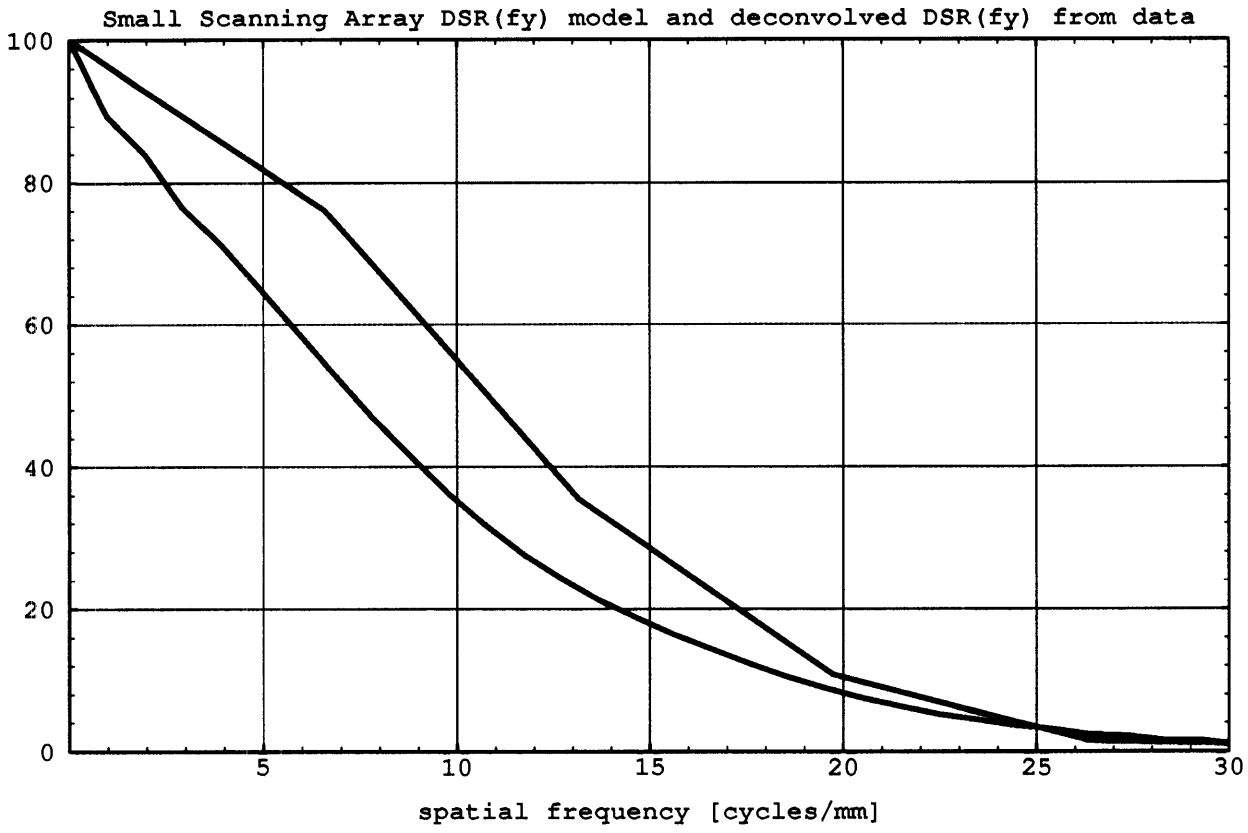

Figure 6-23: Deconvolved DSR(f_y) of data from the Small Scanning Array, lower curve. DSR yielded from numerical model, upper curve.

Chapter 7

Conclusions

A summary and assessment is given for this research about the modeling and testing of photodiode spatial response. Possible extensions of this work are noted.

7.1 Summary and Evaluation

7.1.1 Modeling

In this thesis, a model was proposed for the MTF of the focal plane array. While a consensus on the MTF of shift variant systems is not evident in the literature, the key issues for FPA MTF were identified here. A three–dimensional numerical model of minority carrier drift and diffusion successfully implements the single pixel portion of that FPA MTF model.

The derivation of the numerical model has been shown and the basic assumptions were presented. The Taylor series expansion error terms which describe the dependence of error on grid spacing were also included. The user changeable parameters of the program were described.

The self–consistency of the model was also verified. The model converges to the usual infinite area solution for quantum efficiency when a large diode is simulated. The integrals of the impulse and slit responses both match the flood illumination quantum efficiency. The responses are symmetric in x and y for square array geometries. Furthermore, the profile MTFs were compared with the MTFs generated by an analytical model. It is believed that if the same electric field were used, both solutions would agree exactly.

Finally, results were obtained by using the model. Changes in parameters which improve MTF were found. The MTF was unexpectedly found to be relatively independent of pitch to junction size ratio. Very significant MTF and crosstalk improvements were demonstrated using a multiparameter approach.

The principal defect of the model is the time required for its use. Since profile MTF is of the most

interest, however, most modeling runs are likely to be slit scan simulations. However, the model cannot generate a full matrix of parameter changes and their corresponding MTFs very quickly. Other defects of the model include the sharp mesa cuts and the uncertainty associated with using a low density of grid points. Improvements are discussed in Section 7.2.

7.1.2 Testing

Progress was also made in the area of characterizing physical diode response. A formal analysis methodology was outlined, and a companion test procedure was developed. Sources of error were analyzed in order to identify the magnitude of possible uncertainty in the measurement. The procedure was optimized in light of these concerns. Slit scans were taken and analyzed for both square and rectangular array geometries. The necessity of deconvolution was shown for LWIR slit illumination, as may be seen from the diode slit response curves in either the direct or frequency space domain. Still at issue are the unphysical ripples caused by the deconvolution. This limits the usefulness of the analysis, rendering deconvolved crosstalk quantities suspect. Finally, these test results were compared with initial numerical model results, although the model parameters were not yet changed in order to fit the data.

7.2 Suggestions

Full implementation of a shift variant FPA MTF model is possible using these single pixel results. While such a model might not ultimately be the most useful way to characterize FPA spatial response, it is a starting point. In terms of verifying the model, Cheung's MTF model could be derived with a forcing field and the results could be compared to the numerical results here. Specific desirable changes to the model include:

- Implementation of an adaptive grid to reduce the number of grid points and cut simulation time.
- Creation of a field model based on real x-value gradient data.
- Allowing for a floating potential at neighboring junctions (no current flow case).
- Provision for curved mesa walls.
- Using linear superposition to construct a polychromatic detector MTF. This means generating the MTF for an adequate number of choices of the absorption coefficient, and properly summing the weighted monochromatic MTFs.

Additionally, the product of the profile MTFs might be compared with the full two–dimensional MTF. This product may be found to adequately approximate the full MTF, and thus obviate the need for additional simulation time.

Future work on testing would include mitigating the ripple problem, possibly by using more accurate forms of the polychromatic diffraction MTF. The optical MTF might have to be generated for many different detector cutoff wavelengths. The uncertainties associated with slit rotation and translation also need to be mitigated.

Physical results and modeling results need to be compared and reconciled, so the model may be confirmed as an accurate design tool. As a beginning, the model could be run to generate better matches to the data presented in Chapter 6. Finally, the "matching" parameter values need to be compared with other detector data so that all the information available on that detector is self–consistent.

Bibliography

[1] R.J. Briggs. Three dimensional numerical analysis of diffusion current and quantum efficiency of small area $Hg_{1-x}Cd_xTe$ photodiodes. In *International Electron Devices Meeting*, 1981.

[2] R.J. Briggs. Response efficiency and point spread function for 1 mil size p–on–n HgCdTe photodiodes. In *IRIS Detector Specialty Group Meeting*, August 1991.

[3] D. T. Cheung. MTF modelling of backside–illuminated pv detector arrays. *Infrared Physics*, 21:301–310, 1981.

[4] Luigi de Luca and Gennaro Cardone. Modulation transfer function cascade model for a sampled imaging system. *Applied Optics*, 30(13):1659–1664, 1991.

[5] C. H. Edwards and David E. Penney. *Elementary Differential Equations with Boundary Value Problems.* Prentice–Hall, Englewood Cliffs, NJ, 1989.

[6] Richard LeBlanc and Casey Contini. Infrared focal plane array modeling. *Proceedings of the SPIE: Infrared Imaging Systems: Design, Analysis, Modeling, and Testing*, 1309:27–39, 1990.

[7] S. Park, R. Schowengerdt, and M. Kaczynski. Modulation–transfer–function analysis for sampled image systems. *Applied Optics*, 23:2572–2582, 1984.

[8] M.B. Reine, A.K.Sood, and T.J.Tredwell. *Semiconductors and Semimetals*, volume 18, chapter 6. Photovoltaic Infrared Detectors. Academic Press, New York, 1981.

[9] M.H. Weiler, P.N. Norton, L.L.Carson, and J.J.Schirripa. Hardness improvement program final technical report: Volume 1. Technical report, USASDC Contract DASG60–87–C–0038, October 1989.

[10] Charles S. Williams and Orville A. Becklund. *Introduction to the Optical Transfer Function.* John Wiley and Sons, Inc., New York, 1989.

[11] W. Wittenstein, J.C. Fontanella, A.R. Newbery, and J. Baars. The definition of the OTF and the measurement of aliasing for sampled–imaging systems. *Optica Acta*, 29(1):41–50, 1982.